

LPI Summer Intern Program in Planetary Science

PAPERS PRESENTED AT THE

**37TH SUMMER INTERN
CONFERENCE**

**AUGUST 10, 2022
HOUSTON, TX**



Papers Presented at the

Thirty-Seventh Annual Summer Intern Conference

August 10, 2022

2022 Summer Intern Program for Undergraduates
Lunar and Planetary Institute

Sponsored by
Lunar and Planetary Institute
NASA Johnson Space Center



Compiled in 2022 by

Meeting and Publication Services
Lunar and Planetary Institute
USRA Houston
3600 Bay Area Boulevard, Houston TX 77058-1113

The Lunar and Planetary Institute is operated by the Universities Space Research Association under a cooperative agreement with the Science Mission Directorate of the National Aeronautics and Space Administration.

Any opinions, findings, and conclusions or recommendations expressed in this volume are those of the author(s) and do not necessarily reflect the views of the National Aeronautics and Space Administration.

Material in this volume may be copied without restraint for library, abstract service, education, or personal research purposes; however, republication of any paper or portion thereof requires the written permission of the authors as well as the appropriate acknowledgment of this publication.

HIGHLIGHTS

LPI Summer Intern Program 2022 — Planetary Science Seminars

Facilitated by Julie Stopar, Claudia Bellard, Edgard Rivera-Valentín, and Swetha Venugopal

Date	Speaker	Topic
June 9	Prajkta Mane	Meteorites and the Early Solar System
June 15	Edgard Rivera-Valentín	Asteroids: MBAs, NEAs, PHAs, Oh My!
June 22	Paul Schenk	Ice Worlds and Ocena Worlds in the Outer Solar System
July 6	Interns	Mid-Term Presentations
July 13	Walter Kiefer	Understanding the Evolution of Venus Modeling and Spacecraft Missions
July 20	Samuel Lawrence	NASA Artemis Science
July 27	Sean O’Hara	Planetary Lithospheres: Bending and Breaking
August 3	Kennda Lynch	Astrobiology: A Primer

LPI Summer Intern Program 2022 — Professional Development Seminar

Facilitated by Christine Shupla and Grace Beaudoin

Date	Speaker	Topic
June 10	Edgard G. Rivera-Valentín	The Business of Planetary Science Learn about how Planetary Science gets done and what career paths are available in the field.
June 23	Edgard G. Rivera-Valentín and Prajkta Mane	Presenting Your Research In preparation for the mid-term reports, you’ll be guided through our best practices.
July 15	Edgard G. Rivera-Valentín and Prajkta Mane	Ethics in Science Be exposed to ethical considerations in planetary science, particularly in the practice of research.
July 21	Edgard G. Rivera-Valentín - Moderator Evan Bjonnes, Justin Filiberto, Kennda Lynch, and Prajkta Mane	EDI in Planetary Science A diverse and equitable community can reach for the stars! Learn about the state of our profession and how we can improve.
July 28	Justin Filiberto	A How to Guide to Scientific Writing In preparation for your final project reports, you’ll be guided through our best practices for writing a scientific abstract.
August 8	Edgard G. Rivera-Valentín - Moderator Candice Bedford, Justin Filiberto, Kennda Lynch, and Prajkta Mane	Pursuing Graduate Studies in Planetary Science To prepare you for the application process, our panel will give you advice on how to apply and succeed in graduate school.

LPI Special Seminar

Facilitated by Claudia Bellard

Date	Speaker	Topic
August 9	Astronaut Don Pettit	Science of Opportunity in Space

LPI Intern Stories Series

Webinar facilitated by Grace Beaudoin

Date	Stories	Topic
June 21	Claudia Bellard Sedinam Bogart Daniel Burgin Emily Etheridge William Wallentine Garrett Wolff	During LPI Intern Stories 2022, you'll hear from LPI summer interns about how they applied and prepared for their internship, their ongoing experiences, and how the internship has helped them.

LPI Summer Intern Tours

NASA Johnson Space Center, Astromaterials Research and Exploration Science Division

Date	Speaker	Topic
July 7	Suzanne Foxworth and Kim Willis	Lunar Curatorial Laboratory
July 7	Chris Cline	Experimental Impact Laboratory
July 8	Suzanne Foxworth	Astromaterial Virtual Tour
July 18	Kevin Righter	Meteorite Laboratory

LPI Summer Intern Social Events

Movie/games facilitated by Evan Bjonnes and Swetha Venugopal

National Intern Day facilitated by Claudia Bellard and Delia Enriquez

Date	Event
June 8	Icebreaker
June 22	The Martian
June 29	Board Game Night
July 12	Fun Talks and Ice Cream Social
July 20	Murder Mystery
July 29	National Intern Day

LPI Summer Intern Alumni Event

Facilitated by Delia Enriquez and Julie Stopar

Date	Speaker
August 11	Evan Bjonnes Hannah O'Brien Nicole Nevill

AGENDA

Wednesday, August 10, 2022

9:30 a.m.

Chairs: Edgard Rivera-Valentín and Julie Stopar

Breakfast will begin at 8:45 a.m.

Time	Speaker	Presentation Title
9:30 a.m.	Gaddis L. and Filiberto J.	Introduction Address
9:40 a.m.	MOUTI AL-HASHIMI KEYNAB * Arizona State University Advisor: Mane P.	<i>Diversity of Calcium-Aluminum-Rich Inclusions in CV, CK, and CL Chondrites</i> [#4015]
10:00 a.m.	ETHERIDGE EMILY N. * Marietta College Advisors: Anzures B. A. Dygert N. Goodrich C. A. McCubbin F. M.	<i>Thermal Evolution of Enstatite Chondrite and Aubrite Parent Bodies</i> [#4013]
10:20 a.m.	BURGIN DANIEL L. * University of Otago Advisors: Crossley S. Goodrich C.	<i>A Mineralogic Investigation into the Onset of Core Formation in Highly Oxidized Asteroids</i> [#4012]
10:40 a.m.	CHAMPAGNE CHANSEY E. * University of Louisiana Lafayette Advisors: Rivera-Valentín E. G. Aponte-Hernández B. Taylor P. A.	<i>Automating Size Determination of Near-Earth Asteroids Using Low SNR Arecibo Radar Imaging</i> [#4003]
11:00 a.m.	WOLFF GARRETT M. * University of Colorado Advisors: Stopar J. D. Rivera-Valentín E. G.	<i>Roughness Variations at Different Scales Within Irregular Mare Patches on the Moon</i> [#4011].
11:20 a.m.	BICKHAM DAVID A. II * Sam Houston State University Advisor: Schenk P. M.	<i>Geologic Mapping of Smooth Plains on Dione: Insights into Resurfacing Processes on Icy Bodies</i> [#4010]
11:40 a.m.	NGUYEN ALEXANDER L. * Vassar College Advisor: McGovern P. J.	<i>The Role of Pluto's Ocean's Salinity in Supporting Nitrogen Ice Loads Within the Sputnik Planitia Basin</i> [#4007]
12:00 p.m.		Lunch Break
12:40 p.m.	MCKENNA THEA E. * Cornell University Advisors: Weller M. B. Kiefer W. S.	<i>Properties and Comparative Analysis of Venusian Rift Zones</i> [#4008]
1:00 p.m.	BOGART SEDINAM * University of Colorado Boulder Advisor: Treiman A. H.	<i>The Distribution and Volume of Impact Melt, Cleopatra Crater, Maxwell Montes, Venus</i> [#4006]
1:20 p.m.	ROBERTS EMILY R. * Lunar and Planetary Institute Advisors: Treiman A. H. Eggers G. L. Filiberto J.	<i>Multiple Tectonic and Volcanic Events: Gina Crater Area, Venus</i> [#4002]
1:40 p.m.	GAMBRILL JACOB G. * Embry-Riddle Aeronautical University Advisor: Martínez G. M.	<i>Analyses of Curiosity's Ground Temperature Measurements: Correction for Thermal Noise</i> [#4009]

Time	Speaker	Presentation Title
2:00 p.m.	WESTENBERG MADDIE R. * University of Minnesota Twin Cities Advisors: Rivera-Valentín E. G. Lynch K. L. Kring D. A.	<i>Evaluating Boiling Curves and Their Implications for Impact-Generated Hydrothermal Systems on Mars [#4001]</i> [REMOTE PRESENTATION]
2:20 p.m.	GARCIA FRIDA D. * University of Texas at El Paso Advisors: Bedford C. C. Tu V. Rampe E. Thorpe M.	<i>Investigating Source to Sink Processes on Earth to Connect to Mars [#4004]</i>
2:40 p.m.	WALLENTINE WILLIAM L. * Wesleyan University Advisors: Lynch K. Eggers G.	<i>Investigation of Great Salt Lake Evaporite Spectra for Evidence of Mirabilite and Thenardite [#4005]</i>
3:00 p.m.		<i>Closing Remarks</i>
3:15 p.m.		<i>Group Photos</i>
3:30 p.m.		<i>Adjourn</i>

CONTENTS

Geologic Mapping of Smooth Plains on Dione: Insights into Resurfacing Processes on Icy Bodies <i>D. A. Bickham and P. M. Schenk</i>	1
The Distribution and Volume of Impact Melt, Cleopatra Crater, Maxwell Montes, Venus <i>S. Bogart and A. H. Treiman</i>	4
A Mineralogic Investigation into the Onset of Core Formation in Highly Oxidized Asteroids <i>D. L. Burgin, S. Crossley, and C. Goodrich</i>	7
Automating Size Determination of Near-Earth Asteroids Using Low SNR Arecibo Radar Imaging <i>C. E. Champagne, E. G. Rivera-Valentín, B. Aponte-Hernández, and P. A. Taylor</i>	10
Thermal Evolution of Enstatite Chondrite and Aubrite Parent Bodies <i>E. N. Etheridge, B. A. Anzures, N. Dygert, C. A. Goodrich, and F. M. McCubbin</i>	13
Analyses of Curiosity's Ground Temperature Measurements: Correction for Thermal Noise <i>J. G. Gambrill and G. M. Martínez</i>	16
Investigating Source to Sink Processes on Earth to Connect to Mars <i>F. D. Garcia, C. C. Bedford, V. Tu, E. Rampe, and M. Thorpe</i>	19
Properties and Comparative Analysis of Venusian Rift Zones <i>T. E. McKenna, M. B. Weller, and W. S. Kiefer</i>	22
Diversity of Calcium-Aluminum-Rich Inclusions in CV, CK, and CL Chondrites <i>X. Mouti Al-Hashimi and P. Mane</i>	25
The Role of Pluto's Ocean's Salinity in Supporting Nitrogen Ice Loads Within the Sputnik Planitia Basin <i>A. L. Nguyen and P. J. McGovern</i>	28
Multiple Tectonic and Volcanic Events: Gina Crater Area, Venus <i>E. R. Roberts, A. H. Treiman, G. L. Eggers, and J. Filiberto</i>	31
Investigation of Great Salt Lake Evaporite Spectra for Evidence of Mirabilite and Thenardite <i>W. L. Wallentine, K. Lynch, and G. Eggers</i>	33
Evaluating Boiling Curves and Their Implications for Impact-Generated Hydrothermal Systems on Mars <i>M. R. Westenberg, E. G. Rivera-Valentín, K. L. Lynch, and D. A. Kring</i>	36
Roughness Variations at Different Scales Within Irregular Mare Patches on the Moon <i>G. M. Wolff, J. D. Stopar, and E. G. Rivera-Valentín</i>	39

Geologic Mapping of Smooth Plains on Dione: Insights into Resurfacing Processes on Icy Bodies. D. A. Bickham¹ and P. M. Schenk², ¹Sam Houston State University Department of Environmental and Geosciences, Huntsville, TX 77340, ²Lunar and Planetary Institute, Houston, TX 77058.

Introduction: While not as well-studied as its siblings Titan and Enceladus, Saturn's icy moon Dione is a geologically interesting and complex body that holds secrets to how geologic and resurfacing processes occur on icy bodies. One of the key features of Dione is its smooth plains, a relatively flat and lightly cratered region that is centered on its leading hemisphere [1][2][3]. This region stands in stark contrast to the heavily cratered and more rugged trailing hemisphere. Among the hypotheses for this resurfacing are water-rich volcanism and pervasive relaxation by high heat flow. These plains offer additional opportunity examine resurfacing processes on icy bodies, in comparison to resurfacing on Charon, Ganymede, Enceladus and others.

Methods: In order to test possible formation mechanisms, we first map both the potential extent of resurfacing as well as any geologic structures that exist in relation to it. While geologic maps of Dione already exist, such as that made by Stephan et. al. [4], the mapping products used here were not available as well as lacking preferred detail. As such, we have created a more detailed map independently from previously existing versions based on data from Cassini.

Geologic mapping of Dione was based on a global mosaic at 250m/pixel, stereo-images, a DEM at 400m/pixel that was made from the stereo-images, a slope map and a crater density map, all derived from Cassini data. These mosaics were then uploaded into ArcGIS for analysis.

Results: Our mapping of the leading hemisphere confirmed that the smooth plains are a geologic complex and varied landscape. With a few exceptions, the different features will be grouped together based on inferred relationship with each other and discussed as a whole.

Central Trough Belt: One of the dominant features of the leading hemisphere plains is a series of roughly north-south aligned troughs that run from the north pole across the center of the hemisphere that ends in a horsetail like trough network. This trough belt consists primarily of two parallel troughs with several secondary troughs either branching off or in close proximity to the primary troughs. The troughs in the belt range from ~300m to greater than 1500m deep, with the deepest lying in the north and the shallowest lying in the horsetail network.

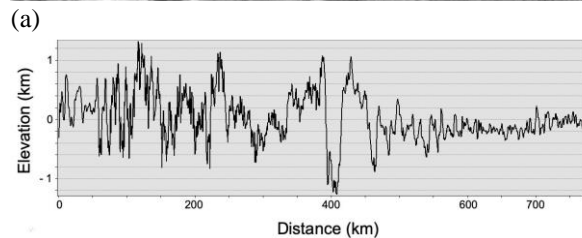
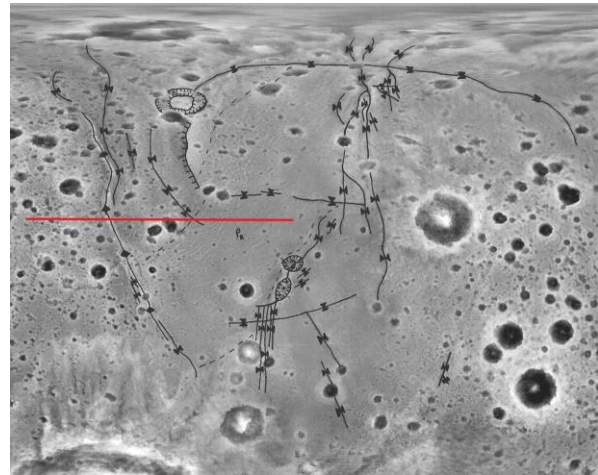


Fig. 1. Geologic map of Dione showing major features (a) and topographic profile showing major change in ruggedness from cratered plains to smooth plains from left to right (red line, b). Geologic map is on the global DEM of Dione. North is top. Largest Crater is ~175 km across.

The central trough belt shows an en echelon in the network just north of the equator. When looking at where the two troughs are in the same lines of latitude, we see not only the two main troughs but also a third, smaller trough between them. These three troughs all show the same S-like shape directly in line with each other. This pattern suggests that these troughs are most likely a part of one system that formed at the same time. Although mostly in a north-south orientation, there are a few cross-cutting troughs in the center and southern portions of the system. While these troughs could be a part of the same system, they also appear to be radial to Aeneas to the east and their origin is unclear.

Central Patera: The central trough belt also intersects two distinct paterae in the southern section, Metiscus and Murranus Patera. These paterae are

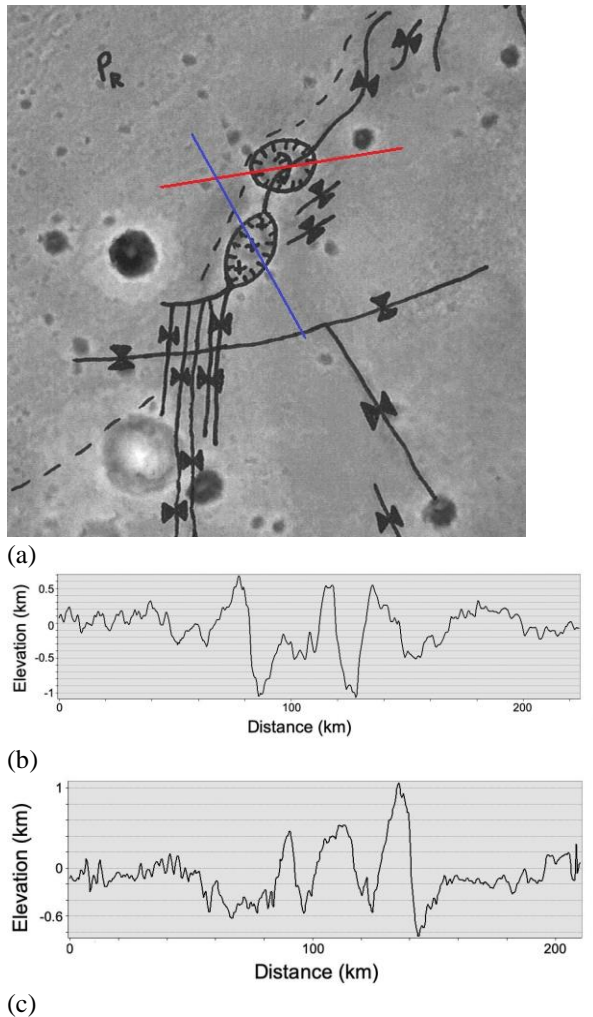


Fig. 2. Close up view from Fig. 1 of central paterae and troughs on Dione's smooth plains (a) with topographic profile of northern patera (red line, b) and southern patera (blue line, c). Map is on global DEM of Dione.

situated in the center of the plains and are the dominant feature of this area. The paterae are characterized by raised rims, shallow floors and non-circular shapes. Although the raised rims and shallow floors could indicate relaxed craters, the odd shapes of the two paterae, as well as their spatial association with the central trough belt suggests an endogenic origin.

The northern patera is the more circular of the two but has a nested smaller patera within it offset to the southwest. The southern patera has an oval shape with three mounds ~1000m high, aligned through the center of it. The two paterae are also connected by a trough that is bordered on either side by a ridge that matches the height of the patera rims. The paterae also sit within a localized shallow depression ~500m deep.

These observations indicate that it is unlikely that these paterae are the result of an asteroid impact. Although not conclusive, the shapes and morphologies of the paterae and their association with the troughs suggests a volcanic origin. Additionally, the paterae most likely formed contemporaneously with the central trough belt rather than predating it.

Northwestern Ridge and Trough Belt: To the northwest of the central trough is a zone that consists of a singular ridge and several north-south trending troughs. The ridge itself is the only one found on Dione [5], is ~750km long and ~1500m tall. The ridge is also flanked on either side by several troughs. While none of them extend the full length of the ridge, the longest of the troughs do extend past the furthest extent of the ridge. One extends to the south and one to the north, ending near the north pole.

East of the ridge are a few more troughs and a scarp. The largest scarp is ~200km long and has a vertical displacement upward of 2000m to the east. North of the scarp lies a quasi-circular feature, and north of that is a trough that extends westward and cuts through the central trough belt in its northern section. It cannot be determined which trough crosscuts the other due to the existence of a crater directly on top of the point of intersection.

Between the ridge and the scarp is a down-dropped section of terrain that exhibits greater relief and crater density than the resurfaced plains. While this might indicate that this section is the oldest of the smooth plains, it is uncertain if that means the same for the ridge and troughs that cut through it.

Quasi-circular feature: The quasi-circular feature just north of the fault scarp is a large, walled depression with a domed floor. While this feature could be a relaxed crater, it has some distinct differences. The raised floor of the feature most resembles a rounded dome while relaxed craters are more conical. While the feature could have formed contemporaneously with the fault scarp and trough that it lies between, its true origin and timing remain uncertain.

Ridged Plains: Between the northwestern ridge and trough belt and the central trough belt, the low relief resurfaced plains are characterized by a series of parallel, close-spaced ridges. These ridges are only a few hundred meters high. Elsewhere, the smooth plains lack a ridged morphology. While the cratered plains are on the order of ≥ 4 Ga old, the ridged and smooth plains may be as young as ~1.5 Ga [6].

Discussion: With a more updated geologic map of Dione, we can now compare Dione to other icy bodies such as Charon, Enceladus and Ganymede to gain new insights into how icy bodies function geologically.

Stratigraphic Sequence: Due to the few numbers of crosscutting structures and inability to perform other classic tests for relative ages, it's difficult to determine the ages of many features. However, there are some relations that can be derived.

The central trough belt, paterae and northwestern ridge and trough belt cut through the smooth plains, suggests that these features all formed after the smooth plains had. As for the ridged plains, due to appearing to neither cutting or being cut by the two belts, it is difficult to determine if the parallel ridges predate the other structures or postdate.

When looking at the central trough belt and the northwest ridge and trough belt, it is difficult to determine which predates the other. The two belts only seem to intersect in a single location. While this would normally allow the determining the relative ages of both structures, there exists a crater in the precise location of the intersection.

Within the smooth plains, there does appear to be a definable boundary between the ridged plains and non-ridged plains. Based on out mapping, it appears that the ridged plains end at the western edge of the central trough belt, with the smooth plains beginning on its eastern edge. The outer margins of the plains are poorly defined, however. Crater densities and slopes appear to increase gradually from smooth plains to cratered plains.

Comparisons: We compared resurfacing on Dione with other ice bodies, namely Ganymede, Charon and Triton. Although Dione's resurfaced plains share some common features (patera, plains, troughs), these bodies are distinctly different in their patterns, morphologies and sequences of features. For example, no paterae have been recognized on Charon, but the trough system on Dione appears more "organized" into two north-south trending systems than on Charon. Paterae on Dione are closed and not associated with bands of bright terrain as on Ganymede.

Mechanism: Currently there are two possible hypotheses to explain the formation of the smooth/ridged plains on Dione: burial by water lava or a large series of such flows, or a hemispherical "hotspot" that either softened or fully melted the area. While both hypotheses can explain the resurfaced plains, neither do so in a fully satisfying way.

The lava flow hypothesis is based around the existence of the paterae and associated troughs in the center of the plains. Whether in numerous smaller bursts or as a few large ones, the lava would extend over the entirety of the plains, filling in the pre-existing craters. However, in this case, one would expect relic crater rims from craters that were not fully filled in. We would then see more and more craters

that were just partially filled in as we move from the patera to the outer edge of the plains. Not only is this gradient of fully filled craters, relic crater rims and partially filled craters absent, there's no presence of such craters at all. As a result, the lava flow hypothesis can't satisfactorily explain the resurfaced plains.

Alternatively, instead of lava simply covering the surface, there could have been a regionalized increase in thermal energy that would have heated the surface. This heating would have occurred to such an extent that it would have relaxed the craters to the point of disappearing completely. Alternatively, this thermal energy would be so high, it would have completely liquified the surface, creating a magma ocean. This magma ocean would have then cooled, leaving behind a smooth surface. Although both heat flow hypotheses are different from the lava flow hypothesis, both still suffer from a similar problem. Due to the nature of heat flow, as you move from the center of a heat source away from it, the thermal energy decreases gradually. In the context of crater relaxation, there will be a decreasing heat flow from the center and a gradual increase in the number of relaxed craters and the magnitude of crater relaxation. However, when looking at the resurfaced plains on Dione, there is no evidence for such a pattern of crater relaxation. There are a few relaxed craters [7], but there are too few to support this hypothesis. Instead, almost all of the craters in and near the margins the resurfaced plains appear to be mostly pristine. Therefore, the hemispherical "hotspot" hypothesis also cannot account for the resurfacing on its own.

Since neither hypothesis survive their tests, there is likely a third, as yet undefined, mechanism for these plains. Alternatively, there could be multiple processes occurring together that generated this terrain. Until such a process is determined, the origin of these plains will remain a mystery.

Future Work: Future work will include determining stratigraphic units on Dione via slope maps, crater density maps, high resolution topography and other methods we will also compare and contrast resurfacing Dione with other icy bodies in the solar system in great detail, including paterae on Triton and Ganymede, plains on Charon and Ariel and troughs on Charon and Enceladus.

References: [1] Moore J. M. (1984) *Icarus*, 59, 205-220. [2] Plecia J. B. (1983) *Icarus*, 56, 255-277. [3] Schenk P. M. et. al. (2018) *Enceladus and the Icy Moons of Saturn*, 237-265. [4] Stephan K. et. al. (2009) *Icarus*, 206, 631-652. [5] Hammond N. P. et. al. (2013) *Icarus*, 223, 418-422. [6] Kirchoff M. R. and Schenk P. M. (2015) *Icarus*, 256, 78-89. [7] White et. al. (2017) *Icarus*, 288, 37-52.

THE DISTRIBUTION AND VOLUME OF IMPACT MELT, CLEOPATRA CRATER, MAXWELL MONTES, VENUS. S. Bogart^{1,2} and A. H. Treiman¹, ¹Lunar and Planetary Institute, 3600 Bay Area Blvd, Houston, TX, 77058. ²University of Colorado Boulder (sebi8707@colorado.edu).

Summary: *We mapped the lava-filled valleys east and downslope of the Cleopatra impact crater, and calculated the volume of the valley-fill. It is less than half the volume of Cleopatra itself, but a significant portion of the volume of impact melt calculated for the crater (at Venus surface temperature) [4]. Among possible explanations for the relatively large volume of valley-fill melt are: that site had a high geothermal gradient, that the impact was near-vertical, and the target rock was not basalt.*

Introduction: The Cleopatra Crater is arguably one of the most interesting features on Venus. Located at approximately 65.9°N, 7.0°E (Figure 1), the crater sits on the eastern slope of the Maxwell Montes Mountain Range in Ishtar Terra. Maxwell's highest peak is 11 km above Venus' mean radius and is the highest point on the planet. Cleopatra's outer rim is approximately 100 km in diameter. Its inner peak ring is approximately 50 km in diameter and is slightly offset west-northwest of the crater's center [1]. The eastern rim of the crater is cut by a channel (Anuket Valles), which feeds into an area of valleys and ridges. The valleys downslope of the channel are filled with material inferred to be melt from Cleopatra [2]. Anuket Valles itself is unusual because few channels on Venus incise and breach crater rims.

Cleopatra was first imaged in Venera 15 and 16 radar images, and there was controversy about whether it was of volcanic or impact origin. Its double-ring structure was similar to those of multi-ring impact craters on the Moon and elsewhere on Venus, tipping the scale towards the impact origin hypothesis. However, the absence of a raised rim and the volume of the outflow material supported the argument that Cleopatra was of volcanic origin. In addition, the depth of the crater (2.5 km) is unusual for an impact crater of its size [2,3].

Radar images from the Magellan orbiter resolved the controversy, showing conclusively that Cleopatra is an impact crater, relatively unmodified since its formation [1,3]. Magellan images also showed that fluid from Cleopatra had breached its rim and flowed downslope to fill many valleys. The channel, Anuket Vallis, cuts through the rim, the crater wall, the peak ring, all the way to the radar dark crater floor.

Method: To determine the volume of melt that flowed out of Cleopatra crater, we mapped the downslope region of filled valleys east of the crater (Figure 2). The base map was the Magellan SAR left look global mosaic (75 m per pixel); elevations were from both the Magellan altimetry global mosaic and the

Magellan stereo digital elevation model (DEM) [7]. The mosaics were downloaded from the Astrogeology USGS website [5] and imported into ArcMap. The JMARS web interface was also used for visualizing the region.

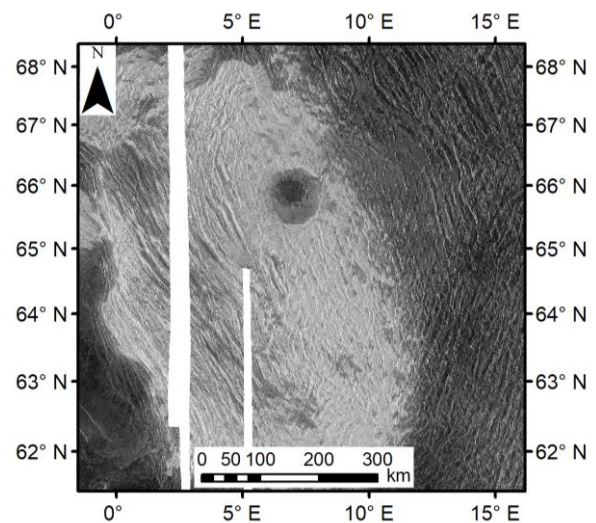


Figure 1. Regional image showing longitudinal and latitudinal position of Cleopatra on Maxwell Montes.

Extents of the melt fill were mapped onto the Magellan SAR image. The valleys containing fill were segmented into rectangles (Figure 3). To calculate the fill volume, we estimated the shapes of the valleys using the DEM of nearby areas, as the DEM does cover the filled valleys, and Magellan altimetry does not have adequate spatial resolution. To model the shapes of the valleys, we used DEM elevation profiles across comparable valleys on the northern, southern, and western regions of Maxwell Montes. After removing regional gradients, we found that the valleys were basically symmetrical with slopes of $\sim 6^\circ$ on both east and west facing sides. The volume of each rectangular area was calculated then as a triangular prism model (Figure 4). The volumes of Cleopatra crater, inside and outside the peak ring, were calculated from simple geometry.

Expected volumes of impact melt from the Cleopatra impact were calculated from the equations of [4] (esp. 12 & 18), assuming (as he did) an impactor with a density of 3320 kg/m^3 travelling at a velocity of $17,000 \text{ m/s}$ [4]. A final crater diameter of 100 km (like Cleopatra) implies a transient crater diameter of $\sim 75 \text{ km}$. We calculated the melt volume for such an impact for granitic and basaltic target rocks on Venus, using

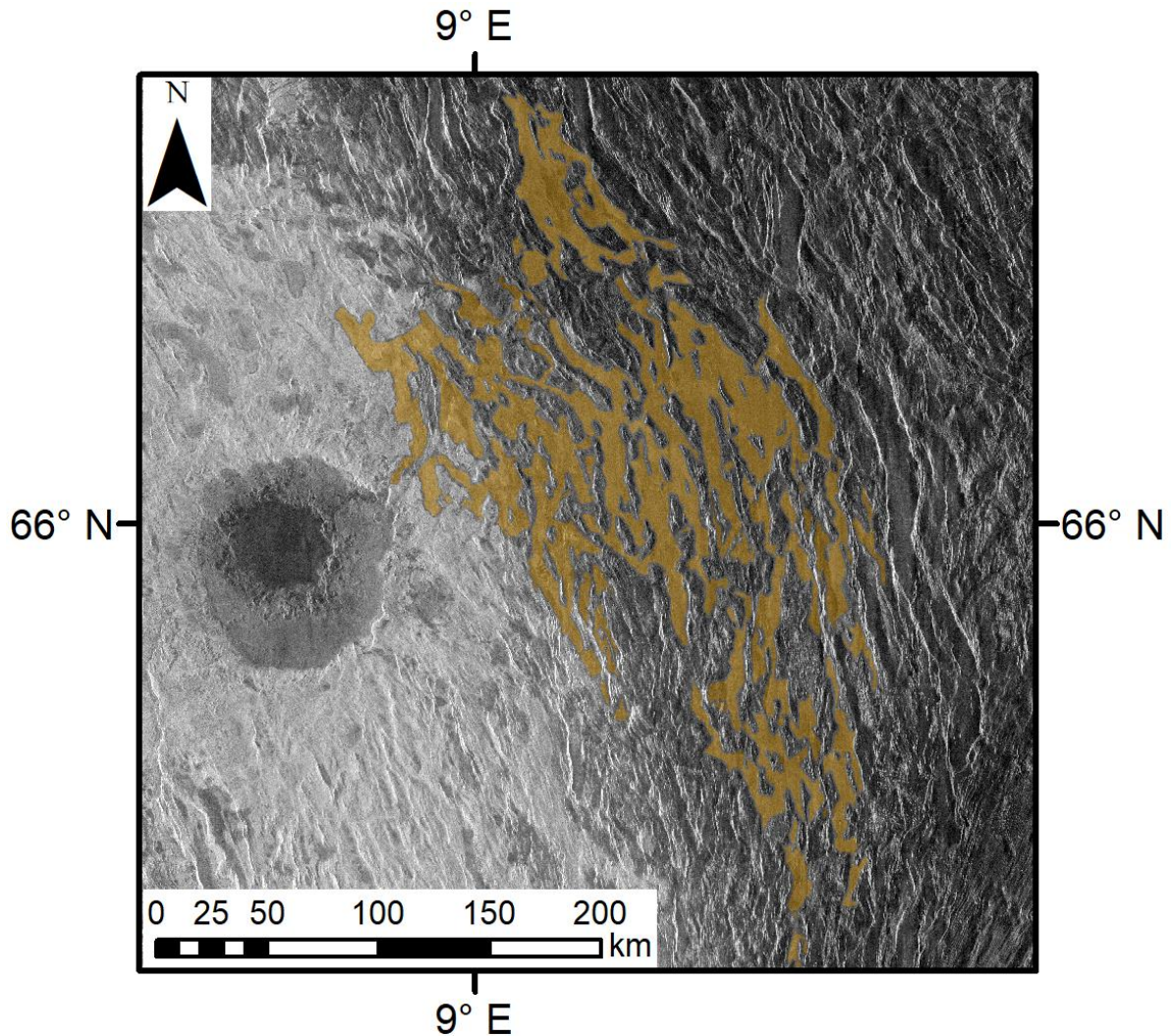


Figure 2. Melt-filled valley floors (brown) east of Cleopatra Crater.

Venus' surface gravity and temperature (740K), and a range of thermal gradients (dT/dz). Melt volumes were calculated for impacts at both 45° (most probable) and 90° (vertical) for Venus. The thermal properties of the target rocks and typical impactor are from [4,6].

Results: *Volume of valley-fill melt:* The east and west facing slopes of the region were at an average of 6° , and the total volume of the lava fill was approximately 4500 km^3 .

Volume of Cleopatra: The volume of the crater from the rim to the outer ring floor was approximately 7850 km^3 . Inside the peak ring to the inner floor of the crater, the volume was approximately 1800 km^3 .

Melt volumes from crater scaling: The estimated melt volumes for granitic and basaltic rocks on Earth and Venus are given in Table 1.

Discussion: Questions to consider are whether the appearance and the volume of the valley-fill are

consistent with the appearance of typical impact crater melt, as well as the volume of melt produced by a crater like Cleopatra.

Appearance: Impact melt is usually rough as it is mixed with fragments of rock. From the radar images, we see that the fill has a relatively smooth texture. A few craters on Venus, for example the Wu Hou crater, are surrounded by rough impact ejecta, with a smoother and radar dark material on the outside. One assumption could be that the impact melt was partly molten and then deposited the rougher and fragmented parts as it continued to flow downslope. If the fill that occupies the valleys east of Cleopatra is impact melt from the crater, then it would have had to be extensively filtered. The valley-fill next to Cleopatra, however, does not show any remnants of larger rock fragments.

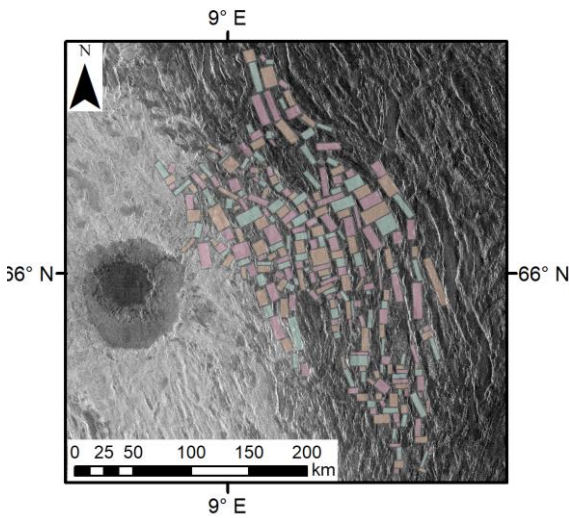
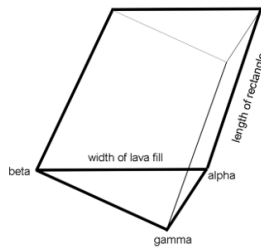


Figure 3. Rectangular segments used to calculate volume of valley-fill melt.

Figure 4. Triangular prism model



Volume: The channel at the crater rim most likely started there, initiated by melt overflowing the crater rim, and so the fluid that

created it would have been at or near the edge of the crater. This implies that Cleopatra was initially full or nearly full of melt. If the crater floor inside the peak ring were at the elevation of the floor between the rim and peak ring (the annulus), then volume of valley fill would have filled the crater to a depth of ~0.6 km. The crater rim is approximately 1 km above the floor of the annulus, so the crater would have been approximately half-full of impact melt. If the crater wall had a low spot, it is possible that the melt could have topped that low spot, and eroded through the rim to allow crater to drain.

A possible simplification of this scenario is that Cleopatra was not so deep as it is now. There is evidence that the floors of large Venus craters have subsided significantly as the heat of impact dissipates [8]. In this case, the crater would have been filled more than the above estimate, so its melt could have been high enough to breach the crater rim and flow down to fill the valleys. Since then, the melt that remained inside the floor would have cooled down, causing the crater floor to subside to the level it is presently.

Conclusion: From our calculations, the volume of the valley-fill melt is comparable to the total impact

Table 1. Calculated Impact Melt Volumes:

Planet	Target Rock	dT/dz (K/km)	Impact angle (°)	Melt Volume (km ³)
Earth	Basalt	25	45	16000
	Granite	25	45	30000
Venus	Basalt	25	45	6000
	Granite	25	45	14000
	Basalt	5	45	5000
	Granite	5	45	9000
	Basalt	25	90	11000
	Granite	25	90	26000
	Basalt	5	90	8000
	Granite	5	90	15000

Calculated from equations 12 & 18 of [4]. 100 km diameter final crater; 75 km diameter transient crater. dT/dz is geothermal gradient; 90° impact angle is vertical. Surface temperatures: Earth, 287K; Venus, 740K. Thermal parameters from [4,6].

melt produced by a Cleopatra-sized crater assuming the target material was basalt, had a low geothermal gradient, or was impacted at a 45° angle. This would imply that all or almost all the impact melt produced by Cleopatra flowed out of the crater, which is unlikely. The volume of the fill, however, is about a third to a quarter of the total melt produced if the target material was granitic, although that is not definitive. This is also consistent with a 90° impact angle and a higher geothermal gradient. This implies that about half the volume of melt produced could have cut through the crater rim and flowed out of the channel, which is a more reasonable assumption. The volume of the fill is large enough that it suggests that the target material was granitic, had a higher geothermal gradient, or that it was impacted at a more vertical angle. Either one or a combination of these conditions would be a more probable answer.

Acknowledgments: We thank the LPI/USRA for sponsoring the first author’s Summer Internship. We are also grateful to Drs. D. Kring and E. Bjornnes for assistance with impact cratering processes. Treiman’s participation was supported in part by NASA grant 80NSSC17K0766.

References: [1] Herrick R. R. and Rumpf E. M. (2011) *JGR*, 116 p. E02004. [2] Grieve R. A. F. and Cintala M. J. (1995) *Icarus* 114, 68-79. [3] Basilevsky A. T and Schaber G. G. (1991) *LPSC XXII*, 59-60. [4] Abramov O. et. al (2012) *Icarus* 218, 906-916. [5] <https://astrogeology.usgs.gov/search?pmi-target=venus> [6] Bouhifd M. A. et. al (2007) *Contributions to Mineralogy and Petrology*, 153, 689-698. [7] Herrick R.R. (2012) *EOS* 93(12) 125-126. [8] Brown C. D. and Grimm R. E. (1996) *JGR*, 101, 26057-26067.

A MINERALOGIC INVESTIGATION INTO THE ONSET OF CORE FORMATION IN HIGHLY OXIDIZED ASTEROIDS. D. L. Burgin^{1,2}, S. D. Crossley^{1,3}, C. A. Goodrich¹, ¹Lunar and Planetary Institute (USRA), Houston, TX 77058, USA, ²Department of Geology, University of Otago/Te Whare Wānanga o Ōtākou, Dunedin, Aotearoa/New Zealand, ³Astromaterials Research and Exploration Sciences, NASA Johnson Space Center, 2101 NASA Parkway, Houston, TX, USA.

Introduction: Redox conditions in the solar nebula were a major factor for controlling the type of core forming minerals available during asteroid and planet growth. Studies of core formation have typically focused on reduced material, which contain abundant Fe-Ni metal. In these settings, segregation of metal requires extensive melting of silicates (>1100°C [1]). The process of core formation from oxidized material, that lacks Fe-Ni metal, is poorly understood yet may have occurred in oxidizing regions of the protoplanetary disk.

The mineralogy of core forming minerals (Fe-oxides and sulfides) in oxidized chondrites can be used to explore if core formation can occur and how melting would first initiate. CK chondrites are the most oxidized chondrite group in the terrestrial meteorite collection (FMQ +2.0 to FMQ +5.1 [2]). Petrologically, this is evidenced by a lack of Fe-Ni metal where Fe has oxidized to form abundant magnetite, FeO-rich silicates, and Fe-sulfides [3,4].

This study characterizes the major element concentrations of the opaque phases (magnetite and sulfides) in CK chondrites to determine the bulk opaque composition. We use the bulk opaque composition to determine the petrogenesis of sulfides and investigate melt pathways.

Methods: Three CK chondrite thin sections were obtained for this study, EET 87860 (CK5/6), EET 90015 (CK5), and DOM 19035 (CK6). Initial observations were undertaken using a Leica DMX-R petrographic microscope at the Lunar and Planetary Institute (LPI).

Backscatter electron (BSE) images were acquired using a Phenom XL scanning electron microscope (SEM) at the LPI. Semi-quantitative analyses of major element concentrations were also carried out for preliminary characterization of phases in the CK chondrites.

Quantitative analyses of major element concentrations in opaque phases were obtained using a CAMECA SX-100 electron microprobe (EMPA) and a JEOL JXA-8350 EMPA at NASA's Johnson Space Centre (JSC). Analyses were calibrated against sulfide and Fe-oxide standards. The operating conditions were an accelerating voltage of 15 kV and sample current of 20 nA.

Electron dispersive spectroscopy (EDS) x-ray element maps were acquired using a JEOL 7600F field emission SEM at JSC.

Modal mineralogy of opaque phases was calculated by pixel counting using ImageJ. Fe, Ni, and S EDS maps were converted to RGB maps. Pixel counting was conducted using ImageJ's color threshold tool. Parameters for each opaque phase were first determined by defining regions of interest (ROIs) and then parameters for each color channel were adjusted manually to ensure all constituents of that phase were included. Each count was repeated three times using different ROIs and the number of pixels per phase was averaged.

Bulk sulfide and bulk opaque compositions were calculated using the modal mineralogy and averaged EMPA analyses for each phase. Only stoichiometric endmember compositions with wt% totals >90% were used for calculating bulk opaque compositions.

Results: The opaque assemblage consists of magnetite and sulfides. Sulfides predominantly occur as pentlandite-pyrite assemblages with magnetite, and as small inclusions within silicates (Fig. 1).

EET 87860. Opaque minerals in EET 87860 are 9.8 vol% and are: magnetite = 82 vol%, pentlandite = 15 vol%, and pyrite = 3 vol%. A single Co-rich pentlandite grain was also observed in this sample.

Pentlandite compositions in EET 87860 average 23 at% Fe, 28 at% Ni, and 48 at% S (n = 133). Pyrite compositions average 34 at% Fe and 64 at% S (n = 68). EET87860 has the most Ni-rich bulk sulfide compositions of the three samples, 25 at% Fe, 23 at% Ni, and 51 at% S.

DOM 19035. The opaque assemblage in DOM 19035 is 7.3 vol% and consists of: magnetite = 77 vol%, pentlandite = 11 vol%, and pyrite = 12 vol%.

Pentlandite compositions average 24 at% Fe, 27 at% Ni, and 48 at% S. (n = 34). Pyrite compositions average 34 at% Fe and 65 at% S (n = 13). The bulk sulfide composition is 29 at% Fe, 13 at% Ni, and 56 at% S.

EET 90015. Opaque phases in EET 90015 are 8.7 vol% and are: magnetite = 75 vol%, pentlandite = 9 vol%, and pyrite 16 vol%. Pyrite and pentlandite are only present as very fine-grained, possibly shock melted, patches (Fig. 1B) and were below the resolution of the EDS maps.

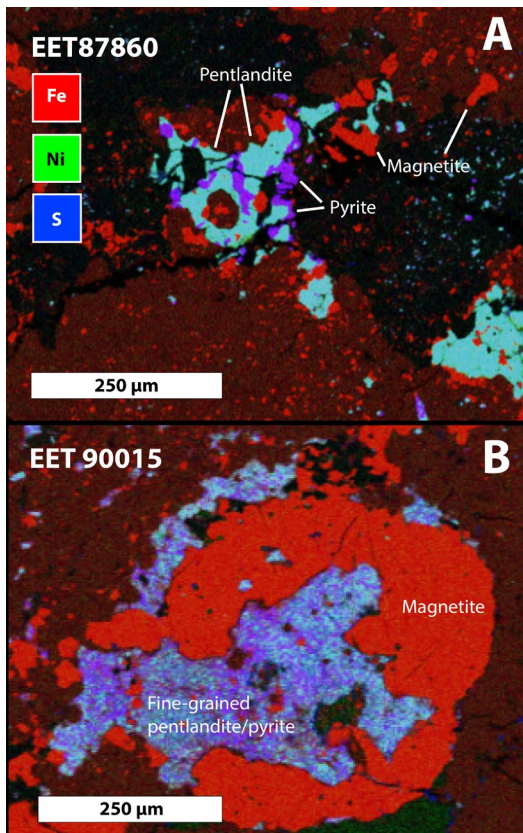


Figure 1: Combined RGB EDS maps of the opaque phases in pyrite EET 87860 (A), and EET 90015 (B).

Pyrite compositions in EET 90015 average 34 at% Fe and 62 at% S ($n = 26$). Pentlandite compositions average 26 at% Fe, 26 at% Ni, and 37 at% S ($n = 44$). The bulk sulfide composition is 31 at% Fe, 10 at% Ni, and 57 at% S, similar to DOM 19035.

Discussion: Formation of sulfides: Fe, Ni, and S initially existed within the protoplanetary disk in gaseous form. Condensation to Fe-rich metal and later sulfidation and oxidation formed sulfides and FeO (in silicates) [5].

The greater modal abundance of pentlandite in EET 87860 relative to DOM 19035 and EET 90015 likely reflects a higher fO_2 for the former [4] as sulfides incorporated more Ni as less Fe was available [3].

Metamorphic history: CK chondrites experienced calculated two-pyroxene metamorphic temperatures of 647 – 867°C for the CK4-5 [6] and 740 \pm 38°C for a CK6 [4]. Pentlandite-pyrite assemblages are not stable above 400°C and will breakdown to form crystalline monosulfide solid solution (MSS) (Fig. 2). At metamorphic temperatures, the stable sulfide phase of EET 87860 was MSS \pm high-T pentlandite (Fig. 3). Subsequent cooling at or below 230°C caused MSS to break down and exsolve pyrite-pentlandite assemblages (Fig. 2b) [7] with textures including blocky pentlandite with pyrite islands (Fig. 1a) [4].

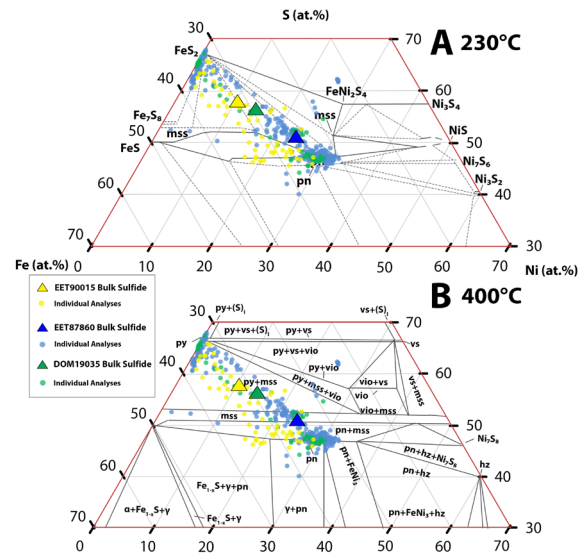


Figure 2: Fe-Ni-S phase diagrams adapted from [4] at 230°C (A [7]), and 400°C (B [8]).

The stable sulfide phases of DOM 19035 and EET 90015 at 800°C, within the upper limit of estimated CK metamorphic temperatures, are MSS and liquid S \pm vaesite (Fig. 3B) [9]. Liquid S, while stable in simple Fe-Ni-S melting experiments, will react with olivine to form orthopyroxene, Fe-sulfide, and O₂ gas. Sulfidation of CK olivine during metamorphism has been proposed in previous work [10] to account for reaction textures of low-Ca orthopyroxene and sulfides, but the sulfidizing agent could not be constrained. Thermal decomposition of pyrite during metamorphism in the CK parent body provides a candidate for the sulfidizing agent at relevant metamorphic temperatures. Closure temperatures for these reaction textures were calculated using two-pyroxene thermometers and yielded uniform closure temperatures of \sim 740 \pm 30°C [10], coincident with the thermal decomposition of pyrite [11].

At temperatures of 400 – 750°C (Figs. 2 & 3), the stable sulfide phases for DOM 19035 and EET 90015 are MSS \pm pyrite \pm vaesite. Exsolution of pentlandite and pyrite from MSS occurred at 230°C. [4] determined that the sulfides in the CK4 chondrites formed from annealing at 230°C, consistent with observations for CK5-6 in this work. However, they determined that sulfides in CK5-6 chondrites formed at 500°C due to the presence of MSS, which is inconsistent with our results. This may illustrate that CK5-6 chondrites possess differing cooling histories from impact fragmentation and reassembly.

Melting Behavior: The Fe-S-O phase diagram of [12] is used here to determine the initial melt behavior during core formation in the CK parent body. During

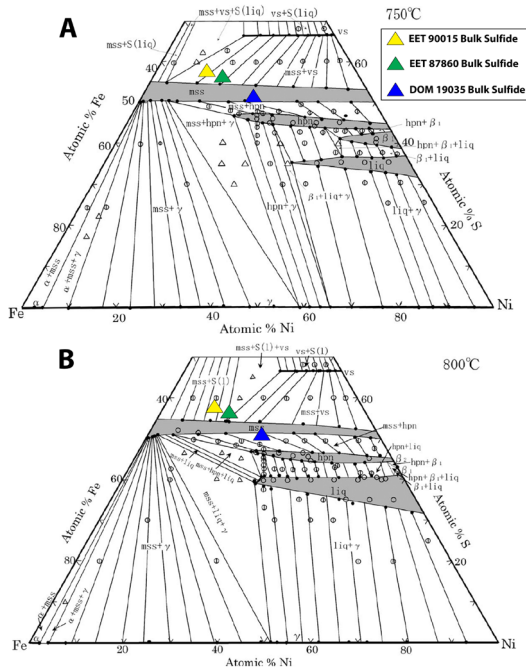


Figure 3: Fe-Ni-S phase diagrams at 750°C (A) and 800°C (B), from [9].

melting, liquid would form earlier in EET 90015 and DOM 19035 than in EET 87860 because liquid S would form at ~800°C in the former.

Melts would first form in EET87860 at the 934°C eutectic point with compositions of 25 wt% S, 8 wt% O, and 67 wt% Fe (Fig. 4). In EET 90015 and DOM 19035, following the reaction of liquid S with olivine, melts would follow a similar pathway. Continued melting would first consume MSS, which would melt completely by ~1,150°C [11], after which the composition of the melt would evolve towards magnetite, which itself would not completely melt until >1,400°C. Melting in the magnetite-dominated composition space is poorly constrained and the reactions that may occur between magnetite and sulfide melts are not known.

The initial, sulfide-dominated melts have an anion:cation ratio of 1.07, and therefore, a suitable

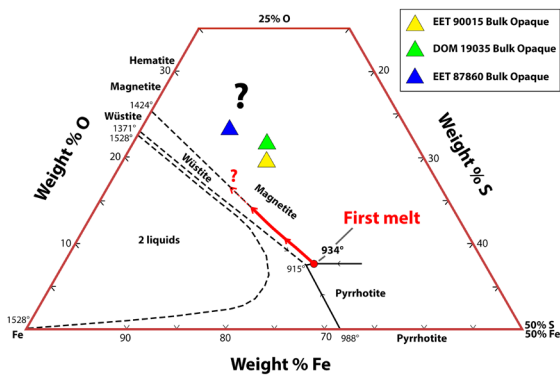


Figure 4: Fe-S-O phase diagram, from [12]

dihedral angle for grain boundary wetting [13,14]. However, the maximum amount of melt possible, prior to the silicate eutectic, would be the entire sulfide fraction; <2.2 vol %. Connected melt networks, needed for core formation via percolation, require a melt fraction of at least 4 vol% [15]. Therefore, core formation in the CK parent body would not be able to occur through percolation via connected melt networks. Melting above the silicate eutectic would be required for segregation of magnetite melt.

Sulfide melts in the R chondrites (FMQ -3.5 to FMQ; [2]) can begin migrating by percolation and form an oxidized core at temperatures as low as 865°C [16]. The work here suggests that there is a point at which high fO_2 inhibits core formation by percolation due to an overabundance of magnetite and underabundance of sulfides.

Future work: Further melting experiments that constrain melting in the magnetite-dominated region of the Fe-S-O system and explore liquid S/magnetite interactions to better determine initial melt behavior in the CK parent body. The extent of local sulfur redistribution could be investigated by trace elements and S isotopes of the reaction textures.

Summary: Sulfides in the CK chondrites formed through breakdown of MSS at 230°C. During thermal metamorphism, liquid S was stable in the less oxidized CKs and may have acted as a sulfurdizing agent. Core formation in the CK parent body could not occur below the silicate eutectic via melt networks due to an underabundance of sulfides caused by high fO_2 .

References: [1] McCoy T. J. et al. (2006) *Meteorites and the early solar system II*, 733-745. [2] Righter K. and Neff K. E. (2007) *Polar Sci.*, 1, 25-44. [3] Kellemeien G. W. et al. (1990) *GCA*, 55, 881-892. [4] Schrader D. L. (2016) *GCA*, 189, 359-376. [5] Lauretta D. S. et al. (1998) *Meteoritics & Planet. Sci.*, 33, 821-833. [6] Chaumard, N. and Devouard B. (2016) *Meteoritics & Planet. Sci.*, 51, 547-573. [7] Misra K. C. and Fleet M. E. (1973) *Econ. Geol.*, 68, 518-539. [8] Craig J. et al. (1968) *Carnegie I. Wash.*, 66, 440-441. [9] Kitikaze A. et al. (2016) *The Canadian Mineral.*, 54, 1175-1186. [10] McCoy T. J. et al. (2018) *LPS XLIX Abstract #2083*. [11] Kullerud G. et al. (1969) *Magmatic Ore Deposits*. [12] Naldrett A. J. (1969) *J. Petrol.*, 10, 171-201 [13] Rose L. A. and Brenan J. M. (2001) *Econ. Geol.*, 96, 145-157. [14] Gaetani G. A. and Grove T. L. (1999) *Earth and Planet. Sci. Let.*, 169, 147-163. [15] Laporte D. (1997) *Petrology and Structural Geology*, 8, 31-54. [16] Crossley et al. (2022) *Under Review*

AUTOMATING SIZE DETERMINATION OF NEAR-EARTH ASTEROIDS USING LOW SNR ARECIBO RADAR IMAGING. C. E. Champagne^{1,2}, E. G. Rivera-Valentín¹, B. Aponte-Hernández¹, P. A. Taylor³; ¹Lunar and Planetary Institute (USRA), Houston, TX 77058, ²University of Louisiana at Lafayette, Lafayette, LA 70504, ³National Radio Astronomy Observatory & Green Bank Observatory, Charlottesville, VA 24944.

Introduction: The Arecibo Observatory in Puerto Rico is one of two radar telescopes that have been used to observe near-Earth asteroids (NEAs) in order to determine their physical characteristics and astrometry [1]. Using its S-band (2380 MHz, 12.6 cm) planetary radar, Arecibo would transmit a circularly polarized signal and receive both the opposite circular (OC) and same circular (SC) polarization as transmitted. The received signal strength is a function of the transmitted power (P_t), the antenna gain (G), the system temperature (T_{sys}), the transmitted wavelength (λ), and asteroid properties, such that the signal-to-noise ratio is proportional to

$$SNR \propto \frac{P_t G^2 \lambda^2 \sigma}{R^4 k T_{sys}} \quad (1)$$

where R is the distance to the object, σ is the asteroid's radar cross section, and k is the Boltzmann constant. Thus, objects that are close and/or large have a high SNR and vice versa. These received echoes could then be used to precisely determine an object's distance and velocity. Additionally, due to the object's rotation along the line-of-sight, there is Doppler broadening of the received echoes (i.e., there is a difference in frequency between the edge moving towards Arecibo and the edge moving away), which can also be used to find the rotation period [2]. With sufficient signal, radar images (i.e., delay-Doppler images) can be made. These are 2-dimensional maps of backscatter power with delay along the vertical and Doppler along the horizontal axis.

With sufficient radar observations over multiple nights and apparitions, and observations in other wavelengths, a fully 3-dimensional shape model can be developed of the asteroid [e.g., 3, 4, 10]. However, not all objects have sufficient data to produce such shape models, and in those cases, visual inspection is used to estimate the radius of the object. This is especially true if the signal-to-noise ratio is low. While the leading edge of objects can be obvious within the image, the trailing edge can be difficult to determine. This is because as the radar incidence angle increases, the backscatter power decreases [2]. Therefore, current methods to determine an asteroid's radius from low SNR radar imaging are not consistent and well quantified. It is important to obtain an accurate estimate of the size of NEAs in the event that they are potentially hazardous. An accurate size

allows for determination of the effects of an impact and provides information for planetary defense strategies.

Here we develop, validate, and test statistical techniques to measure the size of an object in a radar image in a consistent and quantitative manner. We then apply the developed algorithm to a training data set of objects to provide new preliminary size measurements for comparison with other observations.

Method: Delay-Doppler images are in the form of z -score normalized power relative to the signal noise (i.e., in units of standard deviation above the average noise). Z -score normalization results in noise-only pixels having a mean value of zero and a standard deviation of one. To automate identification of the center of the object in delay-Doppler space, we used DBSCAN, a Density-Based Spatial Clustering of Applications with Noise algorithm. DBSCAN finds statistically significant clusters of signal within spatial-based data sets [5]. DBSCAN allows for automation of the first guess as to the location of the object and the likely location of only noise. The radar image is then collapsed along each axis to produce power spectrums, in units of standard deviation, as a function of delay and Doppler, from which our developed algorithm can identify the leading and trailing edge of the signal.

As an example, in Figure 1, we show the power spectrums of the NEA 66391 Moshup (previously 1999 KW4) in terms of standard deviation, maximum, average, and sum of the z -scores along the delay axis. Despite z -score normalization, note that Figure 1a has significant variation around a standard deviation of one. As such, using the DBSCAN-based guess of the location of only noise, the average and standard deviation of noise is taken to characterize the typical fluctuation. Our developed algorithm then determines the extent of the object by finding where the signal is greater than one standard deviation and two standard deviations above the noise-only portion of the power spectrum. In this work, we specifically employ the standard deviation of power and the maximum power as a function of delay. This is because, as seen in Figure 1, the leading and trailing edges of the asteroid are more clearly defined in the standard deviation and maximum graphs than in the mean and sum graphs. A weighted average of the two extent measurements are then taken as the estimated radius of the asteroid with the uncertainty as the weighted standard deviation of the radii.

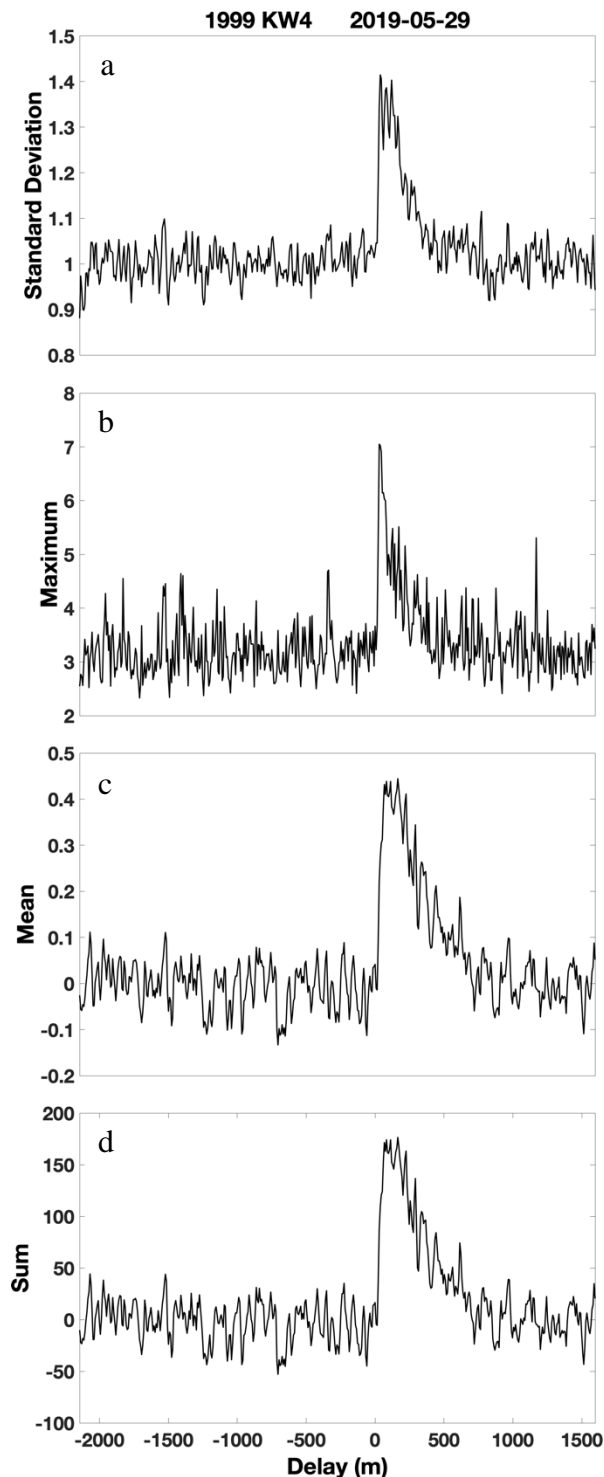


Figure 1: Echo power as a function of delay for NEA 66391 Moshup in terms of (a) standard deviation, (b) maximum, (c) mean, and (d) sum.

Validation Studies: The developed algorithm was validated using synthetic radar images and real Arecibo radar observations.

Synthetic Data: To create synthetic radar images, we began by defining shape parameters (e.g., sphere with a Bennu-like ridge) and applied standard radar-scattering parameters. We then used the SHAPE software to run the forward problem in order to produce the radar image of the chosen shape as a function of sub-radar latitude. Two shapes were tested, spherical and “diamond-like” shapes (i.e., asteroids with equatorial ridges such as Bennu). Synthetic delay-Doppler images were produced as a function of the subradar latitude ranging from 0° (i.e., where the object’s spin pole is perfectly perpendicular to the line-of-sight) and 80° (i.e., where the object’s spin pole is nearly parallel to the line-of-sight) in increments of 10° . Noise following a chi-square distribution was then randomly generated and added to the image. To study the effect of SNR, we varied the maximum signal within each image from $10\text{-}\sigma$ to $200\text{-}\sigma$ in steps of $10\text{-}\sigma$. To ensure noise statistics were adequately captured, we used Monte Carlo methods to randomly generate noise 100 times to estimate the radius and corresponding uncertainty. The average over the 100 realizations was taken as the likely radius for the considered maximum SNR.

In Figure 2, we show a plot of the ratio between the estimated radius and the actual radius of the synthetic object. In this case, the shape considered is a perfect sphere. We find that the accuracy of the developed algorithm is primarily a function of SNR. There is little variation with algorithm efficacy as a function of subradar latitude. The same is true for a “Bennu-like” shape. As can be seen in Figure 3, the primary gradient is along SNR except for very high subradar latitudes, which are rare occurrences. Generally, we find that the algorithm consistently underestimates the actual size of the object regardless of SNR, subradar latitude, and shape. This is because of the difficulty of discerning signal at high incidence angles above noise.

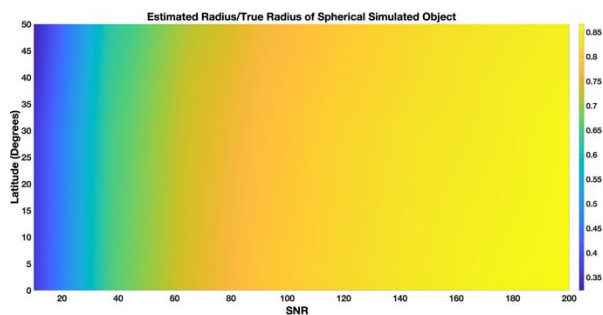


Figure 2: Plot of the ratio of estimated radius to actual radius as a function of maximum SNR and subradar latitude for a synthetically produced observation of a perfect sphere.

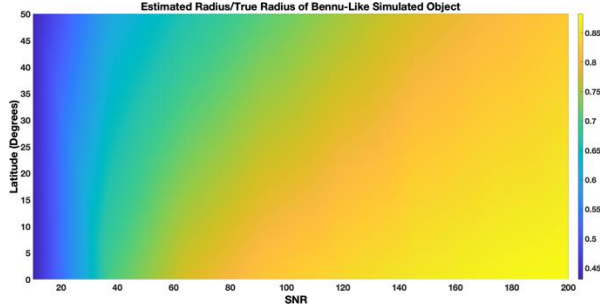


Figure 3: Plot of the ratio of estimated radius to actual radius as a function of maximum SNR and subradar latitude for a synthetically produced observation of a diamond-shaped or “Benu-like” object.

Test Objects: After the synthetic data study, we selected several spherical-like NEAs with varying maximum SNRs that have radius estimates from either the NEOWISE mission, radar-shape models, or estimates from optical observations. The NEOWISE mission, which uses a space telescope to discover and characterize asteroids, has used infrared observations to estimate the size of NEAs through thermal modeling [6]. These measurements have been shown to be well-supported by radar observations [7]. Using the observed absolute magnitude (H_{mag}) of an asteroid and making assumptions of its geometric albedo (p_v), one can also estimate the diameter as [8]:

$$D = \frac{1329}{\sqrt{p_v}} 10^{-H/5} \tag{2}$$

In Figure 4, we show the estimated radius using our newly developed algorithm for each asteroid compared to their NEOWISE, H_{mag} , or shape model based size.

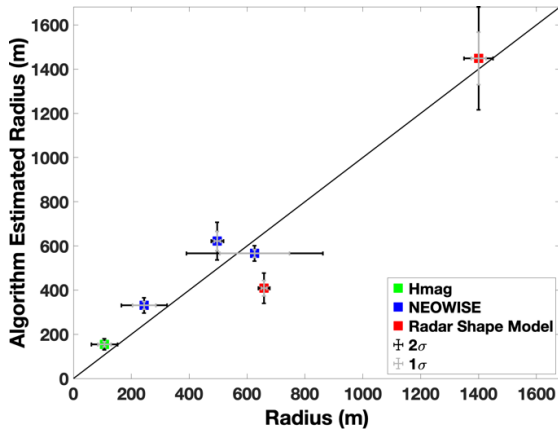


Figure 4: Algorithm-based radius estimates as a function of either estimates from H_{mag} (green), NEOWISE (blue), or radar shape model (red). The solid black line is the one-to-one correspondence.

As seen in Figure 4, generally within at least 2- σ error the algorithm-based estimates agree with other radius estimates. The only exception is 66391 Moshup, which is discussed in the next section.

Case Study: Asteroid 66391 Moshup (1999 KW4) is the only object within our test study whose size is significantly under approximated by our developed algorithm. The radar-based shape model of Moshup finds a radius of 658.5 ± 20 m [9]. However, the shape model of Moshup shows a flattened pole. This would cause the incidence angles to more sharply increase at higher latitudes, reducing the echo power. Also, Moshup has a diamond shape, and its sharp angles produces a different scattering effect than more spherical objects. This can be seen in the radar image in Figure 5.

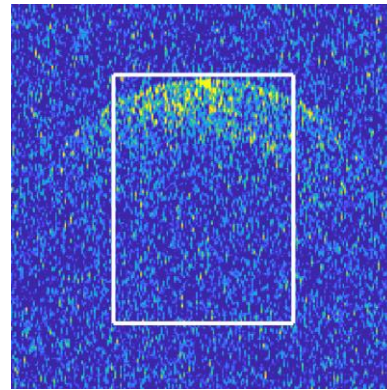


Figure 5: Delay-Doppler image of 66391 Moshup (1999 KW4). The white box is where the algorithm detected the asteroid.

Conclusions: In the field of planetary defense, it is important to know the size of near-Earth asteroids; however, current methods of determining asteroid size can require a lot of data or be inconsistent. Here, we developed an algorithm to automate size determination from low SNR radar images. Our preliminary results show the algorithm performs well for most of the test objects. In the future, we plan on expanding this to account for objects with irregular shapes, such as 66391 Moshup.

Acknowledgments: This work was partially supported by NASA through the Solar System Observations Program and made use of data from the Arecibo Observatory, which is a facility of the NSF.

References: [1] Ostro S. J. et al. (2002) *Asteroids III*, 151-168. [2] Black G. J. (2002) *ASP Conference Series*, 278. [3] Nolan M. C. et al. (2013) *Icarus*, 226, 629-640. [4] Brozović M. et al. (2018) *Icarus*, 300, 115-128. [5] Ester M. et al. (1996) *KDD-96 Proceedings*. [6] Masiero J. R. et al. (2021) *Planet. Sci. J.*, 2, 162. [7] Taylor P. A. et al. (2019) *EPSC Abstracts*, 13. [8] Harris A. W. & Harris A. W. (1997) *Icarus*, 126, 450-454. [9] Ostro S. J. et al. (2006) *Science*, 314, 1276-1280.

THERMAL EVOLUTION OF ENSTATITE CHONDRITE AND AUBRITE PARENT BODIES USING SILICATE GEOTHERMOMETRY. E. N. Etheridge^{1,2}, B. A. Anzures^{1,3}, N. Dygert⁴, C. A. Goodrich¹, F. M. McCubbin³. ¹Lunar and Planetary Institute (USRA), Houston, TX 77058, ²Marietta College, Marietta, OH 45750, ³ARES, NASA Johnson Space Center, Houston, TX 77058, ⁴Department of Earth & Planetary Sciences, University of Tennessee, Knoxville, TN. Email: eetheridge31@outlook.com

Introduction: Enstatite chondrites (ECs) and aubrites experienced a complex history of thermal metamorphism (petrologic type 3-7) as well as possible fragmentation and reassembly. ECs and aubrites, otherwise known as enstatite achondrites, are highly reduced, sulfur-rich meteorites that are primarily composed of orthopyroxene (opx). Plagioclase (plg), clinopyroxene (cpx), various sulfides, silica polymorphs, and iron metal kamacite (kam) also occur in ECs and aubrites. It has been proposed that at least 8 parent bodies are necessary to account for the current collection of enstatite chondrites [1]. Interestingly, the parent bodies of ECs seem to have experienced more severe thermal and shock metamorphism than other meteorites, however the peak temperatures and high temperature cooling rates are poorly constrained. Current equilibration temperature estimates range from 800-1000 °C for EH5 and EH6 chondrites, while EL5 and EL6 chondrites may have experienced temperatures of 600-800 °C [2,3].

To unpack the thermal evolution of enstatite chondrites, we can look at other chondrites that have experienced thermal metamorphism, especially the ordinary chondrites that have two primary hypotheses for their thermal evolution. The onion shell model describes a history in which the parent body accreted and remained largely undisturbed throughout heating. In this model, the petrologic grade is inversely correlated with cooling rate due to the internal heating and increasing pressure closer to the center of the parent body [4,5]. The competing model is the fragmentation-reassembly model where the parent body would have been disturbed through collision after some internal heating [6,7]. After re-accretion, rapid cooling would occur regardless of petrologic type. The fragments would be distributed based on size (independent of petrologic type) with rapid cooling rates based on the new distribution of the re-accreted body.

To place constraints on the thermochemical evolution of enstatite chondrite and aubrite parent bodies, we apply different geothermometers and geospeedometers sensitive to different temperature intervals, which have been recently applied to ordinary chondrites and four primitive achondrite groups [7,8,9]. These include traditional two-pyroxene (T_{BKN}) [10], REE-in-two-pyroxene [11], Mg- and REE-in-plagioclase-clinopyroxene [12,13], and silica

polymorph thermometers [3]. The most thermally metamorphosed enstatite chondrites and aubrites show a complex thermal history with some evidence of partial melting and significantly higher peak metamorphic temperatures than previously calculated. This suggests the parent bodies underwent a fragmentation-reassembly event.

Samples: We studied 7 enstatite chondrites of varying petrologic type [Allan Hills (ALH) 77296 (EH3), EET 96341 (EH4/5), MacAlpine Hills (MAC) 88136 (EL3), Miller Range (MIL) 11014 (EL5), ALH 81021 (EL6), Elephant Moraine (EET) 90102 (EL6), Hvittis (EL6), Happy Canyon (EL6/7)] as well as 3 aubrites [ALH 78113, Larkman Nunatuk (LAR) 04316,

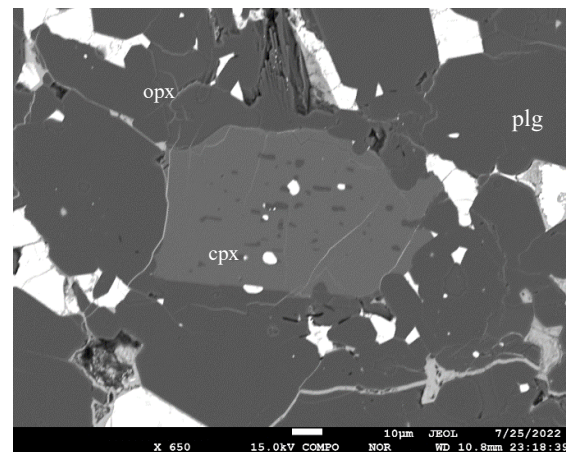


Figure 1. BSE image of EET 90102 showing paired cpx, opx, and plg grains. Melt texture visible in the cpx grain. Taken with the JEOL 8530 EPMA.

Lewis Cliff (LEW) 87020.] The samples were acquired from the NASA Meteorite Working Group (MWG) and the American Museum of Natural History (AMNH). Meteorite thick sections were mounted in epoxy and were polished down using ethanol to 1 micron diamond.

Analyses: Cpx-opx and cpx-plg pairs were identified using a petrographic microscope in reflected and cross polarized light as well as the PhenomXL Benchtop SEM in mapping mode at the Lunar and Planetary Institute. Elemental maps were produced with the JEOL 7600 SEM (15 kV and 20 nA) at NASA Johnson Space Center (JSC). Elemental maps were converted to RGB and mineralogical maps in ImageJ and XMapTools as shown in **Figure 2**. Mineral major

element compositions were acquired using the JEOL 8530 EPMA (15 kV and 25 nA) at NASA JSC. Trace element compositions including REEs and Y will be measured using the LA-ICP-MS.

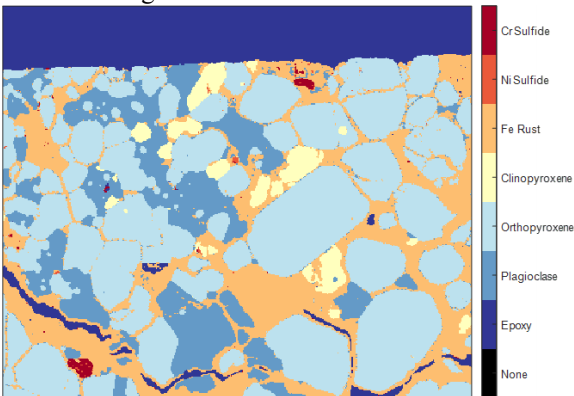


Figure 2. Mineralogic map of cpx-opx and cpx-plg grain pairs in Happy Canyon. Produced with elemental maps from the JEOL 7600 SEM and XMapTools

Mineralogy: The necessary mineral pairs were identified in two ECs (EET 90102 and Happy Canyon) and two aubrites (LAR 04316 and LEW 87020), as clinopyroxene is rare in metamorphosed enstatite chondrites. SiO₂ polymorphs were identified in these same meteorites. A mineralogical description of Hvittis is also included despite cpx not being detected yet.

Happy Canyon (EL6/7): Happy Canyon contains euhedral and subhedral grains of opx (<400µm). Plg and cpx are present in subhedral to anhedral grains (<300µm). Silica polymorph grains appear interstitially within the sample matrix (<10µm). The primary polymorph in this samples is cristobalite. Throughout the sample are recrystallized chondrules, containing much of the cpx grains present. The recrystallized chondrules are highly brecciated, primarily containing cpx with interstitial Ca-sulfide and plg-rich veins crosscutting the clasts. Sulfide phases are present interstitially. Kamacite metal (kam) veins are heavily rusted from terrestrial weathering and are present throughout the sample.

EET 90102: This sample has a similar composition to Hvittis, in that the sample is homogenous overall. The cpx, opx, plg, sulfide, kam, and silica polymorph phases are all anhedral in nature. The grains range from, 10µm to 100 µm. Melt textures are also present in cpx and opx, showing other phases exsolving from the original phase. There are large grains of kam (100µm).

LAR 04316: This sample shows a texture that is typical of aubrites. Large euhedral grains of opx (<0.5cm), cpx(<50µm), and plg(<0.5cm) are present. The opx and plg grains are larger than the cpx grains. Fracturing from shock is shown in these larger grains.

Kam and sulfides are present in anhedral grains (<10 µm). Silica glass is also present. Interesting exsolution textures are present in the larger grains.

LEW 87020: This sample has a similar texture to LAR 04316. Large, subhedral to euhedral grains of cpx, plg, and opx are present and show evidence of shock (between 50µm and 0.5 cm). Some cpx grains show exsolution lamellae, exsolving to opx. The cpx grains are significantly larger in this sample than in LAR 040136. Sulfide and metal phases occur both as anhedral grains and interstitially between larger grains (50µm). Silica polymorphs were identified and occur interstitially. The polymorph in this sample is likely tridymite.

Hvittis: The overall matrix of Hvittis shows a similar texture to EET 90102. There are also large recrystallized chondrules within the sample showing a different texture (approximately 0.5 cm). Within the largest chondrule, there are laths of opx and plg. There are other recrystallized chondrules showing a less obvious recrystallization texture, radially crystallizing with plg, opx, sulfide, metal, and silica polymorphs (chondrule <200 µm, other grains <100 µm). The silica polymorph in this sample has not yet been identified. Cpx has not been definitively identified in this sample.

Temperatures: Geothermometers use the diffusivity of coupled elements to show what the peak metamorphic temperature the mineral pair experienced. REE thermometers are more sensitive to higher temperatures. The diffusivity of these elements is slower that of major elements, allowing for more sensitivity at higher temperatures. Applying REE and major element thermometers can clarify the thermal history ECs and aubrites experienced. When compared with major element data, temperatures produced by REE thermometry are higher for continuous cooling without variation, while the temperatures values will be similar if quenching occurred. If the major element values are larger, then an event that disturbed the heating/cooling process and created inaccuracies in the calculations [11].

Two-pyroxene: The values calculated for the opx-cpx pairs examined in each sample using the two-pyroxene thermometer developed by Brey & Köhler (T_{BKN}) [10] are reported in the Table 1. The aubrites show some differences in temperature using this thermometer due to the brecciated nature of this group. The ECs are more consistent. Both have higher temperature than have been previously reported for aubrites and ECs. This suggest that the pyroxene phases experienced high temperature metamorphism but remained in that phase before cooling. The REE-in-two-pyx will tell if the pyroxene mineral pairs reached higher peak metamorphic temperatures as the REE

calculators are more sensitive to high temperatures than the major element calculators.

Mg-in-cpx-plg: The values calculated for the cpx-plg pairs identified in the samples using the Mg in cpx-plg thermometer developed by Sun and Liang (T_{Mg}) [12] are reported in the Table. Overall, the T_{Mg} temperatures only agree with LAR 04136. The other meteorites have $T_{Mg} > T_{BKN}$. This is consistent with plg forming from partial melting at a higher temperature (due to shock/impact melting) while the opx could be preserved from before metamorphism. The textures within each meteorite must be examined to provided further clarity on this matter.

Table 1. Closure temperatures ($^{\circ}C$) for EC and aubrite samples using the two-pyx and Mg in cpx-plg thermometers. Uncertainties given by 1σ standard deviations.

Sample	T_{BKN}	T_{Mg}	T_{SiO_2}
Aubrites			
LAR04136	1010 \pm 63	1012 \pm 3	Silica Glass
LEW87020	1090 \pm 30		Tridymite
Enstatite Chondrites			
EET90102 (EL6)	892 \pm 23	1035 \pm 40	Quartz
Happy Canyon (EL6/7)	975 \pm 2	1259 \pm 11	Cristobalite

Discussion: Geothermometric techniques such as the silica polymorph thermometers developed by Kimura (2010) and opaque phase thermometry as used by Zhang (1996) have been applied to enstatite chondrites previously [2,3]. Comparing the geothermometry results found in these studies using different silicate mineral pairs helps reconstruct the multiple-stage thermal history of the parent bodies of these meteorite groups.

Silica polymorph thermometer: Kimura suggests that for type EL6/7, they experienced high temperature metamorphism and partial melting to form the cristobalite and tridymite present [3]. Tridymite is stable above 867 $^{\circ}C$ and cristobalite is stable above 1470 $^{\circ}C$, reflecting the high temperature processes these components must have experienced. This explanation agrees with the temperatures produced by the Mg in cpx-plg calculator if partial melting has occurred for plg and to produce the silica polymorphs. Cristobalite and tridymite has been identified in these samples as listed in the Table 1.

Alternate geothermometry: Zhang uses opaque phase thermometry for enstatite chondrites, using FeS in (Mg,Mn)S, FeS in ZnS, Fe-Ni-P, (Mg,Mn)S in CaS,

and KQEOT (kamacite, quartz, enstatite, oldhamite, and troilite) [2]. The KQEOT thermometer reports similar peak metamorphic temperatures to the T_{Mg} values from this study. This thermometer has been the most widely used on enstatite chondrites [2].

Cooling rate and implications: While the REE data has not yet been measured for the samples in this study, Floss et al. has REE data on EET 90102 [14]. Using this data and the REE-in-two-pyroxene thermometer, T_{REE} appears to fall into the to 1100 $^{\circ}C$ range. $T_{REE} \gg T_{BKN}$ indicates a slower cooling rate. For EET 90102, the cooling rate is ~ 3 C/yr. Comparing this value to the T_{REE} values for ordinary chondrites (OC) calculated in the Lucas et. al (2020) paper, this value is continues to be higher than other calculated groups using this method [7]. The cooling rate found for OC varies with the subgroup within the OC chondrite group. The H chondrites group has an estimated cooling rate of ≥ 10 $^{\circ}C$ from T_0 of ~ 825 $^{\circ}C$. L chondrites have a cooling rate of ~ 0.5 to ~ 10 $^{\circ}C$ /year from T_0 of ~ 900 to ~ 1000 $^{\circ}C$. LL chondrites have a more complex cooling history, but is still estimated to have a colling rate of ~ 1 to ~ 100 $^{\circ}C$ /yr. The cooling rate of the OC group overall is more rapid than the preliminary calculation of the EC and aubrite cooling rate. Less rapid cooling suggests that enstatite chondrites and aubrites experienced a more coherent history.

Further work to constrain the REE values for each sample with the necessary pairs will provide clarity on the thermal history, allowing for the calculation of the cooling rates. If this trend from the literature values continues, that suggest that quenching did not occur, and the parent bodies had a more continuous cooling history. Using silica polymorph geothermometry will also provide further clarity on the cooling history of enstatite chondrites and aubrites.

References: [1] Weyrauch et al. (2018) *MPS*, 53, 394-415. [2] Zhang (1996) *MPS*, 31, 647-655. [3] Kimura (2010) *MPS*, 6, 855-868. [4] Miyamoto (1981) *Proc. LPSC*, 1145-1152. [5] McSween et al. (2002) *Uni. AZ. Press*, 559-571. [6] Grimm (1985) *J. Geo. Rea*, 90, #2022. [7] Lucas et al. (2020) *GCA* 290, 366-390. [8] Lucas et al. (2019) *LPSC XLIXI*, Abstr. #2495. [9] Anzures et al. 2022 *LPSC XLIXIV*, Abstr. #2696. [10] Brey & Köhler (1990) *J. Pet.* 31, 1353-1378. [11] Liang et al. (2012) *GCA* 102, 246-260. [12] Sun & Liang (2017) *Contr. Min. Pet.* 172, 1-20. [13] Sun & Lissen-berg (2018) *EPSL* 487, 165-178. [14] Floss et al. (2003), *GCA*, 67, 543-555.

ANALYSES OF CURIOSITY'S GROUND TEMPERATURE MEASUREMENTS: CORRECTION FOR THERMAL NOISE. J. A. Gambrill^{1,2} and G. M. Martínez¹, ¹Lunar and Planetary Institute, Houston, TX, USA, ²Embry-Riddle Aeronautical University, Daytona Beach, FL, USA.

Introduction: The Mars Science Laboratory (MSL) Curiosity rover has been studying the Martian climate within the 154 km wide Gale crater for a decade. On board Curiosity, the Rover Environmental Monitoring Station (REMS) collects meteorological data from the surrounding environment [1]. REMS includes a Ground Temperature Sensor (GTS) to determine the temperature on the Martian surface [2]. The GTS is the first ground-based instrument on Mars capable of continuously assessing the surface temperature [3], shedding light on surface-atmosphere H₂O exchanges, and thus on the water cycle, habitability, and In Situ Resource Utilization of Mars [4]. These measurements also provide ground-truth to orbital measurements [5].

Fig. 1 shows 1 Hz temperature measurements (blue) taken by GTS as a function of Local Mean Solar Time (LMST) on sol 531 (Ls ~ 84°). The average temperature over the first five minutes of each hour is represented by the red dots. At 03:00 LMST, there is a decrease in temperature immediately followed by an increase at 04:00. This decrease is > 5 K, while the uncertainty at night is around only 2 K indicating that the measured temperature is an outlier [3]. This behavior is also found on other sols.

These outliers and the key sources of noise contributing to the systemic error within Curiosity's ground temperature measurements is the point of investigation. Identification and removal of erroneous measurements will contribute to a more accurate set of temperature measurements.

Data: REMS uses a 1 Hz sampling rate. The primary interval of sampling, called a nominal block, recurrently takes measurements for the first five minutes of every hour. The second approach samples in extended blocks, consisting of one or more consecutive hours followed by five additional minutes in the subsequent hour.

The 1 Hz data from these sampling intervals are available in NASA's Planetary Data System (PDS). Data downloaded from the PDS included ground temperature for all available sols as well as thermopile and ASIC temperature for Martian Year (MY) 32, the first full MY in which Curiosity was on Mars. The thermopile converts thermal energy into an electrical signal to be read by MSL. The ASIC provides and regulates the power supplied to the GTS. Since both components are part of the ground temperature system, their temperatures may affect its performance.

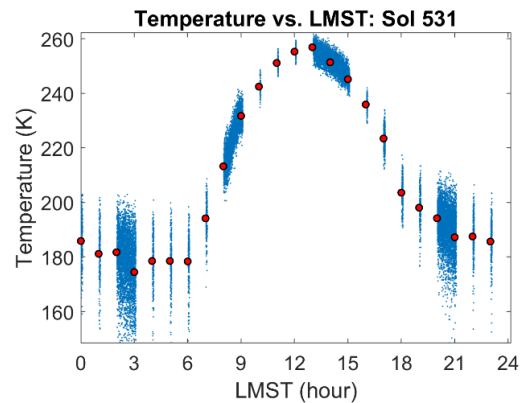


Figure 1. Five-minute averages at the beginning of each hour (red) superimposed over 1 Hz GTS data (blue). Some 1 Hz measurements were excluded from the figure as they fell below the X-axis, but were included in calculating the averages.

Methods: All data from the first five minutes of each hour were averaged for the ground, thermopile, and ASIC temperatures. Additionally, the data from those five minutes were plotted as 20-second moving averages. The five-minute moving averages were catalogued into three groups: one containing all the averages, another comprising of nominal blocks and the first five minutes of extended blocks, and the last one with the averages one midway through or at the end of extended blocks. A third order line of best fit was superimposed over the moving averages. The trendlines for each hour in every sol were categorized according to the type of function the moving average makes. Each type of function was categorized according to its shape, except for linear constant functions, which are classified as any function shape so long as the trendline's amplitude does not exceed 1.5 K. Examples of the functions are shown in Fig. 2. These functions were then classified in pie charts (Fig. 3). The amplitude, i.e., the difference between the maximum and minimum temperature, of each trendline was plotted in a bar chart in Fig. 4. Figs. 2, 3 and 4 are analyzed in the Results section below.

Furthermore, the types of functions were assessed to determine whether any had a statistically significant deviation as compared to the other functions. This was accomplished by finding the average temperature of two of the functions for each hour for consecutive sols in which MSL was stationary. The difference between the average temperature and the temperature for each sol of one of these functions in the group was obtained. The differences were averaged for each type of

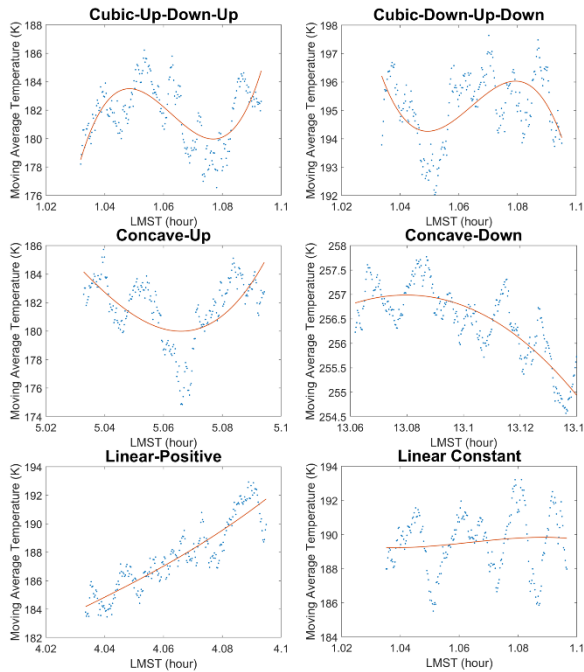


Figure 2. Moving averages (blue) for the first five minutes of each hour. The line of best fit (red) is plotted over the moving average. Each graph represents one of the seven different types of function. Negative linear (not shown) has a constantly decreasing line of best fit.

function, which were used to determine if any function had consistently larger errors than the others (Fig. 5).

Results: Comparing hours in the extended block category with the average at the same time for nearby sols reveals that unexpected decreases in temperature correspond to averages taken after the GTS has been running for extended durations. As an example, there was an extended block from 02:02 to 03:06 LMST on sol 531 (Fig. 1), resulting in a significantly lower temperature than anticipated for the 03:00 average.

Although there are changes in pattern due to extended blocks as well as Ls and LMST, no type of function resulted in a greater quantity of outliers. This difference is augmented by the local temperature. As can be seen in Fig. 3, linear constant functions are more common in the warmer times of the year, particularly at Ls 180°-270°, than the colder part of the year from Ls 45°-135°. Linear constants are also more prevalent during the warmer hours of the day than at night, constituting as much as 95% of all the functions at 12:00 LMST for a particular section of Ls. Fewer linear constant functions during cold periods indicate a larger short-term variation in temperature which leads to a greater uncertainty. Fig. 4 also shows this with the average amplitude of the types of functions over a certain period. The bar charts reveal a much greater variability for each type of function at colder

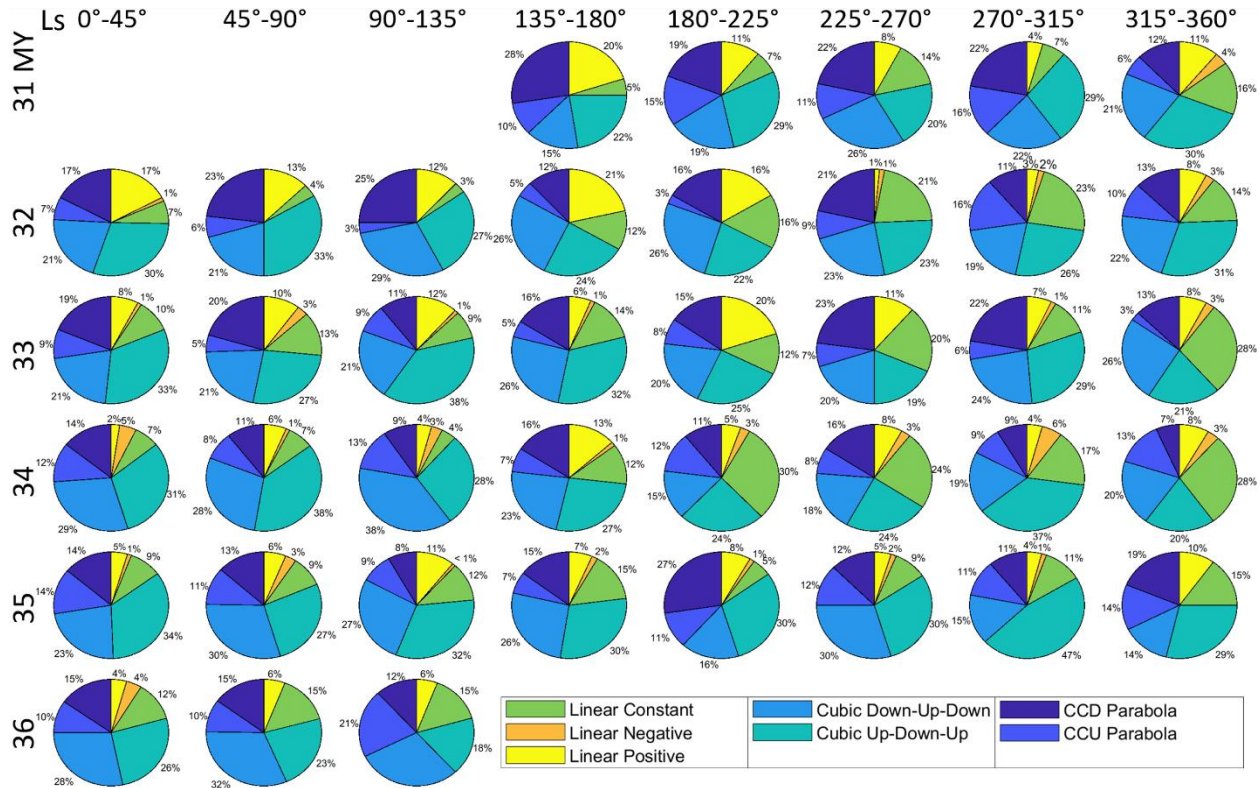


Figure 3. Pie charts represent the distribution of types of functions at 06:00 LMST as a function of Ls and MY.

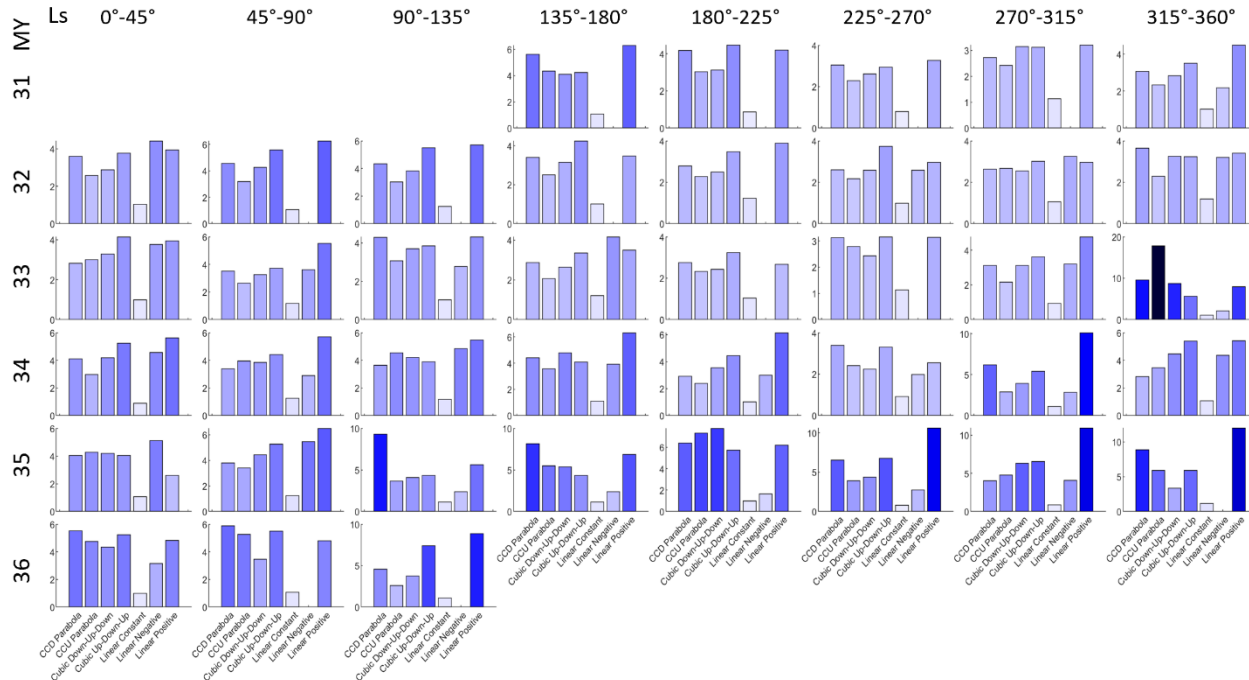


Figure 4. Bar charts represent average amplitude of the trendline for each type of functions defined in Fig. 2. Depiction only accounts for measurements at Ls 06:00 for all LMST and MY.

temperatures. While there is greater variability, no type of function consistently has greater amplitude than another other than when compared to linear constants. This is because linear constants are categorized by their amplitude rather than the shape produced by fitting a trendline. Additionally, the variations in temperature increase each MY, with the average amplitude doubling from MY 32 to MY 36.

Subsequent analysis of the thermopile and ASIC suggest no correlation between their operating temperatures and the measured ground temperature. This can be extrapolated by analyzing the same time over consecutive sols in which the rover is stationary.

By remaining in the same location, the daily temperature over a limited number of sols is expected to be similar. Consecutive sols in which the thermopile and ASIC temperatures and their fluctuations were nearly identical could lead to ground temperature differences of a few degrees K, indicating no causality in the decrease of measured ground temperature.

By comparing the temperature deviation of types of figures in heat maps such as Fig. 5, there is no function that significantly deviates from the average temperature more than another.

Conclusions: Extended blocks lead to a greater divergence from the average temperature calculated from the temperature of surrounding sols at the same LMST. This issue is accentuated at colder temperatures, but still present during warmer periods. The type of function the moving average makes, the thermopile temperature, and the ASIC temperature analysis yielded no correlation with decreases in ground temperature or extended blocks. Additional reasons for this will be investigated as future work. Because the underlying issue remained unidentified, all measurements taken after the first five minutes of an extended block should not be considered.

References: [1] Grotzinger, J.P., et al. (2012) *Spa Sci Rev* 170, 5–56. [2] Gómez-Elvira, J., et al. (2012) *Spa Sci Rev* 170, 583–640. [3] Martínez, G.M et al. (2017) *Spa Sci Rev* 212, 295–338. [4] Martínez, G.M., et al. (2016) *Icarus* 280, 93-102. [5] A.R. Vasavada, et al. (2017) *Icarus* 212, 295–338.

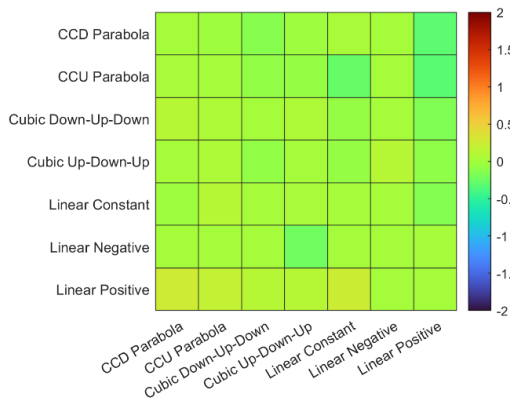


Figure 5. Heat map of differences between the average of different functions at 06:00 LMST. No significant variation between the various functions were found.

INVESTIGATING SOURCE-TO-SINK PROCESSES ON EARTH TO CONNECT TO MARS. F. D. Garcia Ledezma^{1,2}, C. C. Bedford², V. Tu⁴, E. Rampe³, M. Thorpe³, ¹Department of Geological Sciences, University of Texas at El Paso ²Lunar and Planetary Institute, USRA, Houston, USA ³NASA Johnson Space Center, Houston, TX 77058, ⁴Jacobs JETS at NASA Johnson Space Center, Houston, TX 77058

Introduction: NASA's *Curiosity* rover landed in Gale crater in August 2012 to investigate the habitability of Mars through time [1]. As such, *Curiosity* is equipped with multiple science cameras, including the Mars Hand Lens Imager (MAHLI) and several geochemical and mineralogical instruments to assist with the interpretation of the geological history [1]. The MAHLI camera takes close-up images of rocks and soils on Mars to provide context imaging of the soils and sedimentary rocks for the geochemical and mineralogical instruments [1].

The ancient (>3 Ga) sedimentary rocks in Gale crater have formed by fluvial and lacustrine processes, with aeolian processes dominating the geological record of Gale crater after the river-lake system ended in the Hesperian [2,3]. The fluviolacustrine sedimentary system that existed in the past in Gale crater was likely habitable for life as we know it on the Earth, however, the mineralogy is dominated by basaltic materials, not the quartzofeldspathic minerals that derive most sedimentary rocks on the Earth [4]. There remains a knowledge gap for understanding how basaltic materials are physically and chemically weathered in Fluvial and Aeolian environments.

This research aims to understand how the physical and chemical characteristics of basaltic sediments change as they are transported from source to sink in Mars-analog environments. To fulfill this research aim, close-up images of Mars-relevant basalt-dominated sedimentary systems in Iceland have been analyzed using ImageJ and using XRD from source-to-sink.

The SAND-E Mission: The Semi-Autonomous Navigation of Detrital Environments (SAND-E) seeks to examine the chemical and physical alteration of sediments from source to sink in Aeolian-Fluvial sedimentary systems like those found on Mars [5].

Iceland's cold and wet climate, predominately basaltic crust, and presence of active fluviolacustrine and aeolian sedimentary systems make it a popular Mars analog [6]. For this reason, the Þórisjökull glacio-fluvio-aeolian sedimentary system was selected for the 2019 SAND-E Mission Field Area to study source-to-sink processes in these environments. The field sites were located between 4 tholeiitic volcanoes and samples were gathered from sites near the source, mid-way to the source and far away from the source (Fig. 1).

Methods: The sedimentary environment (fluvial or aeolian) for each MAHLI-analog target was identified using the SAND-E rover's Mastcam images. Close-up

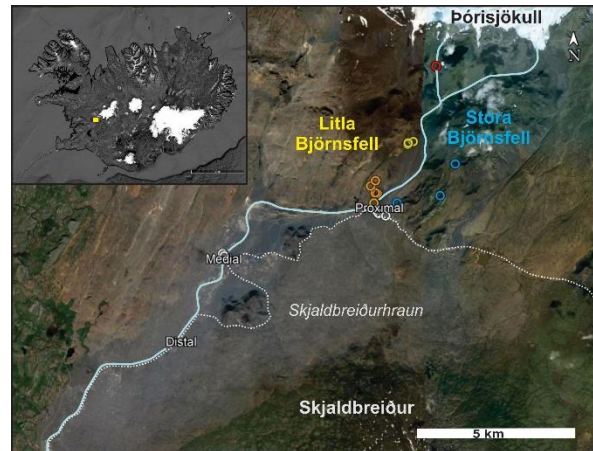
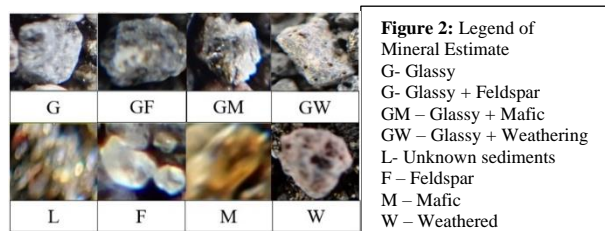


Figure 1. SAND-E 2019 Field Map: Blue line represents the Þórisjökull glacio-fluvio-aeolian sedimentary system. Yellow square in top image demonstrates SAND-Es 2019 Field Site. These sites are represented in Figure 1 with the color-coded circles for each volcano that was sampled. The blue line demonstrates the Þórisjökull glacio-fluvio-aeolian sedimentary system from which the samples were taken. Picture Credit: Bedford et al., (in prep.).

images of basaltic source rocks were taken from the Proximal, Medial and Distal sites using the Olympus Tough TG-6 camera. The close-up images were taken in microscope mode at zero stand-off during the 2019 SAND-E Mission to simulate images taken with the MAHLI camera on *Curiosity*. Changes in sample mineralogy were determined qualitatively by carefully classifying grain textures.



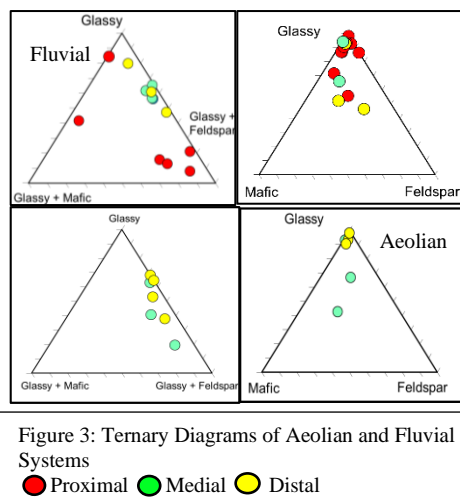
Mineralogical estimates were classified with the letters G for glassy, F for Feldspar, M for mafic, W for weathered, L for variety and N/A for points with no data (Fig. 2). Combinations of letter were also used to denote the appearance of two of these characteristics on the same grain. To quantify mineralogical and physical changes across the Proximal, Medial, and Distal field site, the Gazzi Dickinson method was performed using ImageJ to determine the mineralogical estimate of the samples. A grid of 300 points was generated for each MAHLI-analog image and the grain classifications determined from the qualitative analysis were used to characterize the grains at each point in the grid. This

software was also used to measure the intermediate and long axis of the grains and note when a grain contained vesicles.

Results: Fluvial deposits: Sediments deposited by fluvial processes are present in all three sites. Fluvial sediments contain a wide variety of grain sizes ranging from 2.4 mm to 1.7 mm. As cobbles were too large and often encompassed the entire MAHLI-analog image they have been excluded from this analysis. The silt grain size was also excluded for the opposite reason in that silt grains were too small to clearly distinguish in the MAHLI-analog ImageJ analysis.

Fluvial sediments had average intermediate grain sizes of 2.4 mm (granule) at the Proximal site, 1.2 mm (coarse sand) at the Medial site, and 0.8 mm (coarse sand) at the Distal site. The long axis average of each site respectively is 3.9 mm (granule), 1.7 mm (coarse sand), 1.0 mm (coarse sand) which shows that grain size decreases down the system.

Roundness of a grain can help us understand the physical change a sediment experienced and is defined by dividing the intermediate and long-axis of the grains. The closer the answer is to 1, the rounder the grain is. Proximal site sediments outcomes averaged to 0.77. Medial site averaged to 0.71, while Distal site averaged to 0.82. These averages illustrate the shape of the grains as semi-rounded to rounded and showed an increase in roundedness from the Proximal site to the Distal site.



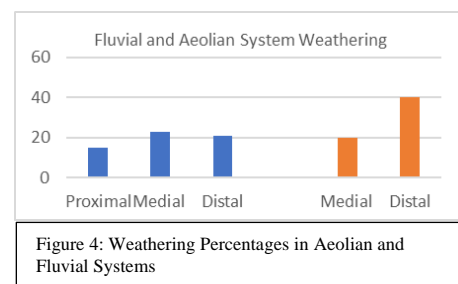
Proximal site images demonstrated a significant abundance of glassy grains making up on average 75% of the sediments, with 53% of grains exhibiting glassy with feldspar and 47% glassy without phenocrysts (Fig. 3). Medial site sediments show a similar pattern with 60% glassy grains; however, compared to Proximal, 84% of the grains are just glassy. Distal site sediments cluster around the glassy side, with 90% the grains being glassy.

Weathering was used as an indicator of chemical alteration and identified based on the appearance of an orange/brown surface. In the fluvial system the appearance of weathered surfaces increases from the Proximal 15% to Distal sites 21%, as seen in Figure 4. Vesicle abundance also varied across the Proximal, Medial, and Distal sites. The Proximal site grains did not contain as many vesicular grains compared to the Distal site. Proximal site vesicularity was only present in 31% of the grains, while in the Distal site it made up 42%. Vesicles also often contained weathered materials. This characteristic was mostly found in the Distal site, but also seen in smaller amounts around the Medial and Proximal sites.

Aeolian deposits: Aeolian deposits are only sampled at the Medial and Distal sites. Most of aeolian sediments are vesicular and semi-rounded to rounded. Single-mineral grains are also more prominent in this system. The colors of these minerals tend to range from white to green. Aeolian sand intermediate grain size averages in the Medial and Distal sites are 0.7 mm (coarse sand) and 0.6 mm (coarse sand). Long axis average of each site is 1.0 mm (coarse sand) and 0.7 mm (coarse sand). Dividing these lengths by each other show an average roundness coefficient of 0.7. This number means that the grains are semi-well rounded.

Mineral abundance in aeolian deposits differ to those in fluvial deposits. Though glassy grains make up a significant amount (average of 83%) of the image's mineral abundance, single-mineral grains are more abundant than in the Fluvial sites. Medial site grains demonstrate a higher percentage of mafic minerals (19%) in comparison to felsic minerals (13%) (Figure 3). This pattern continues through the Distal site, with percentages of 1.4% compared to 0.9%. (Figure 3).

Weathering in aeolian sediments increased with respect to distance as well. Percentages of weathered surfaces doubled from the Medial (19%) to the Distal (40%) (Figure 4). Comparing the two systems, the Proximal and Medial site share a similar percentage of 20%. The aeolian Distal sediments, however, have double the abundance of weathered surfaces compared to the fluvial Distal sediments.



Vesicularity in aeolian systems also occurs in higher percentages than in its fluvial counterpart. In this sedimentary environment, on average 45% of the grains had vesicles. Separating them to their respective locations, 29 % of the Medial-site grains contained vesicles, while in the Distal-site 77% of the grains had them. Vesicular weathering was also present in aeolian samples. The same pattern of Distal vesicular weathering occurred with respect to this sedimentary process.

Discussion: Through using up-close MAHLI-styled images of sediments found at different distances from the source, we have distinguished the chemical and physical impact of aeolian and fluvial systems on grains. Information gathered by measuring intermediate and long axis was used to model shape and size of the sediments. To track mineralogical estimates, the Gazzi Dickenson method and XRD analysis were performed.

Fluvial sediments were rounder than those found in aeolian deposits. Fluvial sediments also showed an increase in roundness with respect to distances, whereas aeolian grains remain relatively the same. The roundness coefficients were also higher in the fluvial system demonstrating well-rounded sediments. Suggesting that fluvial transportation tends to round rocks better due to the constant grain abrasion occurring from source to sink in a denser transport medium. Aeolian abrasion also occurs in small scale levels as the grains hit another surface or grain [7].

In both systems the size of the grains decreased the further away from the source. While the size of the Fluvial site sediments decreases at a constant level, aeolian grain sizes do not differ much from the Medial to Distal site. This pattern can be attributed to aeolian transportation usually carrying grains already small enough to be carried while fluvial transportation actively erodes the sediments. Vesicles also appeared to play a role in the transportation of sediments. Higher amounts of vesicularity occurred at the Distal sites in both Aeolian and Fluvial systems. One interpretation of this could be that the more vesicles around a grain, the lighter it is to transport further away from its source. This makes sense considering that Distal grains in aeolian systems had higher vesicular abundances that could have aided the transportation of the sediments considering their size.

Minerals in sedimentary systems tend to react differently to weathering processes and are sorted during transportation depending on their shape, size, and density [8]. Large abundances of volcanic glass appear in all three sites, as well as in both systems. This high percentage can be attributed to their resilient nature which makes it harder to breakdown and erode [8]. Fluvial system mineralogy is more diverse at the

Proximal site in the glassy grains but has a higher abundance of individual mineral grains towards the Distal site. This suggests that individual phenocrysts are being physically weathered out of the glass grains with transportation from the source.

Aeolian system mineralogy also leaned more towards glassy but tended to be enriched in single-mineral grains. Mafic mineral enrichment occurred particularly in the Medial aeolian sediments. This occurs thanks to olivine's ability to travel farther distances due to its small size and roundness which makes it perfect for wind transportation [9]. The decrease in single grain mafic minerals in the Distal sites can be attributed to olivine's lack of durability due to its crystal structure and density [8]. Because of this, and their smaller size, mafic minerals and glass are often found in aeolian deposits on Earth and Mars [9].

Weathering of sediments was also prominent in the aeolian system rather than in the fluvial. Grain abrasion could be responsible for the smaller quantity of weathering in the fluvial system. Constant grain movements could have played a role by removing the weathered coating around the sediments in an active environment. The presence of weathering in a grain can also be useful determining ages as weathered grains are likely to have been immobile for longer periods of time.

Mars Implications: Mar's geologic records demonstrate the presence of both fluvial and aeolian systems. Understanding these two features is crucial to piece together the history of the red planet. This can be done through Mars-analog research in environments that mimic the systems being researched. With the use of the Gazzi Dickenson method, grain size, shape and mineralogical estimates were gathered to observe the physical and chemical grain alterations that occurred through these sedimentary systems. Having created this analog data, we can then compare the information to Mar's images by using this same method on MAHLI images taken by *Curiosity*. We can then make interpretations on the similarities they share and correlate them to what is present on Earth to figure out past Martian environments.

References: [1] Grotzinger J.P et al., (2012) *Space Sci Rev* 170, 5-56. [2] Grotzinger J.P et al., (2015) *Science* 350, 167. [3] Edgar L. A. et al., (2020) *Journal of Geophysical Research: Planets* 125, 12. [4] Bandfield J. L. et al (2004) *Journal of Geophysical Research: Planets* 109. [5] Ewing R. C et al (2019) LPSC L, Abstract #1485. [6] Thorpe et al (2021) *Journal of Geophysical Research* 126. [7] Greeley R. et al (2001) *Space Science Reviews* 96, 393-404. [8] Cornwall C. et al (2015) *Icarus* 256, 13-21. [9] Mangold N. (2011) *Earth and Planetary Letters* 310, 233-243.

PROPERTIES AND COMPARATIVE ANALYSIS OF VENUSIAN RIFT ZONES. T. E. McKenna^{1,2} and M. B. Weller¹, W. S. Kiefer¹, ¹Lunar and Planetary Institute (USRA), Houston, TX 77058, ²Department of Astronomy, Cornell University, 616 Thurston Ave, Ithaca, NY 14853 (tem76@cornell.edu).

Introduction: Venus' thick atmosphere has historically made it difficult to determine geologic surface features and interior dynamics of Venus [1]. Venus has a surface pressure of approximately 93 bars, or about 9 times that of Earth's, high surface temperatures of around 737 K, and perpetual clouds [1]. These conditions make it extremely difficult for lander and in situ missions. Radar, however, penetrates the thick atmosphere and omnipresent clouds to observe the surface. The Magellan mission in 1989 returned global coverage of radar data that has formed the basis of our knowledge of surface features such as volcanic rises and rifting on Venus [2].

There are several prominent topographic rises on the surface of Venus, which are associated with volcanic centers, including Beta, Western Eistla, and Atla Regiones. These are thought to be the result of hot upwelling mantle plumes [3]. Plumes which originate in the mantle, ascend toward the surface, creating uplift and deformation of the lithosphere, including rifting. Devana Chasma is a rift associated with the Beta Regio volcanic rise, and Ganis Chasma (Figure 1a) along with the volcano Ozza Mons are associated with Atla Regio. Some rift zones on Earth show similar behavior to these features on Venus and may be somewhat analogous, such as the Rio Grande rift in the southwestern U.S. and the East African Rift System (EARS). There is substantial evidence through seismic studies that the EARS is supported by a mantle plume [4].

In most cases, the lithosphere flexural response to the upwelling mantle plume can be approximated as a line load distributed underneath the lithosphere [5]. The resulting flexural response can be modeled to constrain the elastic lithosphere thickness, obtain information about dynamic support, and determine the rate of heat flow as it varies with distance from the plume.

In characterizing the rift in the context of a mantle plume, we determine flank heights and rift depths as a function of distance along the rift. We also model the flexural response of the lithosphere at Ganis Chasma in order to determine elastic lithosphere thicknesses. From this, we can gain insight into the dynamics of Venus's interior: past and present.

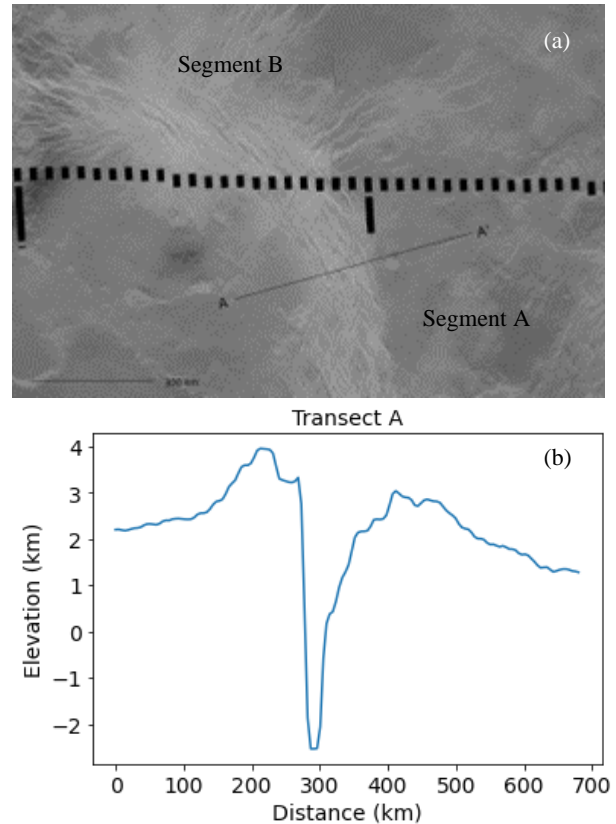


Figure 1. (a) Magellan Synthetic Aperture Radar (SAR) of resolution 110 m/pixel of a subset of Ganis Chasma [2]. Transect A is marked, profile was taken from A to A'. (b) Topographic profile of Transect A using Magellan Altimetry data of resolution 10 km/pixel [2].

Rift Flank Heights: For our analysis we considered Ganis Chasma as three distinct segments, based on rift orientation. The first segment (A) trends generally northward from its initiation near Atla Regio (e.g., Figure 1a). The second segment (B) is delineated from the general North-South orientation of A by shift to a predominately westerly orientation. The final segment (C) returns to a general North-South orientation and terminates towards the regional plains. The lengths of the segments are approximately 865 km, 832 km, and 895 km for segments A, B, and C, respectively. To obtain along strike variations of key quantities, such as rift flank elevations, we took 1200 km profiles using Magellan altimetry data spaced at approximately 25 km intervals along each rift section,

and oriented perpendicular to the rift. An example profile is illustrated in Figure 1b. We generated 106 profiles in total systematically sampling the approximately 2,500 km rift. Figure 2a and 2b show the flank elevation (referenced to the Venus mean planetary radius) for both the West and East flanks. Here West and East are taken as the western and eastern flank profile as defined in rift Segment A, and continues through Segments B and C.

In Segment A of the rift, nearest to the volcanic rise of Alta Regio, the western flank heights are systematically at higher elevations than the eastern flanks, with an average elevation of 3.77 km and standard deviation of 1.03 km for the western flank, and 3.23 km and standard deviation of 0.342 km for the eastern flank. Moving along the rift in Segment B, elevations between the western and eastern flanks transition to eastern dominated, with mean elevations of 3.30 and 3.94 km, with a standard deviation of 0.322 and 0.5473 km, for the western and eastern flanks, respectively. Along the final portion of the rift, Segment C, Eastern flank heights dominate over western flank heights, with average eastern heights of 3.62 km (0.974 km standard deviation), and an average western height of 3.43 km (0.429 km standard deviation). In total, the average western flank elevation for Ganis Chasma is 3.52 km, and 3.57 km for the eastern flank.

Our flank height results compare with that of Devana Chasma, where the rift flank heights span 1-3 km [9].

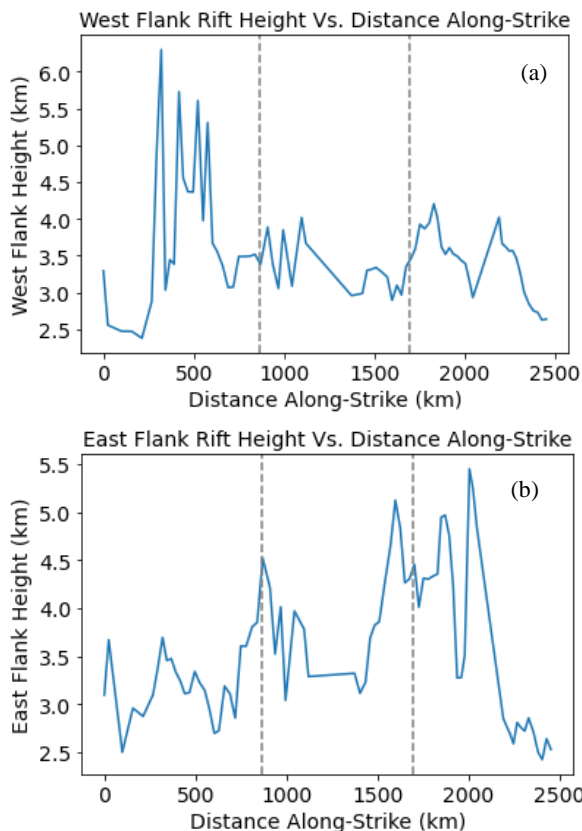


Figure 2. (a) West rift flank height a function of distance along the rift. (b) East rift flank height a function of distance along the rift. The dashed lines on (a) and (b) represent the boundaries between Segments A, B, and C.

Rift Flank Widths: The width of the rift is defined as the distance between the points of maximum elevations on the west and east rift flanks. Determination of the flank elevations allows for the quantification of the along strike rift width (Figure 3). Maximal widths occur roughly corresponding to maximal flank elevations shown in Figure 2a and b. For segment A, the average width is 211.9 km, and 223.2 km for segment C. Minimal widths occurs in the middle portion of the rift, Segment B (142.5 km).

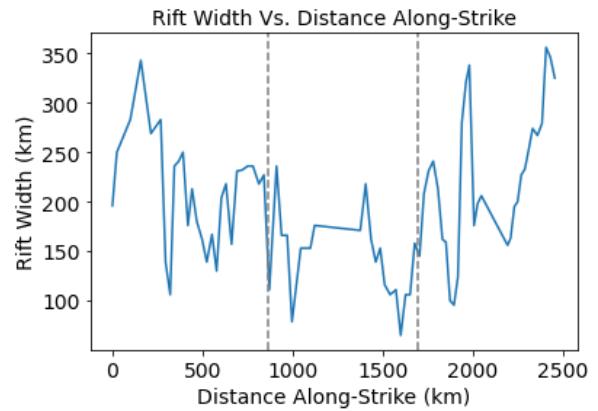


Figure 3. Rift width measure from West to East flank as a function of distance along the rift. The dashed lines represent the boundaries between Segments A, B, and C.

Flexure Modeling: The flexure profiles were modelled based on the line load approximation [5]:

$$w = d_1 e^{-x/\alpha} \cos\left(\frac{x}{\alpha}\right) + d_2 e^{-x/\alpha} \sin\left(\frac{x}{\alpha}\right) + d_3 x + d_4 \quad (1)$$

which describes the flexural response of the lithosphere due to a load. In this equation, w is the flexural topography induced by the lithospheric load, d_1 and d_2 . For Ganis Chasma, this load is due to normal faulting which creates a central valley which in turn leads to a flexural uplift of the flanks (which can be seen in Figure 1a). d_3 is the regional slope, and d_4 is the topographic regional mean elevation. The flexural parameter (α):

$$\alpha = \left(\frac{4D}{\rho g}\right)^{1/4} \quad (2)$$

which depends on the flexural rigidity of the lithosphere (D):

$$D = \frac{ET_e^3}{12(1-\nu)} \quad (3)$$

where T_e is the elastic lithosphere thickness, ρ is the mantle density, g is the acceleration due to gravity on Venus' surface, E is Young's modulus, and ν is Poisson's ratio. We developed a grid search algorithm, to find the best fit from equation 1, and the elastic lithospheric thickness (T_e) from equation 3.

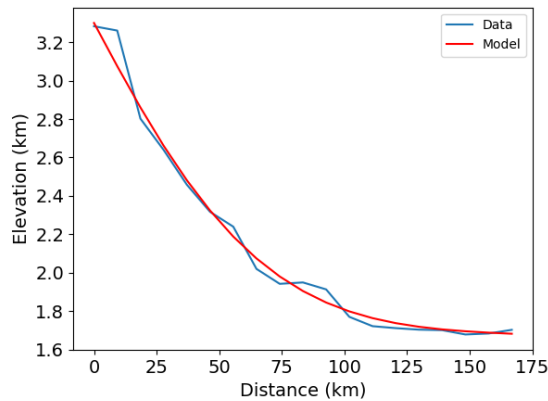


Figure 4. Flexure modeling of the Western flank of a topographic profile on Segment A. The blue line is altimetry data reported from Magellan and the orange line is the flexural model generated by equation 1.

The model matches the topography data with a high degree of fit as a result of trying ~75 million possible parameter combinations. The fit between the model and the profile is assessed using the Root Mean Square (RMS) misfit metric, which is 54 meters for this fit, which is similar to the vertical resolution of the Magellan altimeter measurements. The estimated lithospheric thickness for this profile is 23 km.

For some profiles, we found that there was sufficient “geologic noise” in the form of elevation changes unrelated to flexure along the profile that we could not reliably determine the elastic thickness.

Discussion: The maximum rift flank heights are 4.5 to 6 km for segment A and 4.5 to 5.5 km for segment C. In contrast, segment B has lower maximum rift flank heights of around 3.5 km (Figure 2). Segment B is also narrower than segments A and C (Figure 3).

The simplest interpretation of the bend in the rift is that for segments A and C, the rift is propagating radially away from the upwelling plume in central Atla Regio. This configuration ensures that the extensional stresses are optimally oriented to produce extension. In contrast, we hypothesize that at segment B is that there is a preexisting weak zone in the lithosphere that would reorient the rift during propagation. An example

of this on Earth is the Red Sea rift, where strength heterogeneity of the lithosphere results in a reorientation of the rift zone [10]. Because of the large change in direction of the rift relative to the imposed stress field, the extensional stresses would be less capable of producing a prominent rift, consistent with our observations of lower maximum rift flank heights and a narrower rift in segment B.

Our results compare with estimates of elastic thickness from gravity modeling of the major volcanic rises on Venus (Atla Regio, Bell Regio, Beta Regio, and Western Eistla Regio) of 10-30 km [6, 7]. The Rio Grande Rift on Earth has an elastic lithosphere thickness of 23 km based on flexure modeling similar to that performed here [8].

Acknowledgments: This work was supported by NASA through the Lunar and Planetary Institute (LPI) during the 2022 summer intern program. The LPI is operated by Universities Space Research Association (USRA) under a cooperative agreement with the Science Mission Directorate of NASA.

Magellan radar and topography data was retrieved from the Planetary Data System (PDS) data to generate the results shown.

References:

- [1] Taylor F. W. et al. (2018) *Space Sci. Rev.*, 214, 35.
- [2] Ford P. G. and Pettengill G. H. (1992) *JGR*, 97, E8, 13, 103-13, 114.
- [3] Senske D. A. et al. (1992) *JGR*, 97, E8, 13, 395-13, 420.
- [4] Olsen K. H. ed, (1995) *Continental Rifts: Evolution, Structure, Tectonics*, Elsevier, *Developments in Geotectonics* 25.
- [5] Turcotte D. and Schubert G. (2014) *Geodynamics*, E3.
- [6] Smrekar S. E. et al. (1997), in *Venus II, University of Arizona Press*.
- [7] Simons M. et al. (1997) *JGR*, 131, 24-44.
- [8] Brown C. D. and Phillips R. J. (1999), *Tectonics*, 18, 6, 1275-1291.
- [9] Kiefer W. S. and Swafford L. C. (2006) *JSG*, 28, 2144-2155.
- [10] Molnar N. et al. (2020) *Earth and Planetary Science Letters*, 544, 116377.

DIVERSITY OF CALCIUM-ALUMINUM RICH INCLUSIONS IN CV, CK, AND CL CHONDRITES

X. Mouti Al-Hashimi^{1,2}, P. Mane¹, ¹Lunar and Planetary Institute, Universities Space Research Association, Houston, TX 77058, ² Arizona State University, Tempe 85281 (xmouti@asu.edu).

Introduction: Calcium-aluminum-rich inclusions (CAIs) are the first solids to have formed in our solar system and contain records of the early solar system processes [1, 2]. They are believed to have condensed from the nebular gas [3,4]. Previous studies dating these inclusions suggests their formation within the first million years of our solar system [5,6]. Additionally, they experienced secondary processing in the nebula and/or on the parent body, including condensation, evaporation, melting, and recrystallization, and aqueous alteration [7]. They are mm- to cm- sized refractory inclusions in a variety of shapes representative of their formational history [8]. Their primary mineralogy includes Ca and Al rich refractory phases such as corundum, hibonite, melilite, perovskite, spinel, Ca-Al-rich pyroxene, anorthite, and forsterite [8]. Fluffy type A CAIs have irregular shapes and high porosity, whereas compact type A and type B CAIs, show much less porosity. Therefore, there is great mineralogical, structural, and textural diversity among CAIs resulting from a range of chemical and physical processes which are evident in their textures and composition. The chemical, mineralogical, and textural analyses of CAIs allow for insight into which specific conditions and processes occurred to result in which specific characteristics. The overall objective of this study was to determine the nebular and parent body processes recorded and dominating in each of the CAIs. We report chemical, mineralogical, and textural composition of 5 CAIs from a variety of carbonaceous chondrites groups including Vigarano-like, Karoonda-like, and Loongana-like chondrites (CV, CK, CL respectively). We determined the major mineralogy and the chemical composition of the CAIs using EPMA and SEM analyses.

Samples and Analytical Methods: We analyzed CAIs from Northwest Africa (NWA) 5508, (split number: 2042), Allende (split number: 818-C-11), Northwest Africa (NWA) 12772, (split number: 2019), Coolidge, (split number: 397), and Northwest Africa (NWA) 6254 (split number: 2045). NWA 5508, Allende, and NWA 12772 have classified as CV3, Coolidge as a CL4, and NWA 6254 as a CK3 (*Meteoritical Bulletin*). The CAI in NWA 5508 having previously been studied regarding short-lived radionuclides (SLRs) and named “Saguaro” [9]. The CAIs are listed in Table 1.

We obtained back-scatter electron (BSE) mosaics of Saguaro and Quail using Phenom XL benchtop scanning electron microscope (SEM) at the Lunar and Planetary Institute. Additionally, energy dispersive X-ray spectrometry (EDS) elemental maps of some areas were also obtained for these two samples with the SEM using 15.0kV beam energy and 40 μ A emission current. We collected BSE mosaics of Hoopoe, Penguin, and Falcon using the JEOL JXA-8530F electron probe microanalyzer (EPMA) at NASA’s Johnson Space Center. We used 15kV beam energy, 30nA beam current, and 1 μ m beam diameter. Wavelength-dispersive X-ray spectroscopy (WDS) quantitative data were collected for the different mineralogical phases observed with this EPMA for all five samples included in this study. The resulting data were used to definitively determine the mineralogy of the sample and identify phases.

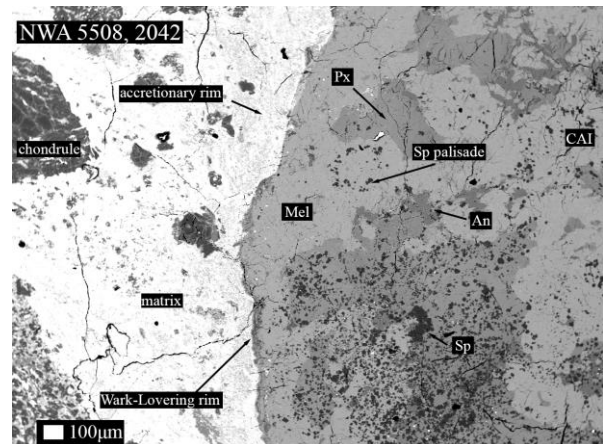


Figure 1. BSE image of a section of NWA 5508 showing CAI Saguaro. Saguaro contains melilite, anorthite, pyroxene, and spinel and is surrounded by a WL rim and an accretionary rim.

Results: NWA5508. This sample contains a CAI (Saguaro) that measures ~ 11 x 6 mm in size and is the largest of the CAIs included in this study. Saguaro is a coarse-grained CAI, and the major mineralogy includes Mg-rich spinel, Al-rich pyroxene, anorthite, and Mg-rich melilite (Table 1). Melilite shows compositional zoning. Saguaro also contains perovskite and spinel. Spinel appears euhedral shape and occur as clusters and as spinel palisades [10]. Two rim sequences surrounded most of the sample: the inner rim being a thin, Wark-Lovering (WL) rim ~3um

wide and the outer accretionary rim generally larger but varying in thickness around the sample. The WL rim contained pyroxene and spinel. Refractory metal nuggets were present throughout the sample but were more prevalent along the edges near the WL Rims (Figure 2). Spinel contains 0.26-0.77 wt% VO₂, 0.17-0.23 wt% Cr₂O₃, and 0.12-0.72 wt% TiO₂. Pyroxene contains 0.06-0.54 wt% VO₂, 0.04-0.09 wt% Cr₂O₃, 0-0.05 wt% Y₂O₃, 0.04-0.25 wt% Sc₂O₃. Rim spinel contains 0.03-0.42 wt% VO₂, 0.19-0.22 wt% Cr₂O₃, 0.22-0.28 wt% TiO₂. Rim pyroxene contains 0.035-0.17 wt% Cr₂O₃, 0.14-3.86 wt% TiO₂. Anorthite contains 0.02-0.06 wt% TiO₂. Melilite contains 0.05-0.20 wt% Sc₂O₃.

Allende. This CAI (designated as Quail) measures ~ 4 x 1.5 mm in size. It is a fine-grained inclusion containing sodalite, melilite, nepheline, hedenbergite, and Mg-rich spinel (Table 1). This CAI is surrounded by a rim of matrix-like material that contains an olivine inclusion, and then another rim of CAI-like material separating it from the main matrix of the sample. The CAI did not contain any metal assemblages. Spinel contains 0.28-0.45 wt% Cr₂O₃, and 0.05-0.07 wt% VO₂,

NWA 12772. The CAI in this sample (designated as Hoopoe) is ~ 6 x 4mm in size. The major mineralogy includes hibonite, Mg-rich spinel, melilite, anorthite, and perovskite (Table 1). Zoning was observed in some hibonites. Melilite presented with two distinct textures. One texture consisted of smooth melilite that appeared homogenous, while the other appeared to consist of many fine fractures. Hibonite appears to be replacing spinel and spinel often appears clustered. A thin Wark-Lovering inner rim surrounds the CAI, except for the edge of sample/chondrite. An accretionary outer rim is also present around the sample and is significantly thicker than the WL inner rim. Metal assemblages were present throughout the sample but mostly appeared concentrated near the WL rims. Hibonite contains 0.35-1.0 wt% VO₂, 0.04-0.08 wt% Cr₂O₃, 0.02-0.07 wt% Sc₂O₃. Spinel contains 0.60-0.99 wt% VO₂, 0.12-0.20 wt% Cr₂O₃, 0.11-0.61 wt% TiO₂. Perovskite contains 0.46-0.71 wt% VO₂, 0.01-0.19 wt% Y₂O₃, 0.06-0.20 wt% Sc₂O₃, and 0-0.34% ZrO₂. Anorthite contains 0.01-0.11 wt% Y₂O₃. Melilite contains 0.01-0.18 wt% Y₂O₃, and 0.04-0.08 wt% Sc₂O₃.

Coolidge. This CAI (designated as Penguin), measure ~ 7 x 4 mm and is fine-grained. The major mineralogy includes Mg-rich spinel and Mg-rich pyroxene (Table 1). Zoning was visible throughout the pyroxene populations as it was with the CAI in the NWA 5508 section. Minor mineralogy also included olivine. Additionally, layered mineral phases metal assemblages were present. Spinel contains 0.18-0.24 wt% VO₂, 0.39-6.61 wt% Cr₂O₃, and 0.02-2.31% TiO₂.

Pyroxene contains 0-0.057 wt% Cr₂O₃, 0.01-0.143 wt% TiO₂, and 0.03-0.05 wt% Sc₂O₃.

NWA 6254. The CAI in this sample (designated as Falcon) is ~ 10 x 8 mm in size and is fine-grained. The major mineralogy includes Mg-rich pyroxene, nepheline, and anorthite and the minor olivine. Additionally, the CAI contained barium sulfate and a carbonate. Pyroxene contains 0.02-0.21 wt% VO₂, 0-0.07 wt% Cr₂O₃, 0.0-9.9 wt% TiO₂, and 0.02-0.09 wt% Sc₂O₃. Nepheline contains 0-0.41 wt% VO₂, 0-0.22 wt% Cr₂O₃, 0-0.183 wt% TiO₂, and 0-0.18 wt % Sc₂O₃. Anorthite contains 0-0.56 wt% VO₂, 0-0.15 wt% % Cr₂O₃, 0-0.29 wt% TiO₂, and 0-0.29 wt% Sc₂O₃. Olivine contains 0-0.07 wt% Sc₂O₃, 0-0.07 wt% TiO₂, and 0.01-0.10 wt% Cr₂O₃.

Section	Type	CAI	Proposed Classification	Weathering & shock grade (Met. Bulletin)
NWA 5508	CV3	Saguaro	Type B	Medium S2
Allende	CV3	Quail	Fine-grained CAI Aqueously altered	Fall N/A
NWA 12772	CV3	Hoopoe	Compact transitional type A and B	N/A
Coolidge,	CL4	Penguin	Unassigned	W2 C-S2
NWA 6254,	CK3	Falcon	Coarse-grained CAI, Type B-like	Moderate Stage 1

Table 1. The samples included in this section and their corresponding CAI, the CAI name, classification, and weathering and shock grade.

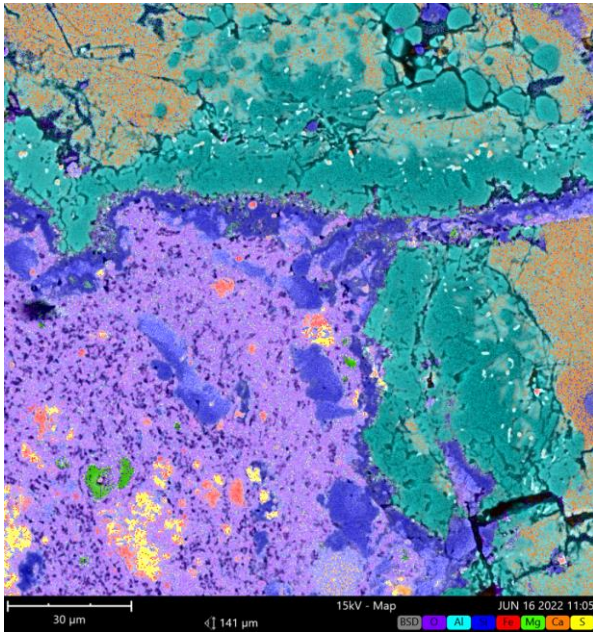


Figure 2. False-Color elemental map of the rim of Saguaro taken with the LPI Phenom XL SEM. Elements displayed are O, Al, Si, Fe, Mg, Ca, and S.

Discussion: The CV3s CAIs analyzed in this study were classified based on their mineralogy and textures into Type A versus Type B CAIs (Grossman, 1980). Saguaro (NWA 5508) shows presence of melilite, anorthite, Al-rich pyroxene, and spinel and shows coarse-grained texture, therefore is classified as Type B (Table 1). Hoopoe (NWA 12772) contains hibonite, spinel, melilite, anorthite, and perovskite and the texture suggests that it has undergone partial melting. Therefore, it is classified as a compact transitional type A and B. Quail (Allende) is a fine-grained CAI that shows the presence of sodalite, nepheline, and hedenbergite which are products of aqueous and thermal alteration [7]. Penguin (Coolidge) is fine-grained inclusion that shows unusual mineralogy. Falcon (NWA 6254) was classified based on a similar set of characteristics outlined in a previous study of another CK [11]. It is therefore classified as a coarse-grained, Type B-like CAI.

Refractory metal nuggets. These metal assemblages were present in all CAIs in this study except for Quail (Allende). While present throughout the sections, these assemblages tended to be concentrated along the boundary of the CAI and its corresponding WL rim. The formation mechanisms of RMNs include crystallization from refractory metal-enriched liquid because of their higher abundance in igneous CAIs [12] and nebular condensation due to their refractory nature [13]. The presence of RMNs in chondritic components other than CAIs suggests that multiple processes could have

contributed to their formation [14]. The RMNs present in Saguaro have likely experienced multiple processes. **Spinel palisades.** Spinel palisades, such as those in Saguaro, have two proposed origin hypotheses. The first being that they were solid CAI-like objects taken in by the larger host CAI [10]. Another mechanism proposed is their formation in situ as the remains of bubbles filled with melt, which is supported by the presence of Mg-rich melilite [15]. The presence of spinel palisades present in Saguaro are consistent with the melting and recrystallization experienced by this CAI.

Barium sulphate. Found only in Falcon the presence of barium sulphate likely results from terrestrial alteration, especially given the presence of a carbonate in the same section [16].

Conclusions and Future Work: In conclusion, Future work will use a Laser-Ablation Inductively Coupled Mass Spectrometer (LA-ICP-MS) for further analysis into the trace elements of some of the CAIs.

Acknowledgments: We thank Justin Simon for his advice and Jake Setera, and Tabb Prissel for their assistance with the analysis. This material is based upon work supported by NASA through the Lunar and Planetary Institute (LPI) during the 2022 intern program. The LPI is operated by Universities Space Research Association (USRA) under a cooperative agreement with the Science Mission Directorate of NASA. We thank the ASU Center for Meteorite Studies for the samples used in this work.

References: [1] Connelly J.N. (2012) *Science*, 338, 651-655. [2] MacPherson G. J. (2014) *Treatise on Geochem.*, 2, 139-179. [3] Grossman L. (1972) *GCA*, 36, 597-619. [4] Ebel, D.S. (2006) *Meteorites and the Early Solar System II* (D. S. Lauretta & H. Y. McSween, Eds.) 253-277. [5] MacPherson G. J. (2012) *Earth Planet. Sci. Lett.*, 331-332, 43-54. [6] MacPherson G.J. (2017) *GCA*, 201, 65-82. [7] Krot A.N. (1995) *Meteoritics & Planet. Sci.*, 30, 748-775. [8] Grossman L. (1980) *Ann. Rev. Earth Planet. Sci.*, 8, 559-608. [9] Dunham E. T. (2022) *GCA*, 324, 194-220. [10] Wark and Lovering (1982) *GCA*, 46, 2595-2607. [11] Chaumard N. et al., (2014) *Meteoritics and Planetary Sciences*, 49, 419-452. [12] Schwander (2015) *Met. and Pl. Sci.*, 50, 893-903. [13] Han et al., (2017) *GCA*, 201, 136-154. [14] Daly L et al., (2017) *GCA*, 61-81. [15] Simon and Grossman (1997) *Maps*, 31, 1, 61-70. [16] Ash R.D (1994) *Meteoritics*, 29, 49.

The role of Pluto's ocean's salinity in supporting nitrogen ice loads within the Sputnik Planitia basin. A. L. Nguyen^{1,2} and P. J. McGovern¹, Lunar and Planetary Institute (USRA), Houston, TX, 77058, ²Vassar College, Poughkeepsie, NY, 12604.

Introduction: The New Horizons spacecraft encountered Pluto in 2015 and collected unprecedented high-resolution imaging and spectroscopic datasets and allowed production of stereographic topography data [1]. One of the prominent features on Pluto, the Sputnik Planitia (SP) basin, is a roughly 870,000 km² impact basin that is filled with nitrogen (N₂) ice (Fig. 1) [2]. The N₂ ice constitutes a load on the icy shell lithosphere of Pluto. Stresses induced from loading create the observed tectonic fractures and faulting.

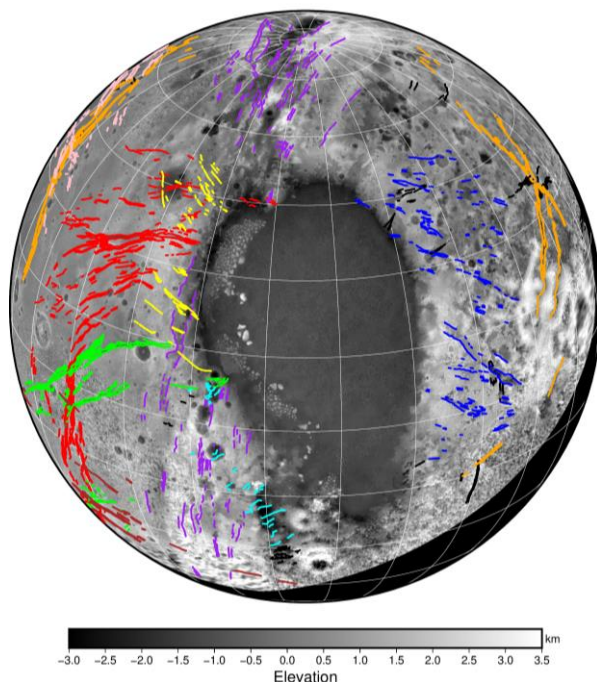


Figure 1: Topography [3] and tectonics [4] of the hemisphere of Pluto centered on the Sputnik Planitia basin (173° N, 25° N E). Different colored lines represent fault groups [1]. Figure created in the pyGMT mapping software [5].

A previous study [4] determined the conditions under which the observed N₂ ice level fill (-2 km beneath the surrounding plains) and faulting could be accomplished. These conditions include a 40-75 km shell thickness and an initial (undeformed) basin depth less than 4 km. In order to satisfy the fill level constraint, models with deeper initial basin depths would need to have thicker fill loads. These larger fill loads would generate enormous stress magnitudes that would predict much more fracturing than observed. However, mitigating conditions such as the possibility of a saltier (and therefore denser) subsurface ocean on Pluto could

provide more buoyant support to the overriding lithosphere, and thereby allow deeper initial basins.

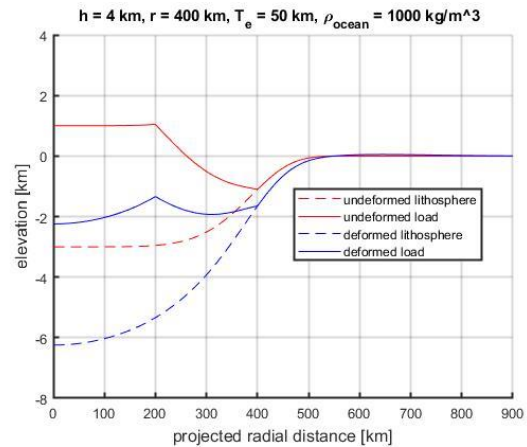


Figure 2: Surface relief (solid lines) and basin topography (dashed lines) versus distance from the symmetry axis (measured on the surface of a sphere), for an analytic model of shallow spherical shell loading [6, 7] corresponding to the dimension of SP. Load topography is expressed as a truncated cone with central height h and radius r , and basin topography is calculated as a “pan-shaped” super-gaussian profile [4] with characteristic width $w_c = 400$ km and exponent $p = 6$. Red lines depict the pre-loading configuration, and blue lines depict the deformed state.

Previous studies of SP basin loading [4, 8] did not account for the possibility of a more saline subsurface ocean and what effects it would have on the response to loading. Understanding the relative importance of ocean salinity effects on the basin-filling of SP is crucial to constrain our knowledge on initial loading parameters of the basin. In accounting for variance in ocean salinity, we can obtain a more accurate estimate for Pluto's shell thickness and thus subsurface ocean thickness. Through analytical and numerical models, we account for variance in ocean salinity, and we put reasonable bounds on local geophysics. Therefore, we seek to quantify the extent to which salinity affects the mechanics of ice shell loading on Pluto.

Methods: Analytic Models. We adapted a model of lithospheric loading in a shallow spherical shell axisymmetric formulation [6, 7] to Pluto conditions. We calculated models using a regular grid of parameter values covering shell elastic thickness T_e , load central height h_0 , load radius r_0 and ocean density ρ_{ocean} . In practice we fix r_0 to the range 400-450 km as

constrained by topography of SP [4] and add an additional variable d_0 representing the initial depth of the basin (Fig. 2). We assume that d_0 is small compared to the shell thickness so that the response of the shell is not significantly affected. We consider a range of T_e that overlaps the range considered by [4].

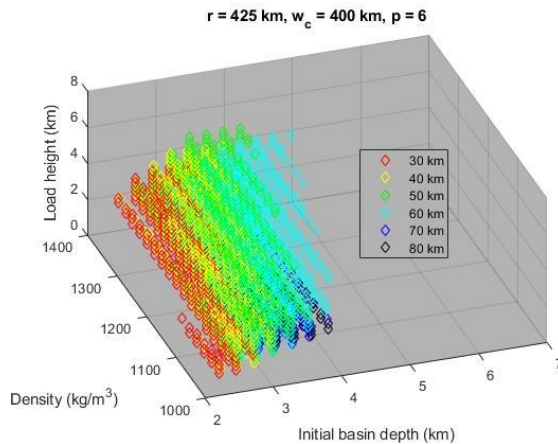


Figure 3: Four-dimensional rendering of parameter distributions for successful models of spherical shell loading (e.g., Fig. 2), as determined by elevation and stress criteria defined in the text. Three spatial dimensions show initial basin depth d_0 , Pluto ocean density ρ_{ocean} , and central load height h_0 . Load height $r = 425$ km. Symbol colors show model shell thickness T_e with values 30-80 km in 10 km increments, in red, yellow, green, cyan, blue, and black, respectively.

Constraints. We implemented topography and stress-based constraints to evaluate a goodness of fit of the analytic models to the observations of N_2 ice topography (Fig. 2) and surface ice tectonics (Fig. 1). The load surface model level is constrained by the -2 km offset of N_2 ice and surrounding plains surfaces [4], and goodness of fit is evaluated via a root mean square technique (misfit < 0.5 km). We use the horizontal stress components σ_h and σ_ϕ , (in-plane and out-of-plane, respectively) to evaluate potential fault mechanisms and orientations [9] and failure (using a Mohr-Coulomb failure criterion with internal friction angle $\phi = 30^\circ$ and cohesion $c = 1$ MPa). Successful models must be consistent with the following observations at SP [4]: 1) A strong radial normal faulting regime in the region immediately surrounding the basin. 2) Complete absence of evidence for concentric normal faulting. 3) Faulting observed for large distances beyond the SP margin (~ 1000 km) 4) a distal strike-slip regime is consistent with increasingly oblique-to-radial fault orientations with increasing distance from SP in a possible trans-tensional regime [4]. We note that complementary stress generating mechanisms such as True Polar Wander [e.g. 8] are also likely to be operating in regions distal to SP. We calculate the

lengths l_f of zones over which failure is predicted for radial normal, concentric normal, and strike-slip stress regimes. We reject models that have small l_{fn} for radial normal faulting, excessive l_{cn} of concentric normal, and a ratio $l_{\text{fss}}/l_{\text{fn}} > 2$. We also reject models with maximum magnitude of either horizontal stress > 7.5 MPa, indicating a condition of pervasive failure through most of the thickness of the shell that would be inconsistent with the preservation of the load and the moderate amount of faulting observed [4].

Numerical Models. We also used Finite Element Method (FEM) models in COMSOL Multiphysics to delve into more complex physics such as spatial variations in lithospheric shell thickness. In using COMSOL, we trade off ease of computation in MATLAB for models that can better account for the impact setting of SP. We use a process [4] where the initial load is iteratively adjusted to fit the observed basin depth. We calculated models with explicit representation of basin topography at the surface, for both uncompensated and compensated cases.

Results: Analytic Models. Successful analytic models (Fig. 3) have initial basin depths d_0 spanning the range from 2 to 5 km; the values spanned modestly increase with increasing ρ_{ocean} . The upper limit of 3.75 km at $\rho_{\text{ocean}} = 1000$ kg/m³ is consistent with the 4 km upper bound found by [4]. We determined gaussian fits [10] to the distributions of d_0 for values of load radius $r = 400$ km, 425 km, and 450 km, with values of 2.95 ± 0.45 km, 3.13 ± 0.46 km, and 3.62 ± 0.97 km, respectively. For the models shown in Fig. 3, load height is positively correlated with basin depth, and increasing ρ_{ocean} shifts the ranges of both d_0 and load heights h_0 to higher values.

Numerical Models. For both uncompensated (not shown) and compensated basin models (Fig. 4), as ρ_{ocean} increases (i.e., moving clockwise in Figs. 4A-C), the radial extent of predicted failure fault zones (the region enclosed between dashed lines) decreases, and values of fault type parameter $A\psi$ decrease. As ρ_{ocean} increases, $A\psi$ decreases from strike-slip to radial normal values at low T_e (e.g. Fig. 4A) and from radial normal to concentric normal values at higher T_e (e.g. Fig. 4B, C).

Discussion: Our findings show us that increasing ρ_{ocean} resembles increasing T_e in some but not all aspects. For example, increasing either ρ_{ocean} or T_e while holding the other constant (Fig. 4) results in a decrease in the width of the zone of faulting (due to decreasing stress magnitudes) and a decrease in $A\psi$ values that for high- T_e models increases the incidence of predicted circumferential normal faulting, in opposition to the tectonic record [4]. One key difference is that increasing ρ_{ocean} does not produce a substantial difference in the characteristic wavelength of deformation, as

demonstrated by the characteristic narrowness of the band of radial normal $A\psi$ values seen for all low T_e models (e.g., Fig. 4A).

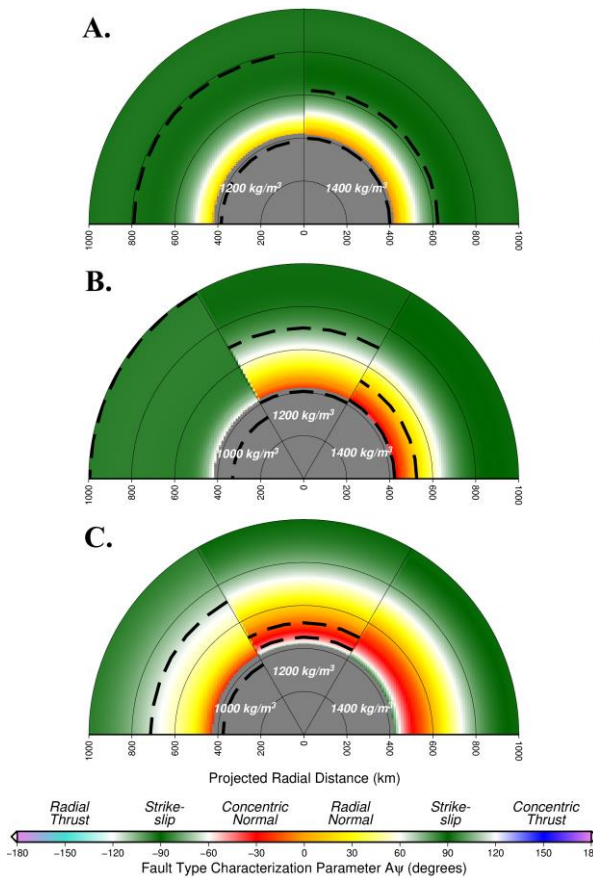


Figure 4: COMSOL Multiphysics FEM models of SP basin loading with isostatic compensation of initial basin topography [after 4]. Fault type characterization parameter $A\psi$ (color scale) and the bounds of locations where the failure criterion is satisfied (regions falling between the black dashed arcs) as functions of projected radial distance r_{proj} for each of three uncompensated loading models. Left to right (moving clockwise) on each plot shows increasing ρ_{ocean} (representing the effect of increasing ocean salinity). Shell thickness vary as A) 30 km, B) 50 km, C) 70 km. Note that A) only has two models due to a 30 km-thick compensated shell not being able to support a load at normal water density.

Our findings confirm the result from [4] that the pre-fill depth of the SP basin must have been relatively shallow. The maximum value for $d_0 = 3.75$ km at $\rho_{ocean} = 1000$ kg/m³ corresponds closely to the previously determined 4 km value [4]. Increasing ρ_{ocean} to the upper limit considered here (1400 kg/m³) only increases this upper limit to about 5 km, allowing the general concept of a shallow, pan-shaped initial configuration of the SP basin [4] to stand.

Our results suggest possible bounds on Pluto ocean salinity from interpretation of loading models. We found that increasing ρ_{ocean} tends to enhance the appearance of features of models that are inconsistent with observations, namely, high incidence of radial normal faulting and narrow zones of predicted faulting. To counteract these effects, Pluto would need a thinner shell, although as pointed out above, thinner shells produce thin zones of predicted radial normal faulting, also at odds with observations. Such a reduction in the overall successful model solution space favors only modest Pluto ocean densification from salinity.

The density/salinity properties of oceans within outer solar system bodies is a matter of debate. Ocean densities as high as 1300 kg/m³ have been considered for oceans in Pluto [11] and Titan [12], with high salinity levels driven by intense chemical interactions between the cores and the oceans. However, applications of terrestrial ocean circulation models to Enceladus have suggested that only modest salinity values (comparable to those of Earth's ocean) are consistent with the preservation of the observed shell thickness variations in the face of heat transport by ocean circulation [13]. Thus, the need to preserve SP-related shell thickness variations over Pluto's history [e.g., 8] is also suggestive of modest salinity and ρ_{ocean} values.

Conclusions: Our work determined several effects of increased Pluto ocean density (due to salinity) in basin-loading models of Sputnik Planitia. Our findings were: **1.) A quantitative constraint on d_0 prior to deformation:** Maximum d_0 of 5 km, and a median value of: 3.13 ± 0.46 km. Increasing ρ_{ocean} allows for deeper values of d_0 towards the 5 km max. **2.) The effects of salinity on shell response to loading:** Increasing ρ_{ocean} increases support, which is similar to increasing T_e . Increasing ρ_{ocean} decreases $A\psi$ and extent of failure, diverging from observations at SP.

References: [1] Stern S. A. et al. (2015) *Science*, **350**, DOI: 10.1126/science.aad1815. [2] White O. L. et al. (2017) *Icarus*, **287**, 261-286. [3] Schenk P. M. et al. (2018) *Icarus*, **314**, 400-433. [4] McGovern P. J. et al. (2021) *JGR Planets*, **126**, DOI: [10.1029/2021JE006964](https://doi.org/10.1029/2021JE006964). [5] Uieda L. et al. (2022) *Zenodo*. v0.7.0. [6] Brotchie J. (1979) *Modern Geology*, **3**, 15-23. [7] Solomon S. C. and Head J. W. (1979) *JGR Planets*, **84**, 1667-1682. [8] Keane J. T. et al., (2016) *Nature*, **540**, 90-93. [9] Anderson, E. M. (1951) *Oliver and Boyd*, **206**. [10] Sivan. Y. (2022) *MATLAB Central File Exchange*. [11] Kamata S. et al., (2019) *Nat. Geosci.*, **12**, 407-410. [12] Lunine J. I. and Stevenson, D. J. (1985) *Astrophys. J. Suppl.*, **58**, 493-531. [13] Kang W. et al. (2022) *Sci. Adv.*, **8**, DOI: [10.1126/sciadv.abm4665](https://doi.org/10.1126/sciadv.abm4665).

MULTIPLE TECTONIC AND VOLCANIC EVENTS: GINA CRATER AREA, VENUS. Emily K. Roberts¹, Allan H. Treiman¹, Gabriel L. Eggers¹, and Justin Filiberto². ¹Lunar and Planetary Institute, USRA, 3600 Bay Area Blvd., Houston, Texas 77058 (eroberts@lpi.usra.edu); ²Code XI, NASA Johnson Space Center, Houston, Texas.

Introduction: A current controversy in the geology of Venus centers on the age(s) of its highlands – the tesserae. One view of Venus’ past is that it experienced a global resurfacing event at ~1.5 Ga, now represented mostly by volcanic plains, and that the tesserae represent earlier crust deformed in that event [1,2]. It is also argued that the resurfacing represents multiple volcanic events over long times [3,4]. The ancient age of tesserae has recently come into question [5,6]. Some tesserae include distinct morphologic units that could represent deformed plains material [5,6]; in other cases it is possible that tesserae are forming today [7]. To address this question, we are mapping a tessera-plains transition around Gina Crater, near Venus’ north pole.

Gina is a ~15 km diameter crater at 78.1°N, 76.3°E (Fig. 1), in the Snegurochka (V1) quadrangle [8]. Gina is on the western boundary of the Szél-anya Lineae belt (mapped mostly as tessera [8]), where it abuts a broad area of regional volcanic plains [9]. The area is complex, with evidence for multiple episodes of tectonism and volcanism and was specifically chosen to help constrain the timing of deformation events relative to those of volcanic emplacement.

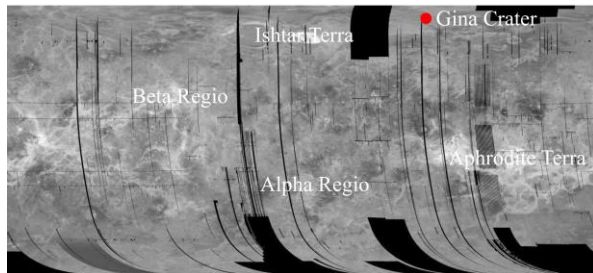


Figure 1. Location of Gina Crater at 78.1°N, 76.3°E.

Data & Methods: We used the Magellan SAR left-look global mosaic (nominally ~75 m/pix resolution) as the basemap. The area was not imaged in Magellan SAR right-look or stereo-look campaigns. The image was acquired from USGS Map-A-Planet 2 [10]. We used ArcMap 10.6 to compile our observations and the JMARS web interface for general visualizations.

Morphologies: Morphologies are defined by shape, orientation, and SAR backscatter. Tectonic features are classified as fractures/ridges, grabens, faults, and lineaments. Fractures/ridges are distinguished by their superposition & cross-cutting relationships, lengths, and connectedness. Grabens are mapped as paired SAR-dark and SAR-bright slopes. Faults are mapped where surface features are offset. Lineaments are mapped as bright, straight lines.

Map Units: Map units are identified based on dif-

ferences in radar brightness, morphology, texture, and stratigraphic relations, according to USGS guidelines [11]. Units are generally defined based on observations of emplaced material, but when material is obscured by deformation, the unit is characterized by deformation. The geologic history of the area is constructed by examination of stratigraphic relationships among units, with an emphasis placed on superposition, crosscutting, and embayment relationships. Contacts are defined by embayment relationships, radar brightness, and deformation morphology and volume.

Results: The descriptions of mapped units (Fig. 2A) are in approximate chronological order.

Fold Belt: Northwest of Gina Crater and the regional plains is a belt of SAR-bright discontinuous parallel ridges, trending NE-SW (*pdf*). The ridges average 1.5 km wide and are separated by 0.5-4 km. The belt is embayed by regional plains units (Fig. 2C) and is cut by fractures/faults of several orientations.

Regional Plains: South of the fold belt and west of Szél-anya Lineae is an area of low-backscatter plains. We distinguish eight units. Six units have low radar backscatter and are differentiated by deformation characteristics. The *pdf* unit is densely fractured or cracked in a pattern of connected polygons and is cut by wrinkle ridges. The *pdd* unit has fewer polygonal fractures, which are less obviously connected; it shows wrinkle ridges, but they are smaller and more localized than in *pdf*. The *pds* unit grades by increasing backscatter into other plains units. *Pds* shows few fractures and few short wrinkle ridges, both of which tend to be isolated from each other. The *pbn* runs adjacent to the main fracture belt. *Pbn* contains very fine-scale fractures and large wrinkle ridges that superpose *pdf* and *pdd*. The *pdb* and *pdub* units have a very low SAR backscatter and are surrounded by *pdf*, *pdd*, *pds*, and *pbn*. *Pdb* is recognized as sharply bounded patches and shows no evidence of deformation (perhaps from its low SAR backscatter), whereas *pdub* patches are diffuse. Two plains units have greater radar backscatter. The *pbs* unit is relatively smooth and is deformed by long, sinuous wrinkle ridges and lineaments, whereas *pbd* has shorter wrinkle ridges and is commonly embayed.

Gina Crater: The Gina impact crater is at the border between Szél-anya Lineae and regional plains to the west. It is recognized by its rim (*cw*), ejecta (*cre*), and floor materials (*cfh*, *cfg*) (Fig. 2B). The crater is shorter E-W than N-S, perpendicular to the dominant fabric of Szél-anya Lineae. Hills and wrinkles on the crater floor are parallel to that tectonic fabric. On the

crater floor is a small patch of low SAR-backscatter material (*cf**d*, like *pdb*). Ejecta from Gina impinges on regional plains units (above) to its west; ejecta lobes to the east (onto Szél-anya Lineae) are indistinct.

Fracture Belt / Tessera: Szél-anya Lineae is a belt of heavily deformed rock on the east of the mapped area. Its structure is primarily N-S, marked by rock layering, fractures, and faults. These are crosscut by structures oriented ENE-WSW & SW-NE, and then by others oriented NW-SE. With such multiple deformations, the area is technically tessera [8].

Shield Volcanos: Shield volcanos occur on all units (except Gina). They are recognized as domes or mounds <10 km across and are of intermediate SAR backscatter. Many have depressions at their summits, and some show lobate extensions like lava flows. In most cases, fractures and faults do not extend into/across shield volcanos from the surrounding terrain. However, some shields (& their flows) are cut by faults/fractures and obscure others (Fig. 2D).

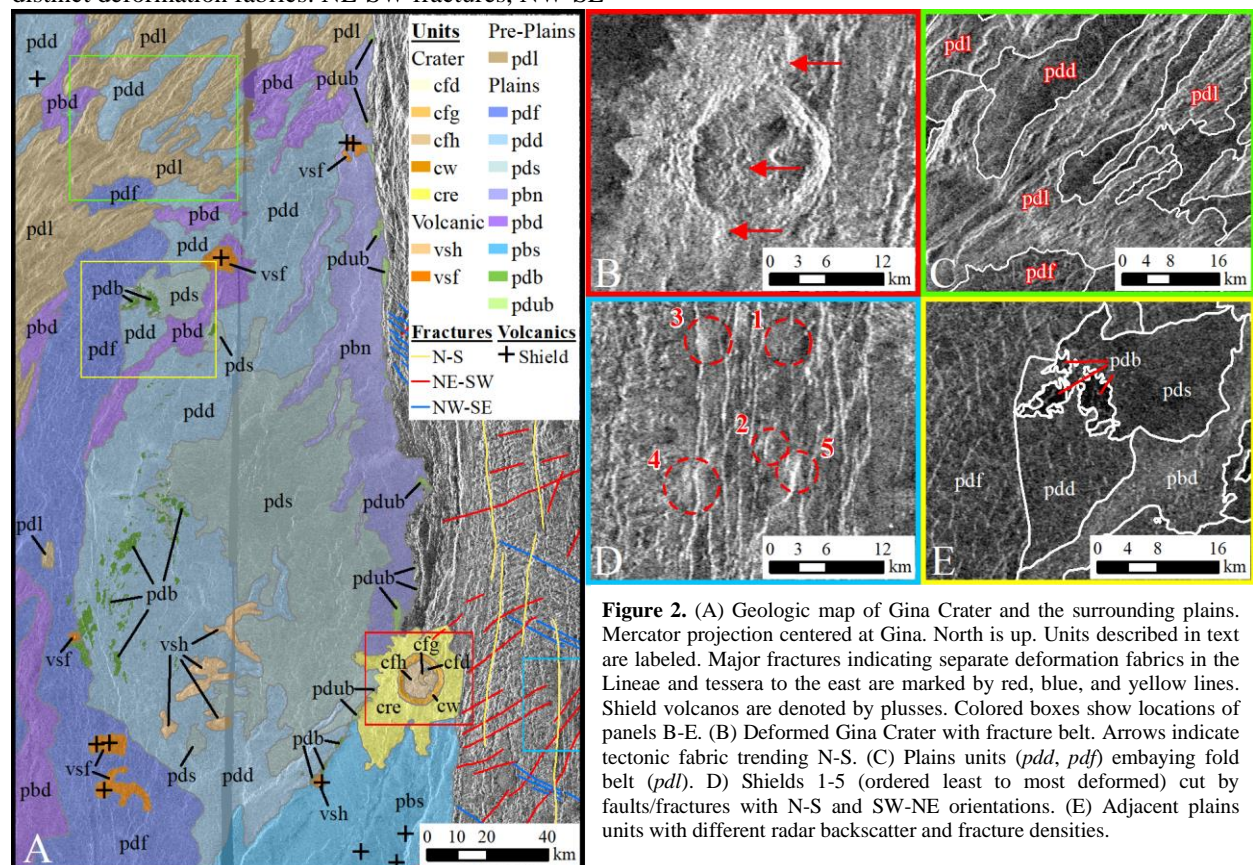
Interpretations: The Gina area is complex, with many episodes of eruption and deformation. The fold belt (*pdl*) is the oldest feature, pre-dating all the plains units. The plains are inferred to be basaltic but without detectable vents. The plains units have been deformed in multiple events. The tessera record at least three distinct deformation fabrics: NE-SW fractures, NW-SE

fractures, and N-S deformation consistent with thrust faults (matching the orientation of Szél-anya Lineae). Gina Crater is on the boundary of the Szél-anya Lineae and plains units. Its ejecta lies on the plains units, so it post-dates their emplacement. Gina pre-dates some of the E-W compression of the Lineae.

The history of the plains and tessera are difficult to link but have their interaction with Gina in common. While Gina post-dates emplacement of plains units, it appears to have impacted into tessera material and is deformed, as was the tessera. This suggests that the tessera formed in multiple episodes of deformation while ongoing volcanism emplaced neighboring units. While the specific interpretation and geologic sequence of events seems reasonable for the Gina Crater area, it may not be applicable to all tesserae.

Acknowledgment: Supported by NASA SSW grant 80NSSC17K0766.

References: [1] Schaber G.G. et al. (1992) *JGR-P* 97, 13257-13301. [2] Strom R.G. et al. (1994) *JGR-P* 99, 10899-10926. [3] Phillips R.J. et al. (1992) *JGR-P* 97, 15923-15948. [4] Hauck S.A. et al. (1998) *JGR-P* 103, 13635-13642. [5] Ghail R.C. et al. (2002) *JGR-P* 107, 5060. [6] Byrne P.K. et al. (2021) *Geology* 49, 81-85. [7] Byrne P.K. et al. (2022) *LPSC* 53, #1197. [8] Hurwitz D.M. et al. (2012) *USGS*, SIM 3178. [9] Ivanov M.A. et al. (2013) *PSS* 84, 66-92. [10] Akins S.W. et al. (2014) *LPSC* 45, #2047. [11] Tanaka K.L. et al. (1993) *USGS*, OFR 93-516.



INVESTIGATION OF GREAT SALT LAKE EVAPORITE SPECTRA FOR EVIDENCE OF MIRABILITE AND THENARDITE. W. L. Wallentine^{1,2}, K. Lynch¹, G. Eggers¹; ¹Lunar and Planetary Institute (USRA), Houston, TX, 77058, USA (Contact: vwallentine@wesleyan.edu), ²Dept. of Earth and Environmental Sciences, Wesleyan University, Middletown, CT 06459, USA.

Introduction: There is little debate about the presence of water in the history of Mars. However, there is much debate concerning the climate of early Mars. Was it ‘cold and wet’, or ‘cold and icy’ or even ‘warm and wet’? [1]. Perennially ice covered lakes (PICLs) serve as a potential analog to an early ‘cold and icy’ Mars, or as a transition point between an earlier wet Mars to the current cold and dry Mars [2, 3]. On Earth, most PICLs are found in regions near the poles that are below 0°C and arid. Near the McMurdo dry valleys of Antarctica in the Lewis Cliffs Ice Tongue, mounds of mirabilite (Na₂SO₄•10H₂O) have been observed to precipitate out of subsurface fluids [4]. Similarly, In the Great Salt Lake (GSL), mounds of mirabilite precipitate out of upwelling saturated spring water during cold, dry months. Mounds that are morphologically similar to those found in the LCIT and the GSL have been observed on Mars, with several explanations relating to upwelling of subsurface fluids, including mud volcanism and pingos [5, 6].

As winter ends in the Great Salt Lake, precipitated mirabilite begins to transform into anhydrous thenardite (Na₂SO₄). In the fossil record, this transformation preserves paleoclimate conditions as thenardite, and has been used as a paleoclimate indicator of a cool and arid period in Central Spain that correlates with an Antarctic ice expansion “Mi” event ~18.4Ma [7].

Here we take the first steps to establishing mirabilite not only as a paleoclimate indicator, but also as an indicator of ancient ice-covered lakes. On Mars, future analysis of thenardite and mirabilite may help constrain paleoclimate conditions of the red planet, help characterize subsurface hydrology, as well as provide biosignatures of extant or extinct life.

In 2015, Lynch et al. [8] published a geobiological review of the Pilot Valley Basin in the Great Salt Lake Desert Basin, demonstrating that spectroscopy of sediments is in good agreement with ground truth methods for the detection of major groups of minerals, including but not limited to smectites, sulfates, and chlorates. Since then, the importance of mirabilite as a paleoclimate indicator on Mars has become apparent, thus understanding its signature in analogous environments is key to piecing together the climate history of Mars.

Most studies of mirabilite spectra are based on pure mineralogical samples in lab settings, or in-situ studies in natural settings. As far as we can tell, there

have been no studies of natural samples observed in lab settings, especially for observing the transition of naturally occurring mirabilite to thenardite. Having an understanding of the spectral signatures associated with this transition could greatly aid researchers in remote sensing of cold, dry environments.

In addition to implications on Mars, understanding the properties of mirabilite has implications for Europa. In 1998, the Galileo spacecraft detected evidence of magnesium and sodium sulfates on Europa via near-infrared spectroscopy [9, 10]. Our understanding of the origin and characteristics of these salts on Europa are hampered by our limited observational data, which will change with the upcoming Europa Clipper and JUICE missions [11]. Due to the upcoming missions, hence developing a better understanding of these sulfates would be useful. In light of this, we performed a study to investigate two sets of samples for evidence of mirabilite or thenardite.

Analog samples: The first set was of sediment from Pilot Valley, collected by Dr. Lynch in her 2015 paper [8]. These samples served as a training set prior to wet sample observation. The second set of samples was of brine fluid collected from the north arm of the Great Salt Lake, where mirabilite mounds have previously formed. The dry samples were kept in room temperature and humidity conditions for nearly a decade, whereas the brine samples were kept sealed and in -80 °C conditions until this study.

Spectral collection: Spectra was collected using an OreXpress Portable Spectrometer, which is built on SEI’s SM-3500 platform. The OreXpress spectrometer operates in the 350-2500 nm range, covering the visible and near infrared spectrum. Dry samples were kept covered at room temperature for about ten years, only being taken out of their aluminum container for spectral observation. Wet samples were kept frozen at -80C for the same period of time, and transitioned to a -18C freezer to allow for brine deliquescence followed by spectral observation, as well as timed observation. Spectra of the timed sample were taken several days apart, depending on the sample, to allow for adequate dehydration. The first wet timed sample observations, which consisted largely of halite and water, were taken 3 days apart. The second timed sample, which was assumed to contain mirabilite, was taken one day apart. The last sample, which was also presumed to

contain mirabilite, had spectra taken 30 minutes apart.

Results: The first set of samples from Pilot Valley contained no conclusive evidence of mirabilite or thenardite. Figure 1 shows an example spectra from these samples that is indicative of gypsum. Figure 2 shows a spectra of pure gypsum, provided by the USGS spectral library

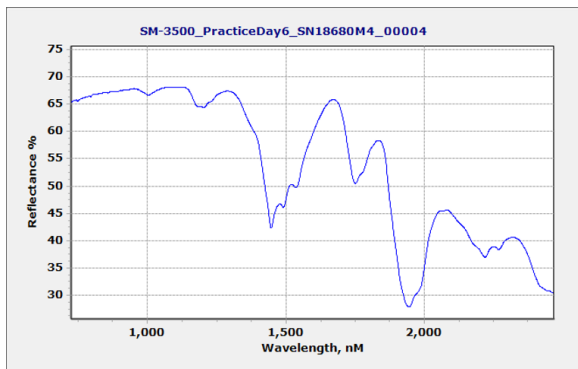


Figure 1: Sample spectra from first set of sediments.

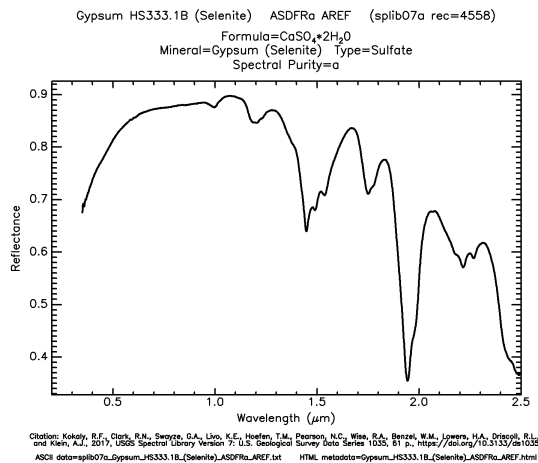


Figure 2: Spectra of pure gypsum, from USGS spectral library [12].

Conclusive detection of mirabilite was possible only when the brine sample was frozen to -80°C . As the sample returned to room temperature, diagnostic bands of mirabilite disappeared after 25 minutes, as seen in figure 3. The spectra of the first scan, where the brine sample was coldest, absorption features are also well defined. Major absorptions in the first scan occur at $1\mu\text{m}$, $1.23\mu\text{m}$, $1.34\mu\text{m}$, $1.5\mu\text{m}$, $1.64\mu\text{m}$, $1.8\mu\text{m}$ and $1.98\mu\text{m}$. After 25 minutes at room temperature and humidity, reflectance drops drastically, and features after $1.5\mu\text{m}$ are subdued or non-detectable. The only remaining absorption features at this stage are found at $1\mu\text{m}$ and $1.2\mu\text{m}$.

A separate sample of brine precipitate was left to dry for six days, coming from the same bottle as the previous sample. After six days, previously subdued absorption bands returned, as seen in figure 5, producing a well defined spectra indicative of mirabilite, as well as potential influence by other minerals present in the sample.

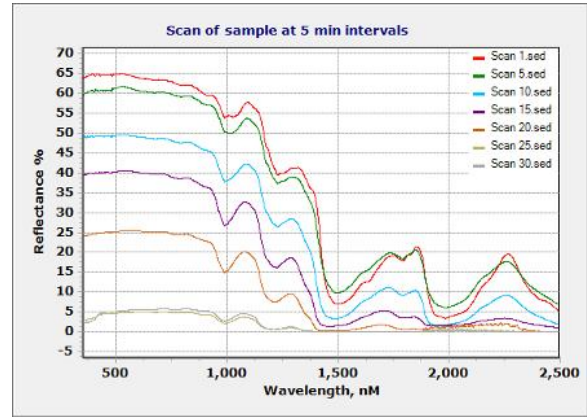


Figure 3. Spectra of frozen sample taken at 5 minute intervals.

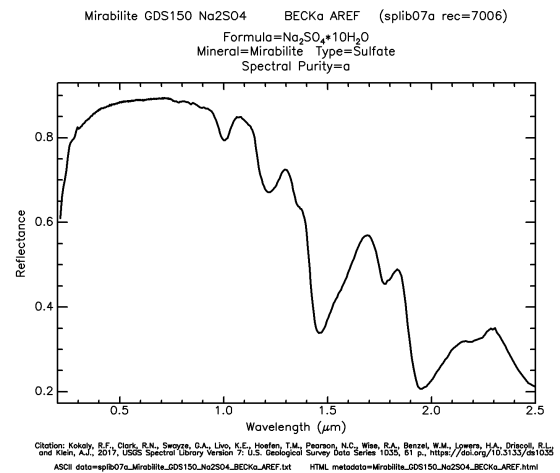


Figure 4. Spectra of pure mirabilite, from USGS spectral library [12].

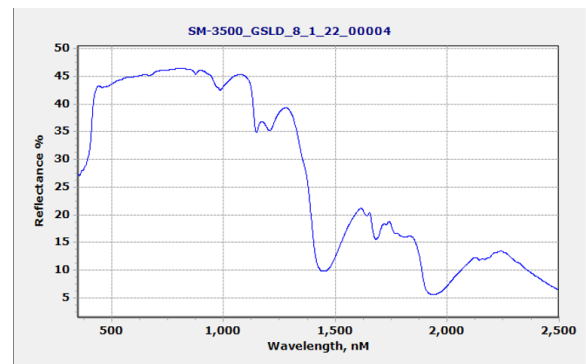


Figure 5. Spectra of brine precipitate left to dry for 6 days.

Discussion: The absorption features found in the frozen brine samples are consistent with those found by De Angelis et al. (2021) of mirabilite [13]. Being a decahydrated sodium sulfate, most of the absorption features can be attributed to water. Specifically, the features at 1 μm , 1.2 μm , 1.5 μm , 1.8 μm , 1.98 μm , are all due to water [13]. Many of the spectral features are also consistent with the mirabilite spectra found on the USGS mineral spectral library [12]. However similar the location of the absorption bands are, the magnitude of reflectance varies. Use of advanced analytical software, such as Envi, would solve this issue.

As the sample warmed, the conclusive diagnostic features of mirabilite after 1.5 μm flattened and ultimately disappeared. This could be attributed to spectral masking by halite, as these features are associated with square crystal formation, and there is no immediate evidence of rapid mirabilite transformation into thenardite. Loss of the hydration bands after 1.5 μm but not 1 μm and 1.2 μm could be evidence of transformation into a semi-hydrated state, sodium sulfate heptahydrate ($\text{Na}_2\text{SO}_4 \cdot 7\text{H}_2\text{O}$). It is unlikely that these bands are evidence of thenardite, as thenardite has only one diagnostic band in the VNIR range, being 1.9 μm . This evidence reaffirms that mirabilite forms under cold conditions, and that warming conditions make detection harder.

Indeed, transformation of mirabilite into thenardite is temperature dependent, but also regulated by the chemical context of the environment. It is known that in presence of NaCl, dehydration into thenardite drops from 32°C to 18°C, whereas presence of Mg^{2+} drops it down to 16°C [10]. The Bonneville basin, where the studied brine samples came from, is known for its extensive halite (NaCl) deposits, as well as its deposits of potassium chloride and magnesium chloride [14].

The lack of evidence for mirabilite or thenardite in the first set of samples could be due to the limited analysis techniques used. Due to technical difficulties, we could not employ Envi for detailed spectral analysis, and instead had to rely on spectral library comparisons. It is known that gypsum tends to

Conclusion: Evidence of mirabilite in frozen brine from the great salt lake was found using visible-near infrared spectroscopy. Mirabilite from partially desiccated brine fluid was also found via VIS-NIR spectroscopy. These preliminary findings shed light on the utility of that the Great Salt Lake as an analog for mirabilite studies. Mirabilite and thenardite have been suggested to exist on Mars and Europa but no mission has prioritized detection of these sulfates [4, 11, 15]. Understanding the processes linked to formation and deposition of these minerals will be a key aspect of planetary science

missions in the future. Before missions can be launched, adequate analog studies on Earth must be performed so as to have enough data ready for comparison.

Acknowledgements: This study was conducted in tandem with the LPI Summer intern program in Planetary Science and funded by the Wesleyan College of Environment Summer Fellowship. Special thanks to Claudia Bellard for her continued support.

References: [1] Wordsworth, R.D., (2016) *Annu. Rev. Earth Planet. Sci.*, 44, 381-408. [2] McKay, C.P. and Davis, W.L. (1991) *Icarus*, 90, 214-221. [3] Rivera-Hernandez, F. et al., (2018) *Sedimentology*, 66, 917-939. [4] Socki, R.A. et al., (2012), *LPSC XLIII abstr. #2718*. [5] Burr, D.M. et al., (2009) *Planet Spce. Sci.* 57, 541-555. [6] Oehler, D. Z. and Allen, C.C., (2010), *Icarus*, 208, 636-657.. [7] Herrero, M.J. et al., (2015) *Clim. Past*, 11, 1-13. [8] Lynch, K.L. et al., (2015), *J. Geophys. Res. Planets*, 120. [9] McCord, T.B., et al., (1998a) *J. Geophys. Res.*, 103, 8603-8626. [10] McCord, T.B., et al., (1998b) *Science*, 280, 1242-1245. [11] De Angelis, S., et al., (2017) *Icarus*, vol. 281, pp. 444-458. [12] Kokaly, R.F. et al., (2017), *US Spec. Lib.*, v. 7. [13] De Angelis, S., et al., (2021) *Icarus*, vol. 357, 114165. [14] Lines, G.C., (1979), *BLM*, 2057. [15] McCord, T.B., et al., (2001), *J. Geophys. Res. Planets*, 106, 3311-3319.

EVALUATING BOILING CURVES AND THEIR IMPLICATIONS FOR IMPACT-GENERATED HYDROTHERMAL SYSTEMS ON MARS. M. R. Westenberg^{1,2}, E. G. Rivera-Valentín¹, K. L. Lynch¹, and D. A. Kring¹; ¹Lunar and Planetary Institute (USRA), Houston, TX 77058, ²Department of Biochemistry, Molecular Biology and Biophysics, University of Minnesota–Twin Cities, Minneapolis, MN 55455 (weste485@umn.edu)

Introduction: Hydrothermal activity can be produced from an impact on any terrestrial body containing fluid or ice in the planetary crust [1]. Impact cratering generates heat and a permeable subsurface structure for circulating fluids [1], which could support thermophilic organisms [2]. Such craters may be promising locations to discover evidence of microbial life on Mars [2]. The potential for life in that setting is demonstrated by the ~180 km diameter Chicxulub impact crater which contained a microbial population in a hydrothermal system that may have been habitable for over 2 million years [3]. Chicxulub is the only large, intact peak ring basin on Earth and is therefore often used as a model for hydrothermal systems on Earth and Mars [1].

Several environmental factors explored here may limit microbial habitability of an impact-generated hydrothermal system: temperature, pressure, water activity, and whether the fluids are in a boiling or liquid state, among others [4]. To sustain thermophilic organisms, temperatures between 50°C and 120°C are required [3]. Liquid water must be stable, which will occur as a hydrothermal system evolves [1]. The water activity of the liquid will also impact this stability zone [5]. Water activity (a_w) is a measure of the amount of free water molecules in an aqueous system. A value of 1 indicates pure water and a value of 0 indicates there is no water available [5]. Almost all microbial species require water activity values above 0.6, limiting the habitability of Martian brines [6, 7]. The combination of these and other factors ultimately determines where habitable regions may have existed on Mars.

Methods: To explore the habitability of impact-generated hydrothermal systems on Mars, craters with diameters of 30, 100 and 180 km were evaluated. Boiling curves were calculated to determine the extent of boiling and liquid stability at three different locations within each crater size. Boiling curves for pure water were generated as a function of temperature and pressure using a vapor pressure equation [8]. Depth was calibrated to pressure using a standard hydrostatic equation down to the crater floor [9]. Below the crater floor and in locations without a lake, a geostatic pressure equation was used [2]. A grain density of 3.42 g/cm³ and a rock porosity of 6.64% were taken from Martian meteorite Lewis Cliff 88516 [10]. That plutonic shergottite was selected because impact-generated hydrothermal systems can extend far beneath the surface [11]. We also investigated the

stability zones for various brines of water activity $0.6 < a_w < 1$. For the regions where stable brines may occur, we investigated their temporal evolution as the solution evaporated and concentrated in salinity. Specifically, we modeled the stability of a ferric sulfate brine following the methods in [12]. Water activity was also evaluated as a function of time using temperature data from thermal models of Martian craters [1].

Results and Discussion: Martian craters are discussed here with respect to temperature, regions of boiling versus liquid fluids, and water activity.

Boiling zones in Martian hydrothermal systems. Model hydrothermal systems and boiling curves for three locations within them are shown in Figure 1. In a 180 km crater, melt is initially bounded by a peak ring and the crater rim (Fig. 1a). After 200,000 yrs, the melt sheet cools enough to become permeable and the crater center reaches 300°C and below [1]. At that temperature, fluids within the impact melt rock and underlying basalt are entirely liquid. When the system cools to thermophilic temperatures of 120°C, the impact melt rock and basalt units again contain entirely liquid solutions (Fig. 1d). In the peak ring and crater rim, boiling only occurs in the top ~10 m of basalt when thermophilic temperatures were reached. However, after 4,000 yrs, the temperature is too low for boiling to occur at that depth in either the peak ring or crater rim (Fig. 1e, f). Thermophilic temperatures are present at 4,000 yrs in the peak ring and crater rim and at 200,000 yrs in the crater center, at which point the fluids are entirely liquid. These conditions are viable for sustaining a microbial population.

A 100 km crater also initially contains melt bound by the peak ring and crater rim (Fig. 1b). However, the melt has a lower temperature than that in the 180 km crater and, thus, solidifies more quickly and becomes permeable within 20,000 yrs. When thermophilic temperatures are reached, hydrothermal fluids are entirely liquid throughout the impact melt rock and underlying basalt. In the peak ring, solutions are also liquid at 120°C except in the uppermost ~5 m of basalt where boiling persists. In the crater rim, temperatures never exceed 100°C, except at depths of ≥ 8 km, resulting in entirely liquid solutions within the vertical range of the model. Thermophilic temperatures would therefore coincide with entirely liquid solutions in the peak ring and crater rim after 500 yrs and in the crater center after 20,000 yrs.

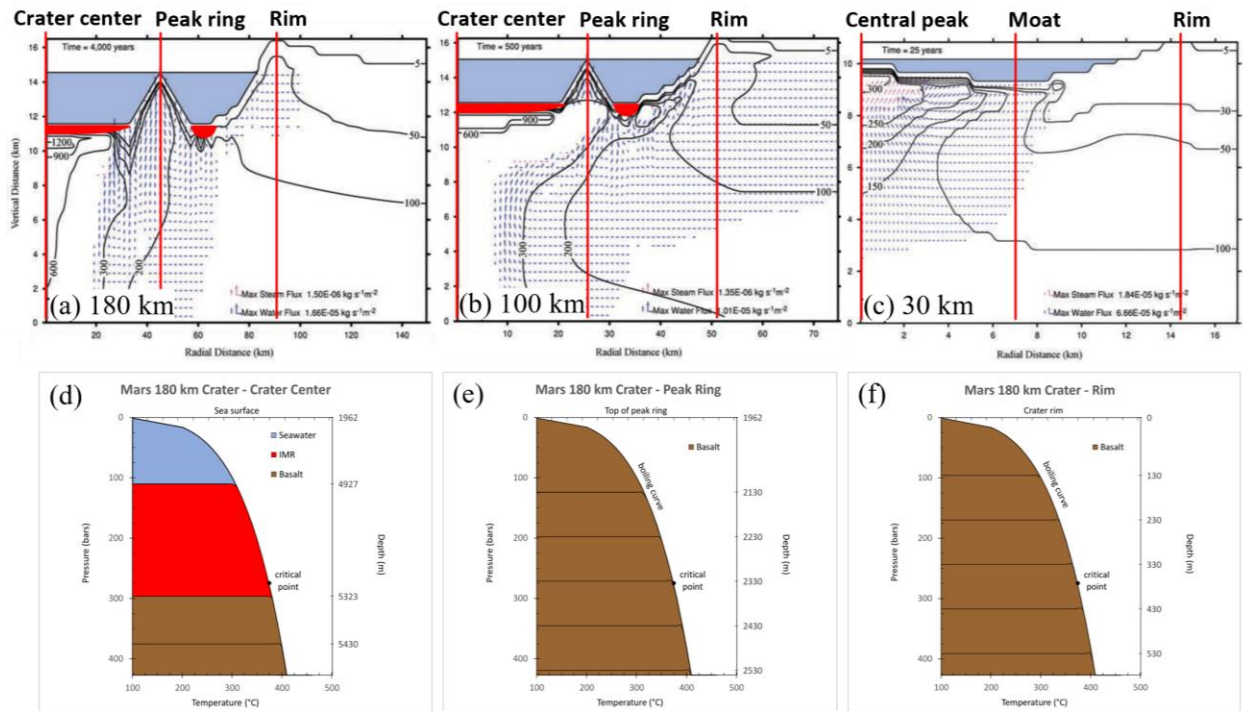


Figure 1: Boiling curves in Martian craters. Schematic diagrams for crater diameters of **a.** 180 km, **b.** 100 km, and **c.** 30 km were adapted from [1] and are depicted under initial conditions with red lines indicating the locations that were evaluated with boiling curves. The thermal evolution of each system was modeled using the initial conditions in **a-c** and is not shown here. The modeled time scale varied with a maximum of 2,000,000 years in **a.**, 200,000 years in **b.**, and 100,000 years in **c.** The boiling curves were generated for pure water with pressure and depth calibrated at the **d.** Crater center, **e.** Peak ring, and **f.** Rim of the 180 km crater as a representative example.

A 30 km Martian crater with a crater lake does not contain a melt sheet (Fig. 1c). Temperatures in the central peak are ~300°C after 25 yrs. As the temperature decreases to 120°C, any boiling ceases. In the crater moat, a thicker layer of water is present,

which further decreases the period of boiling. A ~5 m interval of boiling is possible at the top of the crater rim but is otherwise liquid to depths of several kilometers. In this size crater, thermophilic temperatures below the boiling point of water are reached quickly throughout the hydrothermal system. The effects of boiling therefore do not have to be considered as boiling was not occurring under the conditions present in those regions.

The effect of water activity. While the boiling curves in Figure 1 assume pure water, fluids on Mars likely resemble brines containing various solutes [6, 11]. This decreases the vapor pressure above the solution, which increases its boiling temperature and alters the boiling curve, as shown in Figure 2. When the water activity decreases from 1 to 0.6, the period of boiling is shortened, so fluids within the rocks spend more time in a liquid phase. Therefore, a lower water activity increases the range of depths and temperatures where liquids can be found inside a crater (Fig. 2).

In the three crater sizes that were modeled, the change in water activity has a minimal effect on liquids at temperatures of 120°C or less. In the locations where a crater lake is present, liquid water is stable throughout the entire depth of the rock regardless of the water activity. This is because only the very top of the lake would be able to boil, meaning that fluids within the underlying rock would be liquid. When a

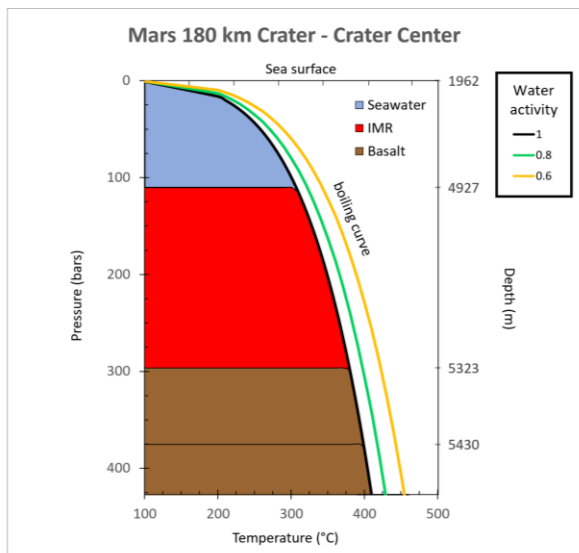


Figure 2: The effect of water activity on boiling curves in Martian craters. The boiling curves for water activities of 1, 0.8, and 0.6 are shown with solid colored lines. The center of the 180 km diameter crater was chosen as a representative example.

crater lake is not present, boiling is possible in the very top of the basalt and the depth at which this could occur is shown to move upward by a few meters each time the water activity is lowered. Therefore, in each crater size and location without a lake, a decrease in water activity results in more of the rock containing liquids. This would seem to indicate that lower water activities allow liquids to be the most readily available for the longest period, which is promising for the habitability of Martian craters. However, a lower water activity introduces physiological constraints to microbial growth; most organisms require a water activity of 0.9 or higher with 0.6 being a reasonable estimate for the minimum value that can sustain life [6]. Therefore, at lower water activities, there is a tradeoff between a longer period of liquid stability within a crater and the amount of water that is available for growth. This means that in the shallower areas where boiling is possible, the most habitable crater regions may have had an intermediate water activity between 1 and 0.6 to maximize the liquid period while also providing enough available water for survival.

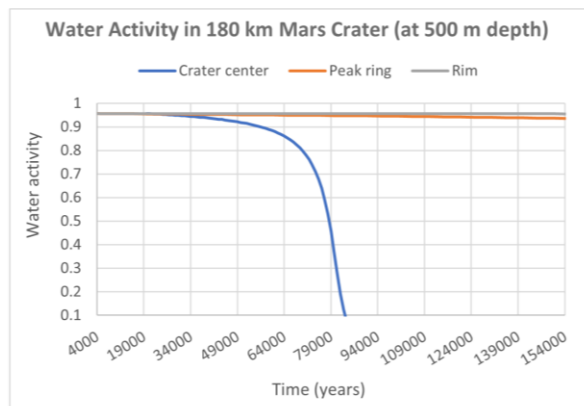


Figure 3: Change in water activity over time. The y-axis begins at 4000 years—the first time point where temperature data is available [1]. The colored lines represent different locations within a crater and are specified above the chart. The change in water activity was analyzed in each crater size at three different depths; the 180 km crater at 500 m is shown as a representative example.

The water activity was also evaluated over time at three different depths using existing thermal models [1]. Temperatures tend to be higher in the central regions and increase with depth beneath the surface [1]. Therefore, the deepest and most central areas experience the highest evaporation rate which causes a rapid loss of the brine. Regions near the surface and farther from the crater center tend to have colder temperatures [1]. This results in a lower evaporation rate and less fluctuation in water activity. Therefore, these regions are more stable which allows the brine to remain for a longer period. Conversely, deeper and

more central regions tend to have less stable brines which rapidly evaporate due to the high temperatures. The 180 km crater at 500 m is shown in Figure 3 as an example of this trend. At a depth of 100 m, the temperature is low enough that the crater size and location within a crater has no discernible effect on the lifetime of the brine. There is a rapid decrease in water activity within the peak ring at an earlier period than the central peak in the 100 and 180 km craters at a depth of 1000 m. This is the only exception to the pattern of shorter brine lifetimes in deeper and more central regions. This is due to an excess of heat generated in larger impacts which increases the time required for the central peak to cool [1]. Once it becomes permeable to fluids, the brine quickly evaporates away. The most promising locations for biological life are regions with a stable brine and long-lived habitable conditions as this allows the most time for a potential microbial population to develop [4]. Based on the trends highlighted in Figure 3, this is most likely to occur closer to the surface of a crater and farther away from its center.

Conclusion: Impact-generated hydrothermal systems can create a habitable environment for microbes, as demonstrated by the Chicxulub impact crater [3]. Using boiling curves and thermal models, we find that liquids are available in each crater once thermophilic temperatures are reached. Lower water activity values increase the stability of liquids while limiting microbial growth, suggesting a biological tradeoff within regions where boiling can occur. Brines are also shown to be more stable near the surface and farther from the crater center. These findings help constrain the regions of habitability within Martian craters and suggest areas where there may be a higher probability to detect evidence of microbial life on Mars.

References: [1] Abramov, O., and Kring, D.A. (2005) *J. Geophys. Res. Planets*, 110, 1–19. [2] Kring, D.A., and Bach, W. (2021) *Astrobiology*, 21, 1547–1564. [3] Kring, D.A. et al. (2021) *Astrobiology*, 21, 103–114. [4] Rummel, J.D. et al. (2014) *Astrobiology*, 14, 887–968. [5] Benison, K.C. et al. (2021) *Astrobiology*, 21, 729–740. [6] Tosca, V.J. et al. (2008) *Science*, 320, 1204–1208. [7] Stevenson, A. et al. (2017) *Environ. Microbiol.*, 19, 687–697. [8] Murphy, D.M., and Koop, T. (2005) *Quarterly Journal of the Royal Meteorological Society*, 131, 1539–1565. [9] Mugisidi, D., and Heriyani, O. (2018). *E3S Web of Conferences*, 73, 2–4. [10] Coulson, I. M. et al. (2007). *Meteoritics and Planetary Science*, 42, 2043–2054. [11] Schwenzer, S. P., and Kring, D. A. (2009). *Geology*, 37, 1091–1094. [12] Chevrier, V. F. et al. (2020). *Planetary Science Journal*, 1, 64.

ROUGHNESS VARIATIONS AT DIFFERENT SCALES WITHIN IRREGULAR MARE PATCHES ON THE MOON. G. M. Wolff^{1,2}, J. D. Stopar¹, E. G. Rivera-Valentín¹, ¹Lunar and Planetary Institute (USRA), Houston, TX; ²University of Colorado, Colorado Springs, CO

Introduction: Irregular Mare Patches (IMPs) are potentially young (<100 Ma), volcanic features notable for their unique bulbous mounds with uniform surface texture and topographically uneven deposits with variable rock densities [e.g., 1-5]. IMPs occur at a few volcanic shields/domes, mare rilles, and within mare plains [4]. Determining their ages and formation is important for constraining models of thermal evolution and identifying potentially unrecognized lava flow or geomorphologic processes on the Moon. Proposed formation mechanisms include lava lakes, inflated lava flows, magmatic foam/lava extrusions, volatile outgassing, and regolith drainage [list in 6]. We combine multiple data sets including Lunar Reconnaissance Orbiter Mini-RF radar data (LRO MRF) and Narrow Angle Camera (NAC) images and topography, with complementary compositional data sets to further characterize the properties and morphology of IMP deposits.

Methods: We acquired level 2 monostatic MRF data (primarily monostatic S-band, 12.6 cm) through NASA's Planetary Data System (PDS), including the Stokes parameters (S1-S4) and same-sense circular polarization (SC), opposite-sense circular polarization (OC), and circular polarization ratio (CPR = OC/SC) products. We performed m-Chi decompositions [7] to create an RGB image (single-bounce=blue, randomly polarized or volume scattering=green, and double-bounce=red). S-band collects cover large portions of the Ina, Cauchy, Hyginus, and Sosigenes Crater IMPs and their surroundings. Processed bistatic radar data, where the Arecibo Observatory S-band planetary radar acted as the transmitter and MRF as the receiver, were obtained from the MRF team; one S-band collect covers the Cauchy IMP. MRF X-band data suffer from, as of yet, uncorrected signal gradients and thus were not used in this study.

Calibrated, high-resolution LROC NAC images and topographic data (Digital Elevation Models, DEMs) were acquired from the PDS and then map-projected. The JAXA archive, LROC Team, USGS website, and ACT-REACT Quickmap webviewer [<https://quickmap.lroc.asu.edu>] provided access to complimentary data including multispectral UV-VIS-NIR basemaps from Kaguya/SELENE, Clementine, and the LRO Wide-Angle Camera (WAC). Using the gdaldem program [<https://gdal.org/>], we generated roughness maps at different scales from the NAC topographic data which are available for Ina, Cauchy, Hyginus, Nubium, and Maskelyne IMPs.

Results and Discussion: Within and around each IMP, we identified and characterized several types of deposits using the available data: interior mounds, rock-poor interior deposits, rocky interior areas, pyroclastics, mare, highlands, and crater ejecta.

Relatively radar-dark and homogenous areas (regions of ~2-7 km) in the MRF S-band S1 (total backscatter power) surrounding Hyginus and Cauchy suggest the presence of pyroclastics or similarly fine-grained, rock-poor material (**Fig. 1**), similar to descriptions in [8]. These areas share characteristics with pyroclastic and dark mantling deposits (DMD) near Mare Vaporum [9]. Similar deposits were not observed exterior to Ina or Sosigenes Crater in the available coverage. Hyperspectral Moon Mineralogy Mapper data indicates volcanic glass is not a major component around Cauchy or Ina but is present around Hyginus and within large IMPs in minor amounts [10]. Relatively low Diviner thermal inertias associated with many IMPs are also consistent with less-consolidated or rock-poor deposits within/around the IMPs [6, 11].

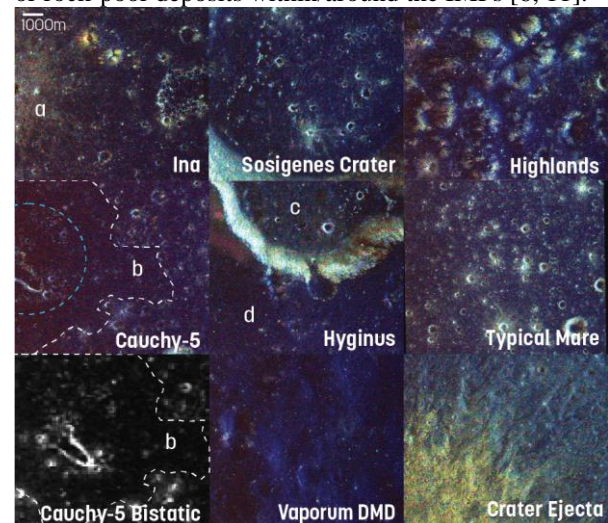


Figure 1: m-Chi radar imagery of various features at the same scale. a) fresh crater ejecta east of Ina Caldera. b) radar-dark deposit surrounding Cauchy-5 dome with an eastward extension. c) brighter floor within Hyginus. d) pyroclastic-like material outside Hyginus

Blocky units with numerous exposed rocks evident in NAC imagery are associated with higher S1 and are characterized by an intense multicolored appearance in m-chi (**Fig. 3**), the result of a high number of wavelength-scale facets with complicated geometries. Rocky spacecraft-facing slopes (e.g., east-facing for left-look) return equal values in all m-Chi parameters

due to viewing geometry. Comparatively small eastern slopes on mounds are dominated by blue in the m-Chi, consistent with a spacecraft-facing slope of smooth material at wavelength scale. Mean values of m-Chi for different deposits exhibit some variations in color (i.e., predominantly blue, purple, or yellow); the interior floor of Hyginus has a brighter, more yellow appearance resembling mare deposits or fresh impact ejecta (**Fig 1**). In all studied IMPs, mounds and certain uneven units have low backscatter returns (except those covered by rocks). Uneven patches exterior to Cauchy's central depression and those present within Hyginus and Sosigenes Crater are radar bright without the presence of rocks in NAC imagery (**Fig. 3**), suggesting buried rocks, consolidated material, or complex regolith grain properties within the upper meters. These materials are multicolored in the m-Chi, consistent with an uneven texture creating similarly complicated geometries.

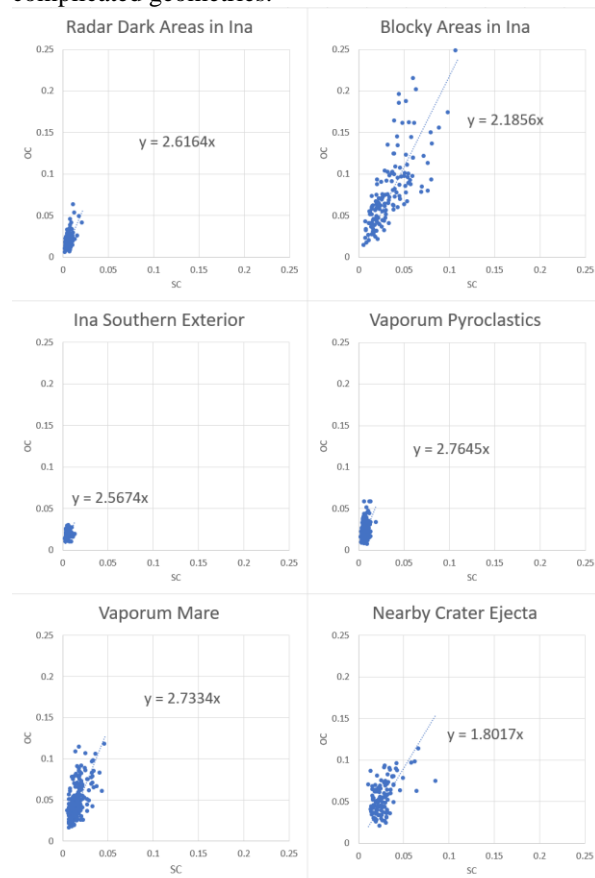


Figure 2: OC/SC plots of various deposits taken within the same radar collect. The extent represents higher S1 values while the slope is potentially attributed to physical properties of materials.

CPR, an indicator of roughness, has a high degree of noise and enhancements on spacecraft-facing slopes, but does exhibit some correlation with rocky areas.

Plotting OC and SC values for different deposit types within the same radar collect (**Fig. 2**) show differences in ranges, means, and trend slope. Differences in OC and SC values between units can be related to particle shapes, composition, ~10 cm roughness, and/or topography [12]. Our first look at these trends suggests that the radar-dark areas within Ina are potentially similar to “typical” mare or pyroclastic deposits; the blocky, radar-bright interior areas are more like “typical” crater ejecta. A more detailed statistical analysis will be performed in the future.

For most IMPs, the radar data are sensitive to ~1-2 m depths, related to Fe, Ti content [13]. Ina's center has low radar backscatter, with both the mounds and uneven deposits nearly indistinguishable. Thus, we believe a rock-poor material of at least 1-2 m to be present in all areas within Ina not dominated by rocks, in agreement with Diviner data suggesting at least 15 cm of regolith (or fine-grained material) coverage [6]. Superposed craters on mounds without excavated rocks indicates this depth may extend further.

From the NAC topographic data, we found that the largest mound in Ina does not show a roughness difference with exterior deposits, but both mounds and proximal exterior deposits (the dome) are somewhat smoother than “typical” mare at scales up to ~100-m.

NAC DEMs indicate that lower boundaries of mounds within Ina have slopes as high as 40°, with majority of slopes < 30°, the predicted angle of repose of lunar regolith and unconsolidated grains [14]. Elevation profiles across IMP interior units show that their surfaces are dissimilar to typical mature mare deposits where roughness is dominated by superposed small impact craters. Rather, the mounds are dominated by gentle swales and the uneven units have profiles reminiscent of recent terrestrial lava flows such as seen at Kilauea [5, 18].

Conclusions: Based on the observed characteristics, we identify four general units associated with IMP features: mounds, radar-dark uneven units, radar-bright uneven units, and rocky units. If the IMP features are primarily volcanic in origin, the mounds and many adjacent radar-dark areas might be volcanic deposits coated with pyroclastics ranging from scoria to ash (e.g., mildly explosive phases of the eruption) [15-17]. Uneven radar-bright units are high-albedo, typically smaller, and present either without, or outside of, depressions like Ina, Nubium, and Sosigenes Graben. The difference in radar values between uneven radar-bright and uneven radar-dark units can be attributed to level of consolidation, buried rock content, or abundance of a fine-grained surface layer. Rocky areas are concentrated mostly along the outer portions of the Ina

depression and impact craters although they are also associated with small uneven units. When rocks are present, they dominate the radar data.

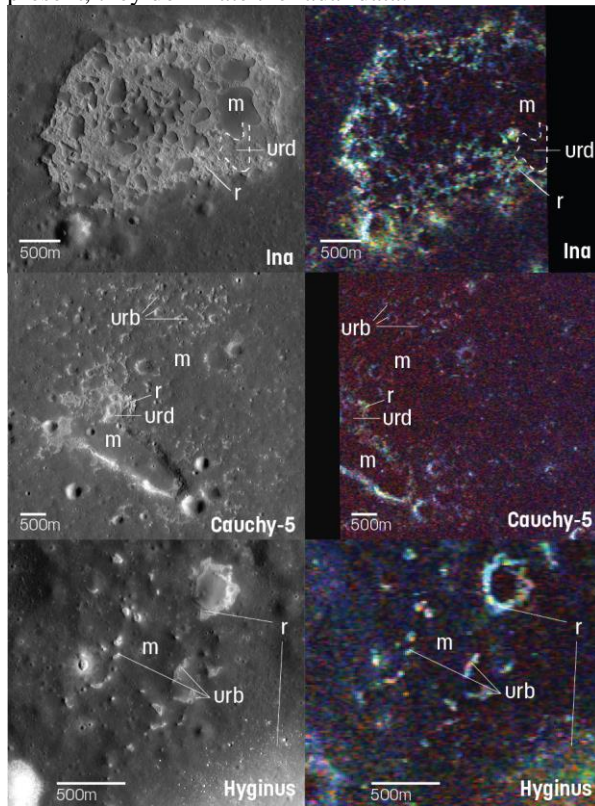


Figure 3: Close-up views of IMPs. Examples of units are marked: mounds (m), radar-dark uneven units (urd), radar-bright uneven units (urb), and rocky units (r).

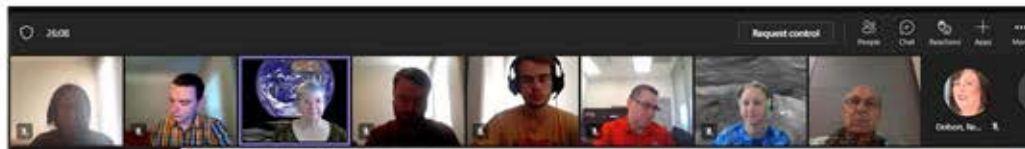
100-m scale lava-like textures, several small IMPs at the bases of steep slopes, and preservation of steep margins of fine-grained deposits are most consistent with a relatively young age. Further, the stratigraphy of mounds and uneven units is most simply explained by concurrent formation. Future exploration (e.g., returned samples, landings, field assays) of these landforms will likely be required to conclusively solve the enigma of when and how they formed [19, 20].

Acknowledgments: Dr. Lauren Jozwiak, MRF Team for assistance with locating and processing MRF products.

References: [1] Strain and El-Baz (1980) *Proc. Lunar Planet. Sci. Conf. 11th*, p. 2437-2446. [2] Schultz et al (2006) *Nature*, 444(7116), 184–186. [3] Stooke (2012) *JGR*, 125, 10.1029/2019JE006362. [4] Braden et al. (2014) *Nature Geoscience* 10.1038/NGEO2252. [5] Qiao et al (2019) *JGR124* 1100-1140. [6] Byron, B. D. et al (2022) *JGR* 127. [7] Raney et al. (2012) *JGR* 117, 10.1029/2011JE003986. [8] Carter et al (2013) *LPSC* 2146. [9] Weitz, C. M. et

al (2021) *LPSC* 7011. [10] Vannier et al. (2021) *LPSC* 1727. [11] Elder et al. (2017) *Icarus*, 290, 224-237. [12] Virrki and Bhiravarasu (2019) *JGR*, 124, 10.1029/2019JE006006. [13] Fa et al. (2011) *JGR*, 116, 10.1029/2010JE003649. [14] Carrier et al (1991) *Cambridge Univ. Press, New York*, 475-594. [15] Henderson et al (2020) *ESS*, 8, 10.1029/2019EA001013. [16] Mangan et al (1996) *JVGR*, 73, 1-18. [17] Giguere et al (2020) *JGR*, 125, 10.1029/2019JE006034. [18] Garry et al (2012) *JGR*, 117, 10.1029/2011JE003981. [19] Stopar et al (2019) *PSS*, 171, 1-16. [20] Qiao et al (2021) *PSJ*, 2:66, 10.3847/PSJ/abaaa0.

LPI Summer Intern Program in Planetary Science Orientation - June 7, 2022



Lunar and Planetary Institute

- The Lunar and Planetary Institute (LPI) is an integral part of the NASA Planetary Science Division's (PSD's) plan for the study of the Solar System
- **Purpose:** The LPI team provides a research and exploration leadership capability in planetary science and fosters communication and a greater involvement of the science community in the accomplishment of NASA's Planetary Science goals



A Tours

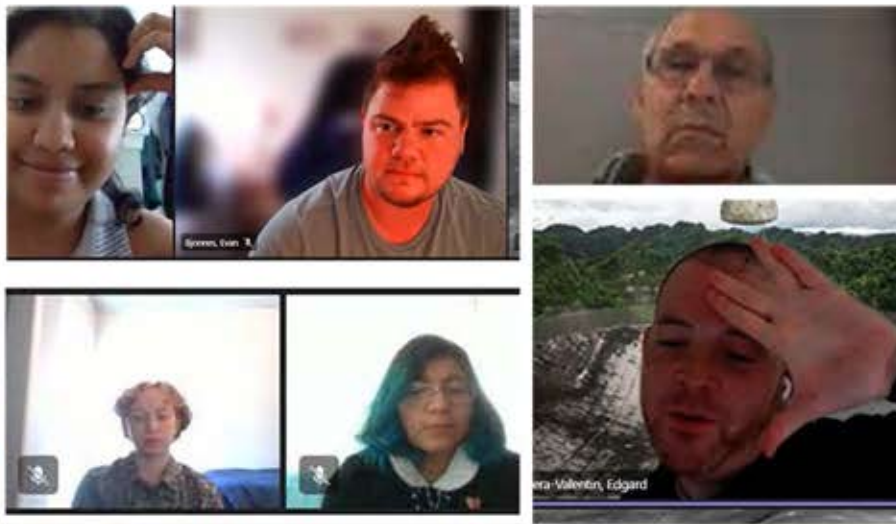
Person Tour
 7th. Due to time, another group of interns will
 rge with this tour.
 Please wears closed shoes. No flip flops or sandals are
 allowed during the tour.
 More information to come as we get closer to the visit.



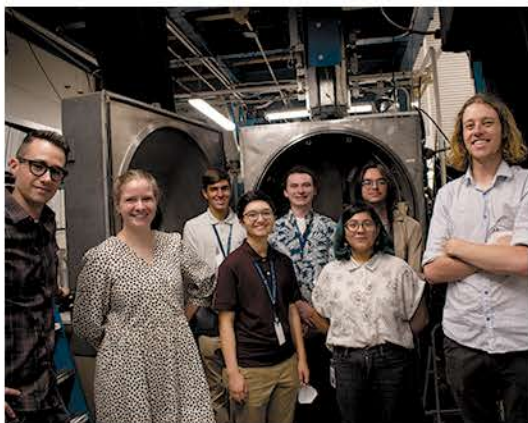
	Group 1	Group 2
:00 AM	VVA	EIL
:30 AM	EIL	VVA

VVA - Lunar Lab viewing area
 EIL - Experimental Impact Lab

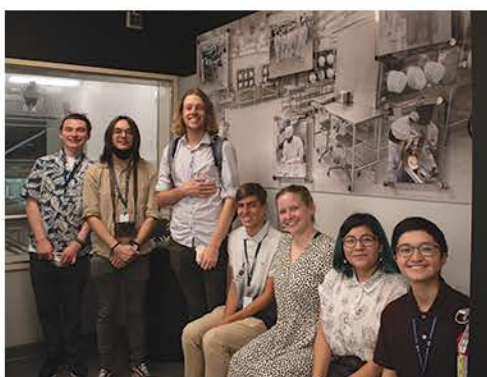
al Tour
 romaterials tour, July 8 at 11:00-12:00 pm (CDT)



July 7, 2022. The Experimental Impact Laboratory (EIL). The EIL has three different accelerators, each of which is used in its own way to simulate the effects of impact and shock on planetary surfaces and materials. Impacts in the EIL typically occur under near-vacuum conditions (pressures well below 1 torr).

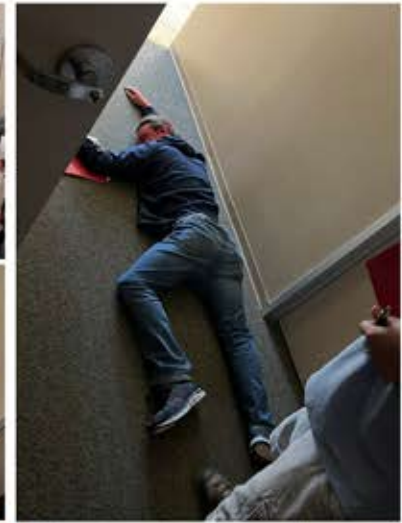


July 7, 2022. The Lunar Sample Laboratory Facility is a repository and laboratory facility at NASA's Lyndon B. Johnson Space Center in Houston, Texas, opened in 1979 to house geologic samples returned from the Moon by the Apollo program missions to the lunar surface between 1969 and 1972.



July 18, 2022. The Meteorite Laboratory. The curation and collection of Antarctic meteorites is a U.S. funded, cooperative effort among NASA, the National Science Foundation, and the Smithsonian Institution. Meteorites of greater interest and undergoing detailed study are kept at JSC for distribution to the scientific community, but irons are sent directly to the Smithsonian Institution.






Throughout the summer, the interns attended Brown Bag Seminars, where they were introduced to various fields in Planetary Science, and Professional Development Seminars, they were provided with career growth opportunities. The interns also assisted with Public Outreach, where they engaged the public in lunar and planetary science. National Intern Day was celebrated on July 28th.



LPI Intern Directory


Summer 2022



Alexander Nguyen

● INTERN TYPE
LPI Intern

● ADVISOR
Pat McGovern



Chansey Champagne

● INTERN TYPE
LPI Intern


● ADVISOR
Edgard Rivera-Valentin



Daniel Burgin

● INTERN TYPE
LPI Intern

● ADVISOR
Sam Crossley



David Bickham

● INTERN TYPE
LPI Intern


● ADVISOR
Paul Schenk



Emily Etheridge

● INTERN TYPE
LPI Intern


● ADVISOR
Brendan Anzures



Frida Garcia Ledezma

● INTERN TYPE
LPI Intern


● ADVISOR
Candice Bedford



Garrett Wolff

● INTERN TYPE
LPI Intern


● ADVISOR
Julie Stopar



Jacob Gambrell

● INTERN TYPE
LPI Intern


● ADVISOR
German Martinez



Maddie Westenberg
(They/Them)

● INTERN TYPE
LPI Intern


● ADVISOR
David Kring



Sedi Bogart

● INTERN TYPE
LPI Intern

● ADVISOR
Allan Treiman



Thea McKenna

● INTERN TYPE
LPI Intern


● ADVISOR
Matt Weller



William Wallentine

● INTERN TYPE
LPI Intern


● ADVISOR
Kennda Lynch



Xeynab Mouti

● INTERN TYPE
LPI Intern

● ADVISOR
Prajita Mane



Emily Roberts

● INTERN TYPE
LPI Summer Intern

● ADVISOR
Allan Treiman